Transport of Dirac Fermions on the Surface of Strong Topological Insulator and Graphene

Inaugural-Dissertation

zur

Erlangung des Doktorgrades der
Mathematisch-Naturwissenschaftlichen Fakultät
der Heinrich-Heine-Universität Düsseldorf

vorgelegt von

Arijit Kundu
aus Kolkata

June, 2012

Aus dem Institut für Theoretische Physik IV
der Heinrich-Heine Universität Düsseldorf

Gedruckt mit der Genehmigung der
Mathematisch-Naturwissenschaftlichen Fakultät der
Heinrich-Heine-Universität Düsseldorf

Referent: Prof. Dr. Reinhold Egger

Koreferent: Prof. Dr. Dagmar Bruß

Tag der mündlichen Prüfung: 14.06.2012

Zusammenfassung

In dieser Dissertation untersuche ich den elektronischen Transport mittels Dirac-Fermionen an der Oberfläche von starken topologischen Isolatoren und in Graphen.

Zu Beginn gebe ich eine Übersicht über topologische Isolatoren und Graphen, gefolgt von einer Einführung in die bei niedrigen Energien gültige effektive Theorie. Sie dient der Beschreibung elektronischer Zustände an der Oberfläche von starken dreidimensionalen topologischen Isolatoren und derer in Graphen. Unter Anwendung dieser Theorie gelange ich dann im Speziellen zur Struktur der Oberflächenzustände topologischer Isolatoren mit einem großen Oberflächen zu Volumen Verhältnis, wie es z.B. Nanodrähte oder Dünnschichtsysteme aufweisen.

Anschließend wird das Energiespektrum und die Spinparität der Eigenzustände eines aus einem topologischen Isolator konstruierten Quantenpunktes mit der Form einer Nanoröhre betrachtet. Numerische Berechnungen zeigen nun, dass sogar bei niedrigsten Energien eine Spin-Oberflächen-Fixierung aufgebrochen wird. Dies bedeutet, dass die Spinausrichtung in einem topologisch geschützten Zustand nicht relativ zur Oberfläche fixiert ist. Des Weiteren zeigt die Numerik die Existenz von impulslosen Moden und inter-Bandlücken Zuständen, die nahe der Grundflächen des zylindrischen Quantenpunktes lokalisiert sind. Die meisten Eigenschaften des Energiespektrums und die Spinstruktur der Eigenzustände wurden außerdem analytisch aus der Beschreibung durch Oberflächen Dirac-Fermionen reproduziert. Die Resultate wurden mit mikroskopischen Ansätzen, die auf einer Tight-Binding-Rechnung für einen topologischen Isolator in Nanoröhren Geometrie beruhen, verglichen und zeigen qualitative Ähnlichkeit.

Hierauf folgend werden durch Elektron-Phonon-Streuung hervorgerufene Effekte in dünnschichtigen Systemen aus topologischen Isolatoren theoretisch untersucht. Die Phononen werden hierbei durch eine isotropische elastische Kontinuumstheorie mit spannungsfreien Randbedingungen modelliert. Die Wechselwirkung mit den helikalen Oberflächen-Dirac-Fermionen wird hierbei durch ein Verformungspotenzial beschrieben. Der temperaturabhängige spezifische Widerstand $\rho(T)$ und die Quasipartikel-Zerfallsrate $\Gamma(T)$, beobachtbar durch Photoemission, werden numerisch berechnet. Für den Hoch- und Tieftemperaturgrenzfall werden analytische Ausdrücke in Form von Potenzgesetzen für diese beiden Größen berechnet. Detaillierte Vorhersagen über den gesamten Temperaturbereich für die Materialparameter von Bi_2Se_3 sind angegeben und ermöglichen eine experimentelle Bestätigung.

Anschließend wird eine für Dirac-Fermionen in topologischen Isolatoren und Graphen einheitliche Theorie zur Beschreibung von Quantentransport und der Streuung an räumlich lokalisierten statischen Magnetfeldern entwickelt. Das verwendete Modell beschreibt vereinheitlichend die Effekte von orbitalen magnetischen Feldern, Zeemann- und Austauschfeldern in topologischen Isolatoren und von durch Zug oder Defekten in einlagigem Graphen verursachten pseudomagnetischen Feldern. Die generelle Streutheorie hierzu wird formuliert, und für radial symmetrische Felder werden die Streuamplitude, der totale und der Transport-Streuquerschnitt in Abhängigkeit von Phasenverschiebungen ausgedrückt. Als Anwendung hierzu untersuche ich ringförmige magnetische Felder. Die Aharonov-Bohm Geometrie wird ebenfalls als Grenzfall der Ring-Geometrie untersucht.

Außerdem erörtere ich den supraleitenden Nahwirkungseffekt auf Graphen und untersuche resonantes Tunneln durch eine supraleitende Doppelbarrierenstruktur in Graphen als Funktion der Systemparameter. In diesem System entstehen Transmissionsresonanzen auf Grund von gebundenen Andreev Zuständen. Der Transport durch diese Geometrie, als Funktion der Einfallsenergie für verschiedene Einfallswinkel, zeigt eine Dämpfung der Resonanz, wenn die normale Reflektion zwischen den Barrieren sich erhöht. Des Weiteren betrachte ich noch das Phänomen des Quanten-Ladungs-Pumpens. Dieses wird erreicht durch eine periodische Modulation der Amplituden (Δ_1 und Δ_2) der Bandlücken der beiden zugehörigen supraleitenden Barrieren. Diese Modulation entspricht einer Pump-Kontur in der $\Delta_1 - \Delta_2$-Ebene des Parameterraums. Auf Grund von Resonanzen in dieser Ebene, erhält man eine große Menge gepumpter Ladung, wenn diese Kontur die Resonanzen umschließt. Dies steht in direktem Gegensatz zum Ladungspumpen in einer normalen Doppelbarrierenstruktur in Graphen, wo die gepumpte Ladung sehr klein ist auf Grund des Phänomens des Klein-Tunnelns. Das Verhalten der gepumpten Ladung als Funktion der Pumpstärke und der Phasendifferenz der Pumpparameter für verschiedene Einfallswinkel der Elektronen wird ebenfalls analysiert. Das Resonanzverhalten kann eventuell experimentell beobachtet werden.

Abstract

In this dissertation I study electronic transport through Dirac Fermions on the surface of strong topological insulator and graphene.

I start by reviewing the physics of topological insulator and graphene and the low energy effective theory for the electronic states of the surface of a 3D strong topological insulator and graphene. Using this theory the electronic structure of the surface states of strong topological insulators of geometries with large surface to bulk ratio like nanowire and thin film are obtained.

Then the energy spectrum and the spin-parity structure of the eigenstates for a finite size topological insulator quantum dot of the shape of a nanotube are considered. Numerical calculations show that even at the lowest energy scales, the "spin-surface locking" is broken, that is, the spin direction in a topologically protected surface mode is not locked to the surface. The calculations also show the existence of "zero-momentum" modes, and sub-gap states localized near the "caps" of the dot. Both the energy spectrum and the spin texture of the eigenstates are basically reproduced from an analytical surface Dirac fermion description. The results are compared to microscopic calculations using a tight-binding model for a strong topological insulator in a finite-length nanowire geometry, which shows qualitative similarity.

Then, a theoretical study of electron-phonon scattering effects in thin films made of a strong topological insulator is presented. Phonons are modeled by isotropic elastic continuum theory with stress-free boundary conditions, and the interaction with the helical surface Dirac fermions is mediated by the deformation potential. The temperature-dependent electrical resistivity $\rho(T)$ and the quasi-particle decay rate $\Gamma(T)$ observable in photo-emission are computed numerically. The low and high-temperature power laws for both quantities are obtained analytically. Detailed estimates covering the full temperature range are provided for the parameters of Bi_2Se_3 which possibly can be verified by experiment.

Afterwards, a theory of quantum transport and scattering by spatially localized static magnetic fields is developed in a unified way for the low energy Dirac Fermions on topological insulator and graphene. The employed model describes in a unified manner the effects of orbital magnetic fields, Zeeman and exchange fields in topological insulators, and the pseudo-magnetic fields caused by strain or defects in monolayer graphene. The general scattering theory is formulated, and for radially symmetric fields, the scattering

amplitude and the total and transport cross sections are expressed in terms of phase shifts. As applications, I study ring-shaped magnetic fields. The Aharonov-Bohm geometry is also studied as a limit to the ring geometry.

I also review the superconducting proximity effect on graphene and study resonant tunneling through a superconducting double barrier structure in graphene as a function of the system parameters. In this geometry, transmission resonances occur because of the formation of Andreev bound states. The evolution of the transport through this geometry as a function of the incident energy for various angles of incidence shows the damping of the resonance as normal reflection between the barriers increases. I also consider the phenomenon of quantum charge pumping of electrons in this geometry in the adiabatic limit. Quantum charge pumping can be achieved by modulating the amplitudes (Δ_1 and Δ_2) of the gaps associated with the two superconducting strips. Because of transmission resonances in the $\Delta_1 - \Delta_2$ plane of parameter space, a large value of pumped charge is obtained when the pumping contour encloses the resonances. This is in sharp contrast to the case of charge pumping in a normal double barrier structure in graphene, where the pumped charge is very small, due to the phenomenon of Klein tunneling. The behavior of the pumped charge as a function of the pumping strength and the phase difference between the two pumping parameters, for various angles of the incident electron is also analyzed. The resonance behavior can possibly be observed by experiment.

Contents

Acknowledgement

First of all, I would like to express my gratitude to my supervisor Prof. Dr. Reinhold Egger for giving me the opportunity for doing the doctoral study with him in this beautiful country and for constantly guiding me throughout my doctoral study. His efficiency and determination will always be an example to me. I am also grateful to Prof. Dr. Sumathi Rao for being a source of constant friendly guidance.

I like to thank Dr. Alex Zazunov, who is not only my teacher and colleague, he is also a great friend and source of inspiration to me. I like to thank Dr. Sébastien Giraud, Prof. Dr. Alfredo Levy Yeyati, Prof. Dr. Thierry Martin, Dr. Arijit Saha and Artur Hütten for working with me and guiding me. I am also thankful to Priv.-Doz. Dr. Alessandro De Martino, Dr. Stephan Weiß and Dr. Tomi Paananen for useful discussions. I also like to thank Prof. Dr. Dagmar Bruß for being my referee for the dissertation.

A very special thanks go to my girl-friend Rajeswari, for being with me in good as well as in difficult times. I am extremely lucky to have friends like Aldo and Roland, who were always helping me in any problem. I also thank my 'long-distant' friend Debasish for many discussions.

And finally, I can not finish my acknowledgement page without mentioning my parents, without their constant support it could be difficult for me to continue the journey for being a researcher.

Introduction

Graphene was studied theoretically over few decades. But is was generally believed that a monolayer graphene will be almost impossible to separate out for studying their properties, and even if they could be separated, they will not be stable against thermal fluctuation. In 2004, an experimental discovery by André Geim *et al.* proved both of the believes to be not true. As a result of this discovery, the decade old system has become an extremely rapidly growing field of research. Topological Insulator is rather a new field of research, which is the generalization of the celebrated quantum-Hall systems (described by Klitzing in 1980). Historically predicted topologically protected states in a quantum well were first experimentally observed by Konig *et al.* only in 2007. The first 3D topological insulator was predicted to be bismuth antimony by Hsieh *et al.* in 2008. Since then, exciting physics like the non-trivial surface state of a topological insulator, the possibility of appearance of Majorana Fermions at the interface with superconductor have made it one of the most active field of research in theoretical as well as in experimental condensed matter physics.

Although physically different, the electronic transport by the surface state of a "Topological Insulator" and in "graphene" are both remarkably described by relativistic Dirac Fermions, with light velocity replaced by the Fermi velocity. This opens up an opportunity to study then simultaneously, often in an unified way. In experiments with this systems, the usual length scale are in the order of nano-meters. That lies in the regime of *mesoscopic physics*. In this thesis, I will describe the theoretical studies and research I performed in my doctoral program concerning many phenomena associated with mesoscopic electronic transport in topological insulator and in graphene.

Organisation:

In the first chapter I shortly review the physics of topological insulator and graphene. I describe the topological insulating phase as a topologically nontrivial phase generalizing from quantum Hall phase. In a 3D *strong* topological insulator, the surface state is best described by massless Dirac Fermions system. This "massless-ness" is protected by the topology of the bulk system. In the Sec. 3 of the chapter I review the band structure of a monolayer graphene along with its symmetries and the emergence of Dirac Fermions as low energy excitations around certain points in the Brillouin zone.

In the next two chapters (2nd and 3rd) I discuss the effective Hamiltonian, energy

spectrum and important spin texture for different 3D topological insulator geometries starting from a low energy Hamiltonian introduced by Zhang *et al* in 2009. We specially focus on the case of a nanotube geometry. I also introduce a Dirac surface Fermion theory for describing the system.

In the next two chapters (4th and 5th) I discuss interaction effect on topological insulator surface state and graphene. Thin film geometry is one of the most favorable geometry for transport measurement experiments because of its better surface to bulk ratio. The temperature dependent resistivity and lifetime broadening of a topological insulator is discussed in Chapter 4. In Chapter 5, I describe the magnetic scattering of the Dirac Fermions on the topological insulator surface and graphene in a unified manner.

Chapter 6 is dedicated to study an interesting mesoscopic geometry with graphene and proximity induced superconductivity. An incident electron from graphene on such an interface can reflect back as hole, which is called the Andreve refletion. Due to this process, one expects boundstates within the quantum well formed by a double superconductor barrier structure in graphene, which gives rise to tunneling resonances. I discuss such resonating transport along with the large pumped charge in this system.

Most of the results of Chapter 2-6 are obtained while working with Prof. Dr. Reinhold Egger, Dr. Alex Zazunov, Prof. Dr. Sumathi Rao, Dr. Arijit Saha, Prof. Dr. Alfredo Levy Yeyati, Prof. Dr. Thierry Martin, Dr. Sébastien Giraud and are published in scientific journals, which I list in the chapter 'List of Publications'.

Finally, I discuss the conclusions of my study and research described in the thesis.

List of abbreviations

Following is the list of abbreviations I used througout the text of the thesis:

ARPES	Angle-resolved photo-emission spectroscopy
BZ and FBZ	both denotes the first Brilloiun zone
QHE	Quantum Hall effect
QSHE	Quantum spin-Hall effect
TR	Time-reversal
TI	Topological insulator
AR	Andreev reflection
SAR	Specular Andreev reflection
CAR	Crossed Andreev reflection
SCAR	Crossed specular Andreev reflection
CT	Co-tunneling
SDB	Superconducting double barrier
SB	Superconducting barrier
NS	Metal - superconductor junction
NSN	Metal - superconductor - metal junction

Chapter 1

Dirac Fermions in Topological Insulator and Graphene

1.1 Introduction

In this chapter we review the electronic structure and the emergence of Dirac Fermions on topological insulator surface and in grapehene. We start with distinguishing a trivial insulator with a nontrivial insulator through the topological aspect of band theory. We then follow the advancement from quantum Hall state to quantum spin-Hall state to 3D topological insulating state. This review is followed from several other reviews noted in Ref. 1–3. Then in Sec. 1.3 we discuss the band structure and emergence of Dirac Fermions as low energy excitations in graphene close to the special Dirac points $\boldsymbol{K}, \boldsymbol{K}'$. Although the low-energy excitations in a strong topological insulator and graphene are Dirac Fermions, there are several fundamental differences between these two systems, which we discuss at the end of the chapter Sec. 1.4.

1.2 Topological Insulators

1.2.1 Band theory of solids

One of the most celebrated theoretical discovery in condensed matter physics in the last century was the development of band theory of solids and to explain insulating and metallic states of matter. Electrons carry the charge in a metal, and if in a material it becomes energetically costly to excite a bound electron to become a conducting electron, the material becomes an insulator. The simplest example is a atom, where the electron is bound to the nuclei in closed shell.

In a crystal, band theory exploits the the symmetries because of the periodicity of the structure to classify the electronic states in terms of their *crystal momenta* $\mathbf{k}$, which we explain below:

Bloch Hamiltonian

In a crystal, the electrons are subjected to periodic potential $V(\boldsymbol{r})$, and the simplest single electron Hamiltonian has the form:

$$H = \frac{\hat{\boldsymbol{p}}^2}{2m} + V(\boldsymbol{r}), \tag{1.1}$$

where $V(\boldsymbol{r}+\boldsymbol{a}) = V(\boldsymbol{r})$ is periodic with the Bravias lattice vector $\boldsymbol{a}$ and the Hamiltonian commutes with the discrete translation operator $[H, \hat{T}_{\boldsymbol{a}}] = 0$ where

$$\hat{T}_{\boldsymbol{a}}\psi(\boldsymbol{r}) = \psi(\boldsymbol{r}+\boldsymbol{a}) \ , \tag{1.2}$$

and it can be described by the operator $\hat{T}_{\boldsymbol{a}} = \exp(i\boldsymbol{q}\cdot\boldsymbol{a})$. Here $\hbar\boldsymbol{q}$ is called the crystal momenta (or Bloch momenta[4]) and is defined based on the lattice symmetry. For a Bravias lattice, the primitive cell in the momentum space is called the first Brillouin zone (FBZ or BZ), and $\boldsymbol{q}$ is single valued only in the FBZ.

Now, as $\hat{T}_{\boldsymbol{a}}$ commutes with the Hamiltonian, the eigenstates of the Hamiltonian can be expressed as eigenstate of the translation operator, and it satisfies the following boundary condition:

$$\psi_{n\boldsymbol{q}}(\boldsymbol{r}+\boldsymbol{a}) = e^{i\boldsymbol{q}\cdot\boldsymbol{a}}\psi_{n\boldsymbol{q}}(\boldsymbol{r}) \ , \tag{1.3}$$

where n is called the band index. $\boldsymbol{q}$ is a good quantum number, and so, we can go to a shorter Hilbert space, which is characterized by parameter $\boldsymbol{q}$, by the unitary transformation:

$$H(\boldsymbol{q}) = e^{-i\boldsymbol{q}\cdot\boldsymbol{r}}He^{i\boldsymbol{q}\cdot\boldsymbol{r}} = \frac{(\hat{\boldsymbol{p}}+\hbar\boldsymbol{q})^2}{2m} + V(\boldsymbol{r}) \ . \tag{1.4}$$

The transformed eigenfunctions $u_{n\boldsymbol{q}}(\boldsymbol{r}) = e^{-i\boldsymbol{q}\cdot\boldsymbol{r}}\psi_{n\boldsymbol{q}}(\boldsymbol{r})$ is periodic with the lattice vector:

$$u_{n\boldsymbol{q}}(\boldsymbol{r}+\boldsymbol{a}) = u_{n\boldsymbol{q}}(\boldsymbol{r}) \ . \tag{1.5}$$

The mapping from a Bloch momenta $\boldsymbol{q}$ to the eigenvalues $E_m(\boldsymbol{q})$ is called the dispersion relation, and $E_m(\boldsymbol{k})$ defines the energy bands of the material. Energy of the last occupied band is called the Fermi energy.

In an insulator there is a gap between the Fermi energy and the next energy band (conduction band). For the insulating phase of a matter, the most important bands are just above and below the Fermi energy. Although different insulators have different band structure, but one can interpolate between them adiabatically without closing the energy gap. In that sense all conventional insulators are equivalent, and which is also equivalent to the vacuum. Because, according to Dirac's theory in vacuum, all positron levels are filled and it also has a energy gap, called the pair production energy.

1.2.2 Quantum Hall effect (QHE)

The integer quantum Hall state[5,6] is a situation where a insulator state becomes not-equivalent to vacuum. In a strong magnetic field the electrons in a 2D electron gas moves in cyclotron motion with frequency ω_c and forms landau levels with energy $\epsilon_m = \hbar\omega_c(m+1/2)$. If N Landau levels are filled and the rest are empty, then there is an

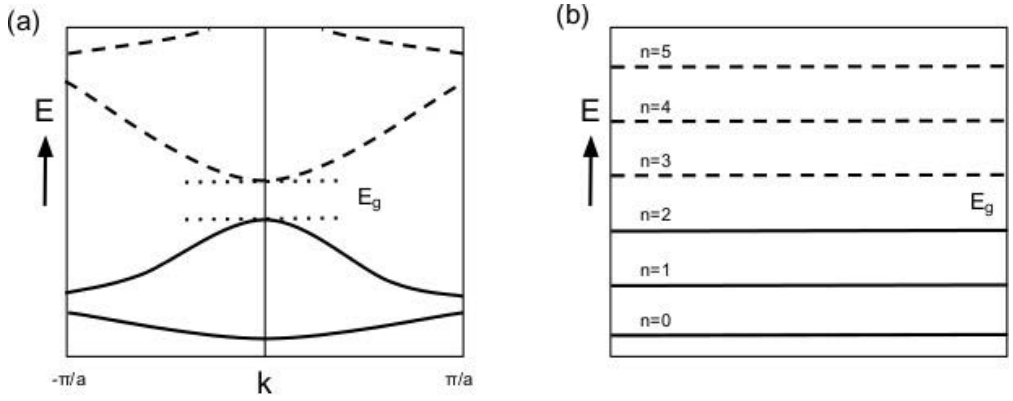

Figure 1.1: The energy bands in (a) a trivial insulator inside the BZ, (b) quantum Hall state (the Landau levels). The dotted lines denote the empty bands and the solid lines denote the filled band. The energy difference between the highest filled band (valence band) and the first empty band is the energy gap E_g.

energy gap separates the occupied and empty states just as in an insulator (see Fig. 1.1). And one can recognise the system as like a lattice with unit cell area enclosing a unit flux quantum.[3,7]

But, unlike an insulator, in this case an electric field causes the cyclotron orbits to drift, leading to a Hall current characterized by the quantized Hall conductivity.[i] The quantisation of Hall conductivity is a topological property and can be seen from the formulation of Berry phase. We have discussed the Berry phase and quantum Hall effect in Appendix A.

The quantum Hall conductivity of a system is determined by the TKNN invariant[8] (or the first Chern number[9]) of a system (which is either zero or an integer)

$$n_C = \frac{1}{2\pi}\int_{\mathsf{BZ}} \frac{d^2k}{(2\pi)^2} \sum_{\text{Filled band } n} \Omega^n_{k_x k_y} \ , \tag{1.6}$$

where $\Omega^n_{k_x k_y}$ is the Berry curvature[10] of nth band defined in Appendix A. The Hall conductivity is quantised in the unit of (e^2/h) as

$$\sigma_{xy} = n_C \frac{e^2}{h} \ . \tag{1.7}$$

The TKNN invariance is a topological property of the ground state. Two ground states of two Hamiltonians cannot be continuously deformed into one another if they carry different Chern numbers. In this case, the two insulators are topologically distinct.[9] The only way to deform two systems of different topological signature into one another is by closing the band gap, i.e. via an intermediate metallic configuration. For a conventional

[i] Hall conductivity is defined as the electrical conductivity in a perpendicular direction to the applied electric field.

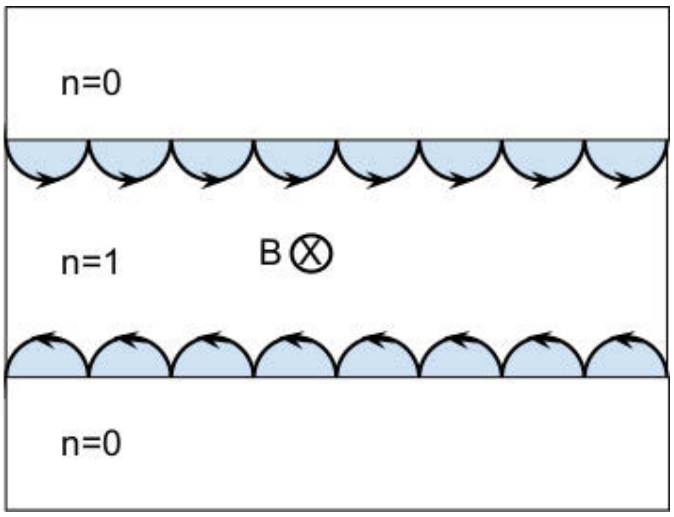

Figure 1.2: Explanation of quantum Hall effect because of the conduction by the edge.

insulator the Chern number is zero. Insulators of non-vanishing Chern numbers are called topological insulators or Chern insulators.

1.2.3 Edge state and bulk-boundary correspondence

Propagation by edge state

The integer quantum Hall effect can also be visualised from an intuitive physical picture.[11] In presence of a magnetic field, the electrons move in circular orbit with energy equal to the cyclotron frequency. Now, if we have a 2D surface with finite width, the electrons at the boundaries can not complete their orbits. They perform a skipping motion as shown in Fig. 1.2, and that is the reason for conductivity by the edge. This picture shows that, although in the bulk the quantum Hall system is an insulator, it can be metallic at the interface with a trivial insulator (here vacuum). Also, as the conduction in *chiral*, as there is no way to rotate oppositely, hence no possibility for back scattering. This can not be modified by small perturbation, like disorders. And hence, the quantisation of Hall conductivity is robust (topologically protected).

This above picture gives a hint to the non-trivial nature of the edge states at the boundary of a trivial and a topological insulator. As we discussed in the previous section that, one can not smoothly deformed (i.e. without closing any gap) into one another between two topologically non-equivalent band structure. The only way to do this is to close the gap. So, we expect at the boundary of two such materials some gap-less edge state. We will explain it below by an example.

Hall conductivity of Dirac Fermions in continuum

The 2D Dirac equation has the following form

$$H_D = k_x\sigma_x + k_y\sigma_y + m\sigma_z \ , \tag{1.8}$$

where $m\sigma_z$ is the mass term which opens up a gap in the spectrum. This has two bands, and the lower band is occupied in the case of vacuum. The Hall conductivity can be computed by calculating the Berry curvature over the occupied state (with $e^2/h = 1$)

$$\sigma_{xy} = \frac{\text{sgn}(m)}{2} \ . \tag{1.9}$$

This half integer Hall conductivity is puzzling, but it appears because as it is not in a lattice, the Dirac fermions are not regularised properly. But, if the sign of m changes, the total change of Hall conductivity is 1.

Edge mode

Let us choose a boundary between a Dirac Hamiltonian (Eq (1.8)) with positive mass and one with negative mass:

$$H_D(y) = -i\partial_x\sigma_x - i\partial_y\sigma_y + m(y)\sigma_z \ , \tag{1.10}$$

where $m(y) > 0$ for $y > 0$ and $m(y) < 0$ for $y < 0$. Remarkable, one can verify that this system has a solution

$$\psi(x, y) = e^{ik_x x} \exp\left(-\int_0^y m(y')dy'\right) \begin{pmatrix} 1 \\ -1 \end{pmatrix} \ , \tag{1.11}$$

with energy $E = k_x$. This mode obviously is confined only close to the boundary $y = 0$ and decays exponentially on either side and is *chiral* because of a positive group velocity $dE/dk_x = 1$. This model was studied first by Jackiw and Rebbi.[12]

Bulk-boundary correspondence

The above example shows that we have edge modes at the interface between two insulators (as they both have non zero mass on either side) with different Hall conductivity. One of them has 1/2 Hall conductance and the other has -1/2 Hall conductance. Once we properly regularise the system (by putting on a lattice), one of them will have Hall conductance 0 and other one will have Hall conductance 1. This edge mode argument can be generalised. Edge mode exists at the interface of two topologically non-equivalent system. This edge modes are not independent of the bulk, and a signature of the bulk-topology. This is called the bulk-boundary correspondence.

1.2.4 Time reversal symmetry and Hall conductivity

Non-zero Quantum Hall conductivity depends on time reversal (TR) symmetry breaking. Let us shortly review the properties of TR symmetry:

TR symmetry

TR transformation is defined as a mapping

$$T : t \to -t \ . \tag{1.12}$$

Under time reversal we have the follwoing properties:

$$T\hat{x}T^{-1} = \hat{x} \ , \quad T\hat{k}T^{-1} = -\hat{k} \ . \tag{1.13}$$

Using them, from $[\hat{x}, \hat{k}] = i$, we have $TiT^{-1} = -i$, and so, for a spinless particle, $T = K$, where K is the complex conjugation operator. In general $T = UK$ where U is an unitary matrix. For a spinfull particle TR flips the spin $TST^{-1} = -S$, which is equivalent to rotate the spin (in spin space) and a representation for TR operator is $T = -e^{-i\pi S_y}K$, where the (-1) sign is for convenience. For a spin 1/2 particle, $\boldsymbol{\sigma}/2$ denote the spin, and we have

$$T = -e^{-i\pi\sigma_y/2}K = i\sigma_y K \ . \tag{1.14}$$

This also gives rise to the relation

$$T^2 = -1 \ . \tag{1.15}$$

The main consequence of this is called the *Kramer's theorem*, which states that for a single particle state $|\psi\rangle$ with energy E, if the system is TR symmetric (i.e. $[H, T] = 0$), then $T|\psi\rangle$ is also an eigenstate with the same energy and $|\psi\rangle$, $T|\psi\rangle$ are orthogonal. That is, every single particle energy states are at least doubly degenerate.

Now, for QHE, we so far formulated the system as with spinless particle and the magnetic field acts on the system by Lorentz force. For a spinless system, the above formulation of TR operator gives, for a time reversal symmetric band, the wave-function must follow:

$$Tu(\boldsymbol{k})T^{-1} = u(-\boldsymbol{k})^* = u(\boldsymbol{k}) \ . \tag{1.16}$$

Now, the Berry curvature is defined as (Eq. (A.11)), for a single band,

$$\begin{aligned}
\Omega_{ij}(\boldsymbol{k}) &= i\left[\left\langle \frac{\partial u(\boldsymbol{k})}{\partial k_i} \middle| \frac{\partial u(\boldsymbol{k})}{\partial k_j} \right\rangle - \langle i \leftrightarrow j \rangle\right] \\
&= i\left(\frac{\partial u(\boldsymbol{k})^*}{\partial k_i}\frac{\partial u(\boldsymbol{k})}{\partial k_j} - \langle i \leftrightarrow j \rangle\right) \\
&= i\left(\frac{\partial u(-\boldsymbol{k})}{\partial k_i}\frac{\partial u(-\boldsymbol{k})^*}{\partial k_j} - \langle i \leftrightarrow j \rangle\right) \\
&= i\left(\frac{\partial u(-\boldsymbol{k})}{\partial(-k_i)}\frac{\partial u(-\boldsymbol{k})^*}{\partial(-k_j)} - \langle i \leftrightarrow j \rangle\right) \\
&= -\Omega_{ij}(-\boldsymbol{k}) \ ,
\end{aligned} \tag{1.17}$$

which gives zero while integrating over the full BZ. This shows that the TKNN invariant is zero for a system with time reversal symmetry. So, a time reversal breaking term (like magnetic field) is necessary for having non-zero Hall current.

1.2.5 Quantum spin-Hall effect (QSHE)

The qualitative picture for quantum spin-Hall effect[13–15] (QSHE) is explained in Fig. 1.3. In a quantum Hall effect the 1D channel is broken in a fashion shown in Fig. 1.3(a), which of course breaks the TR symmetry. But the channel can also be broken in a TR symmetric fashion as shown in Fig. 1.3(b). This system has non-zero Hall conductivity separately for spin up and spin down electrons, but the total Hall conductivity zero. These systems are called quantum spin-Hall state, first proposed by Bernevig and Zhang.[15]

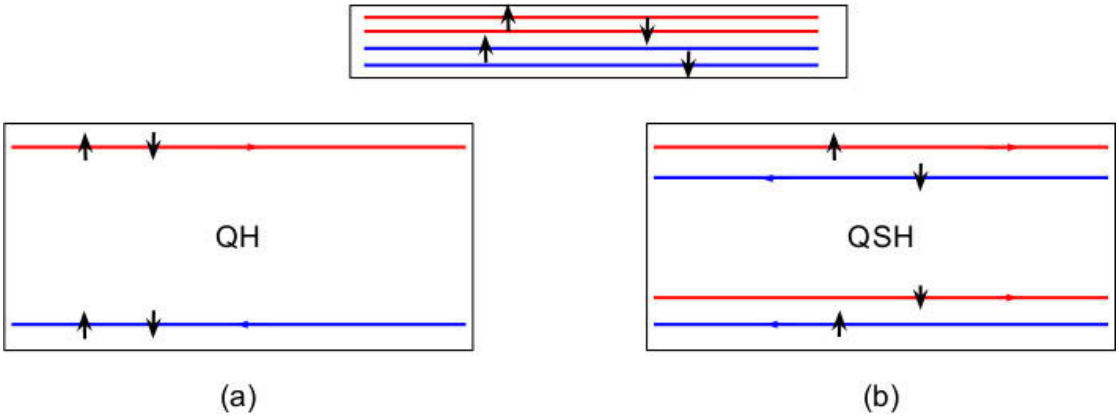

Figure 1.3: Breaking of 1D particle channel in quantum Hall effect (a) and TR symmetric quantum spin-Hall effect (b). The red line shows the right moving channel and the blue line shows left moving channel. Such breakup giving rise to chiralities are only possible if the bulk has non-trivial topology.

HgTe/CdTe quantum well

The theoretical prediaction of QSHE was followed by experimental observation first in HgCdTe quantum well.[16,17] In CdTe, the conduction band is formed by electrons in s orbitals and the valence band is formed by p orbitals. Whereas, in HgTe, because of strong spin-orbit coupling,[18] the p orbital-band is pushed above to become conduction band and the s-orbital band becomes the valence band. In the experiments, a system was formed by sandwiching HgTe inside two CdTe blocks (shown in Fig. 1.4). This gives a 2D quantum well potential. Now, if the width of the HgTe block is very small (< 6.3 nm), the electronic structure is dominated by the influence of CdTe inside HgTe, and the conduction and valence bands (E_1 and H_1 in the figure) remain the same as HgTe. But, if the width becomes > 6.3 nm, because of the strong spin-orbit coupling, the bands get inverted. In this situation, 1D edge states at the interface of HgTe and CdTe exist.

Now, as the system is time reversal symmetric (intrinsic spin-Hall effect does not break TR), the TKNN invariant vanishes. But there exist non-trivial edge states at the boundary. From the bulk-boundary correspondence, there must be some topological property of the bulk responsible this. This topological property is characterised by the Z_2 invariant, which we will describe shortly.

The appearance of QSHE can be explained in a similar manner as the integer QHE by a formulation of non-abelian Berry phase theory.[7,19–21] Where the Berry connection (for abelian case Eq. (A.8)) is replaced by a matrix because of the spin degree. The Berry curvature in many systems (for eg. in Dirac model) becomes proportional to spin $\boldsymbol{S}$.[19] A generalised version of the anomalous velocity Eq. (A.14) is obtained for non-abelian case, which becomes proportional to $\boldsymbol{E} \times \boldsymbol{S}$.[7] That is, the trajectories of spin up and spin down electrons are parted towards opposite direction perpendicular to the electric

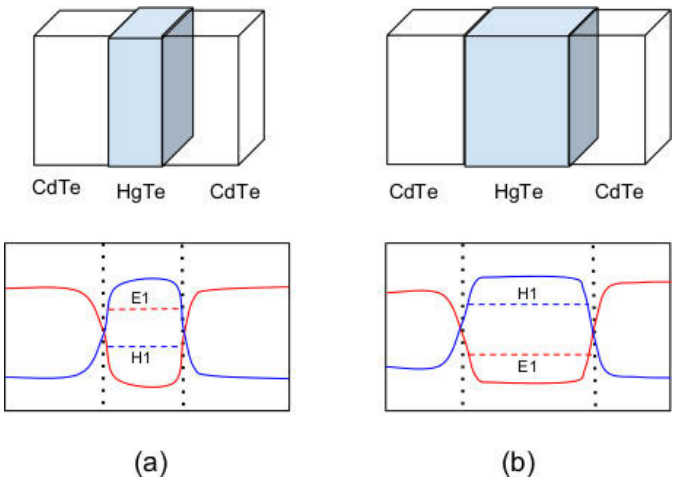

Figure 1.4: Quantum spin-Hall effect in CdHgTe quantum well. Because of strong spin-orbit coupling in HgTe, the conduction and valence band of them are opposite in HgTe and CdTe. (a) If HgTe is sandwiched between blocks of CdTe, up to a critical length the influence of CdTe dominates in the band structure of the HgTe. (b) After the critical width a band inversion occurs in HgTe and the system acquires a non-trivial topology giving rise to a spin-Hall state.

field. If population of different spins are equal, then this gives the spin-Hall effect.[ii]

1.2.6 Z_2 invariant

Most of the usual TR invariant insulators does not show non-trivial edge states at the boundary. The topological property of the bulk responsible for the QSHE edge states is the Z_2 invariant, which can have only two possible values (in 2D) $\nu = 0, 1$.[13,22] This can be understood from bulk boundary correspondence. In Fig. 1.5, we have plotted the band structure associated with the edge of two 2D TR invariant insulator with respect to the crystal momentum along the edge. Due to the TR symmetry, the band structure is symmetric around the mid of the Brillouin zone $k = \pi/a$. So, it is sufficient to show only one half of the Brillouin zone. The special points $k = 0$ and $k = \pi/a$ are (only) TR symmetric points in 2D. So, the bands must be degenerate at this points, because of the Kramer's theorem.

Depending on the bulk structure, there might be edge modes present. If they are present, they also must be degenerate at these two TR invariant points and away from these points the degeneracy can be lifted (by spin orbit coupling, for eg). But, there are only two ways the bands of surface states can connect between $k = 0$ and $k = \pi/a$. Either they can connect like in Fig. 1.5(a), where they intersect the Fermi energy at an odd number of points, or they can connect like in Fig. 1.5(b) intersecting the Fermi energy an even number of times. But for the second case , without closing any gap all

[ii] In case of ferromagnet, the population of spin up and spin down are different and the resulting state is called anomalous quantum-Hall state.

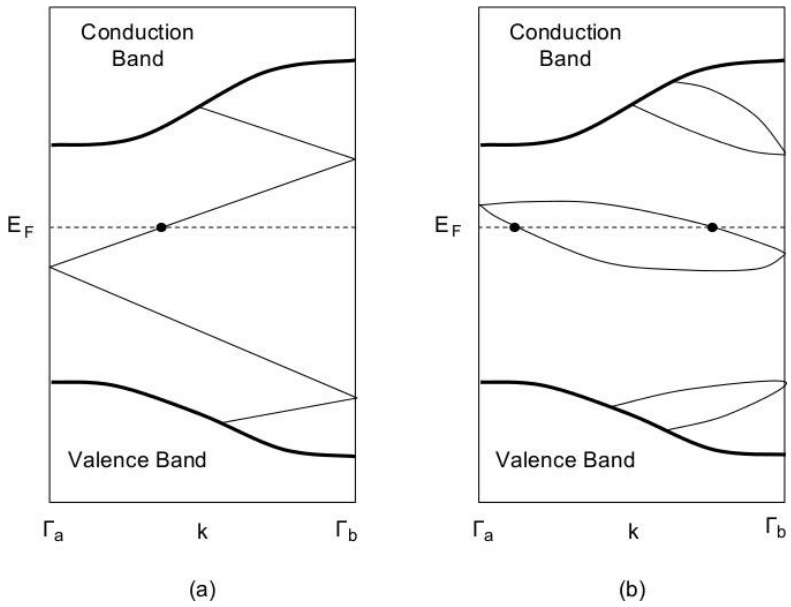

Figure 1.5: Band structure at the edge of TR invariant insulator between the two TR symmetric points $\Gamma_a = 0$ and $\Gamma_b = \pi/a$. In case of (a), the surface state crosses the Fermi energy odd number of times and in the case (b), it crosses an even number of time. Z_2 invariant $\nu = 1$ for the first case, whereas it is zero for the second case.

the edge states can be moved away from the gap (by *disorder*). But for the first case it is not possible. So, the two systems are topologically different. The invariant which determines the topological class in the Z_2 invariant. For the first case, its value is $\nu = 1$, whereas for the second case its value is $\nu = 0$.

In general, if the band of the edge modes of a TR invariant insulator and a trivial insulator intersect the Fermi energy N_f number of times, the Z_2 invariant is defined as $\nu = N_f \bmod 2$. There are several ways to calculate the invariant.[22–29] For system with extra symmetry it can be calculated exploiting the symmetries. We show the case of inversion symmetry for 3D TI Bi_2Se_3 in Sec. 2.2. If the system has conservation of spin (S_z), then the up and down spin has independent Chern number $n_\uparrow$, $n_\downarrow$. Because of TR symmetry, $n_\uparrow + n_\downarrow = 0$, but the difference $n_- = (n_\uparrow - n_\downarrow)/2$ defines the quantised spin Hall conductance, and the Z_2 invariance is then given by $\nu = n_- \bmod 2$.[30]

1.2.7 3D topological insulator

The 2D spin-Hall states can be generalised to 3D which are usually called 3D topological insulator (TI). It was predicted in many materials including 3D HgTe quantum well. But first good material (because of large bulk gap) for TI was predicted by Zhang et al in Bi_2Se_3 and Bi_2Te_3 like materials. There have been sucessfull experiments with Bi_2Se_3 confirming the predictions. We discuss the surface state of Bi_2Se_3 in the next chapter.

To specify a 3D TI one needs four Z_2 invariants $(\nu_0; \nu_1, \nu_2, \nu_3)$, which also can be

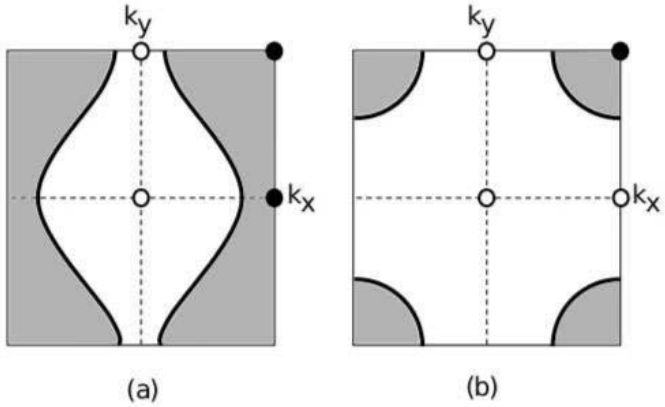

Figure 1.6: Band structure of the surface state of TR invariant topological insulator. The four TR invariant points are shown with circular dots. The Fermi arc (the boundary of the shaded area) can enclose an even number of TR invariant points in (a) or an odd number of TR invariant points in (b) depending on the bulk topology. The enclosed points are plotted with filled dots.

understood from the bulk-boundary correspondence.[7] The surface of a 3D TI can be labeled by 2D crystal momenta. In three dimensions there are 8 TR invariant points[iii] in the bulk which project into 4 TR invariant points on the surface. So, the surface bands, if they exit, must be degenerate at these points. Away from this TR points spin-orbit coupling lifts the degeneracy. Similar to the 2D case, there are different ways the bands may connect between the TR invariant points in two different ways, shown in Fig. 1.6. The ring bounding the surface band is the Fermi ring (a 1D surface for 2D band). The ring can surround an even number of TR points, or it can cover an odd number of TR points. Which of these two occurs is determined by the four Z_2 invariants of the bulk.

The simple generalisation from 2D to 3D spin-Hall state can be achieved by simply stacking layers of 2D spin-Hall surfaces.[31] Fig. 1.6(a) shows the Fermi surface of the surface of such a 3D spin-Hall system, where the layers are stacked on the y axis. But, in this case the Fermi arc of the surface state encloses an even number of TR invariant point, and unlike 2D case, surface states in this case are not protected from disorder. Such topological insulators are called weak topological insulators and they have the index $\nu_0 = 0$.

Z_2 invariant $\nu_0 = 1$ is a distinct phase, called *strong topological insulator*. This ensures that the Fermi arc of the surface state encloses an odd number of TR invariant point. These surface states are protected against disorder. This state is not a direct generalization of the 2D spin-Hall state. In the rest of the report, we will mean to strong topological insulator whenever we mention topological insulator (TI) in 3D.

[iii] We denote them as Γ_i, i=1,8 and Γ denotes the $\boldsymbol{k} = 0$ point in BZ .

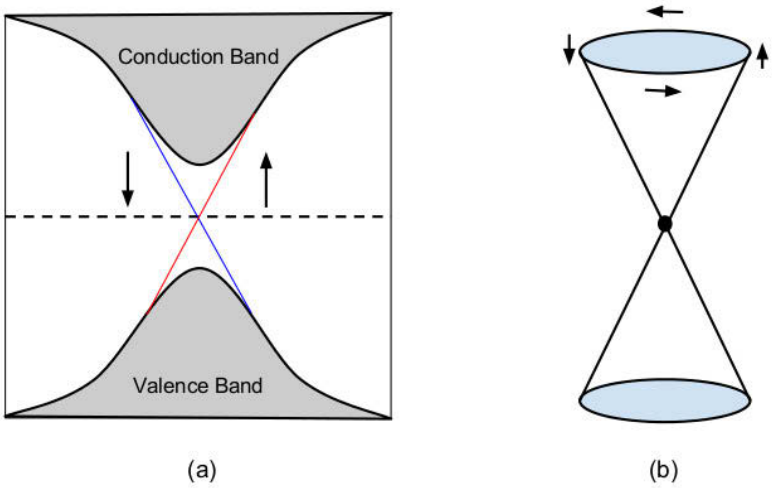

Figure 1.7: Helical Dirac Fermion in QSHE and on the surface of 3D TI . (a) Shows that the two opposite spin states have opposite velocity in a QSHE surface. (b) Shows in a 3D TI , the spin is always perpendicular to the momentum, but also lies on the surface.

1.2.8 Dirac Fermions

The Fermi arc of the surface of a strong topological insulator encloses an odd number of TR invariant points. This nature is protected by topology. For the simplest case, when it encloses one TR invariant point, the surface band can be described by the Dirac Hamiltonian[iv]

$$H_{\text{surface}} = -i\hbar v_F \boldsymbol{\sigma} \cdot \boldsymbol{\nabla} \ , \tag{1.18}$$

where $\boldsymbol{\sigma}$ is spin, and for a surface with a mirror plane (inversion symmetry), symmetry requires the spin density[3]

$$\boldsymbol{S} \propto \hat{e}_z \times \boldsymbol{\sigma} \ , \tag{1.19}$$

where $\hat{e}_z$ is the direction perpendicular to the surface. This property is called *spin-surface locking*. Here we wish to mention that, in a system there must be in total an even number of Dirac points on the surface, otherwise the Hall conductivity of the system will be an half integer. This is called the *Fermion doubling theorem*. For graphene, we see in the next section, that, existence of $\boldsymbol{K}, \boldsymbol{K'}$ satisfies the Fermion doubling theorem. For a 3D strong topological insulator there exists an odd number of points in one surface. But, the other Dirac point resides on the opposite surface and as a whole the Fermion doubling is satisfied.

Helicity

For both QSHE and 3D topological insulator, the Dirac Fermionic states at the surface have spin filtering property. Fig. 1.7 (a) shows the helical property of the Dirac mode of a QSHE state.[32] On the surface spin up and spin down moves in opposite direction.

[iv] The simplest dispersion relation at the Fermi surface with non-zero velocity is always linear.

This makes the backscattering process impossible if it does not flip the spin, and thus the surface modes are not affected my Anderson localization.

The spins of the Dirac Fermion in a 3D (strong) topological insulator surface rather moves circularly such that at any point on the fermi circle, the velocity is perpendicular to the spin direction. This property is called the *spin-momentum locking*.

1.3 Graphene

1.3.1 Crystal structure of graphene

Graphene is a 2D allotrope of carbon, which is the 6th element of periodic table. The mostly available form of carbon is ${}^{12}C_6$. The 6 electrons in a single carbon atom are in the quantum state $1s^2 2s^2 2p^2$. The $1s$ orbital to closely bound to the nucleus and irrelevant for chemical bonding. In presence of other atoms, the electrons in $|2s\rangle$ and $|2p\rangle$ hybridize. A hybridization between a $|2s\rangle$ orbital and n $|2p\rangle$ orbitals is called a sp^n hybridization.

In the case of graphene, the electron-bonds are sp^2 hybridized. The participating electrons are one $|2s\rangle$ electron, and two $|2p\rangle$ electrons, lets say from $|2p_x\rangle$ and $|2p_y\rangle$ orbitals. For each carbon atom they connect to three carbon atoms by σ bonding. This forms a planar structure, where the angle between the bonds are 120^o. This gives rise to a hexagonal structure, which is similar to a benzine ring. The remaining electrons inside the structure also forms week π bonds, but the average distance between two neighbouring C atoms is 1.42 Å, which lies in between the bond length of σ bond and π bond.

The 3D structure of graphene, commonly known as graphite is formed by several graphene layers on top of each other. They are attached by week van der Waals force which is a much weaker force compared to the σ bonds. Two consecutive graphene layer has a distance of 2.4 times the σ bond length. The first successful extraction of single layered graphene by Novoselov and Geim *et al.*[33,34] and Zhang *et al.*[35] in 2005 opened up the opportunity for many interesting physics.

As shown in Fig. 1.8(a), there are two non-equivalent carbon atoms (marked by A and B) in a hexagonal structure. They combine to form a unit cell. We can chose the primitive lattice vector as

$$\boldsymbol{a}_1 = \frac{a}{2}\left(3, \sqrt{3}\right) \ , \quad \boldsymbol{a}_2 = \frac{a}{2}\left(3, -\sqrt{3}\right) \ , \tag{1.20}$$

where a is the bond length. The reciprocal lattice vectors $\boldsymbol{a}_1^*, \boldsymbol{a}_2^*$, defined by $(\boldsymbol{a}_i \cdot \boldsymbol{a}_j^*) = 2\pi\delta_{ij}$ are

$$\boldsymbol{a}_1^* = \frac{2\pi}{3a}\left(1, \sqrt{3}\right) \ , \quad \boldsymbol{a}_2^* = \frac{2\pi}{3a}\left(1, -\sqrt{3}\right) \ . \tag{1.21}$$

The first Brillouin zone of graphene is also a hexagon in momentum space.

1.3.2 Electronic structure of graphene

In graphene, at low energy, the relevant atomic orbitals are the π bonds formed by $|p_z\rangle$ orbitals, because the bonding energy is close to the Fermi energy. Each of this orbital

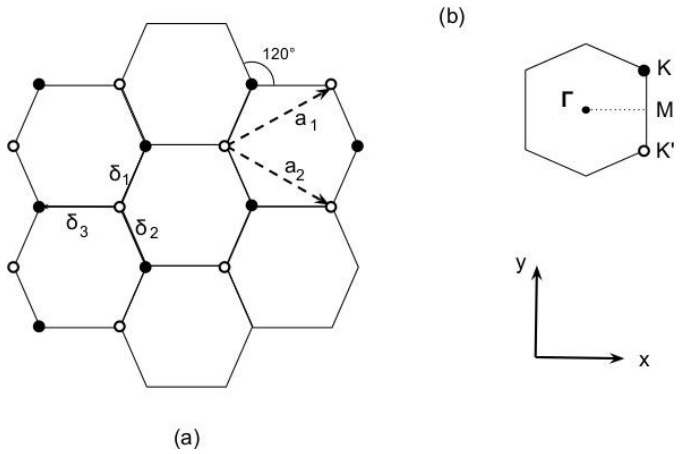

Figure 1.8: Crystal structure of graphene. (a) is the hexagonal structure on grapehen plane. The two non-equivalent atoms are marked by A and B, they combine to form a unit cell. $\boldsymbol{a}_1, \boldsymbol{a}_2$ are the primitive lattice vectors. (b) shows the first Brillouin zone with the two non-equivalent momenta K, K' and the effective origin in momentum space M. See Sec. 1.3.2

can be occupied by two electrons with opposite spins. Here we will discuss the energy bands of π electrons within a tight-binding approach, which was originally calculated for the honeycomb lattice by P. R. Wallace[36] in 1947 The tight-binding approach includes the nearest-neighbour hopping (which, in case of graphene relates one A atom to three B atoms), and correction due to next-nearest-neighbour hopping (relates nearest AA or BB).

Denoting the orbital of ith atom with spin σ as $(i\sigma)$, the tight-binding Hamiltonian can be written as:

$$\hat{H}_{TB} = -t \sum_{<i,j>,\sigma} (a^\dagger_{i\sigma} b_{i\sigma} + H.C.) \; - \; t' \sum_{<<i,j>>,\sigma} (a^\dagger_{i\sigma} a_{i\sigma} + b^\dagger_{i\sigma} b_{i\sigma} + H.C.) \; , \qquad (1.22)$$

where $t \sim 2.8$ eV is the nearest neighbour hopping energy and $0.02t \leq t' \leq 0.2t$,[37] so the next-nearest-neighbour hopping is ~ 0.1 eV. $a^\dagger_{i\sigma}$ and $b^\dagger_{i\sigma}$ are the electron creation operator on sub-lattice A and B of the ith lattice site.

Let us first consider the case with $t' = 0$. We will add this later as correction. The Hamiltonian is block-diagonal in spin space, so for obtaining the band energy, we'll consider only one spin for simplicity. Also it is convenient to write the tight-binding wave function as a spinor with components as amplitude on A and B sub-lattice site within the unit cell labelled by the reference point $\boldsymbol{R}_i$. Without loss of generality, we can chose $\boldsymbol{R}_i$ to be the coordinate of a A site. Then the tight-binding wave-function has the form (without spin index)

$$\begin{pmatrix} \Psi_A \\ \Psi_B \end{pmatrix} = \sum_i e^{i\boldsymbol{k}\cdot\boldsymbol{R}_i} \begin{pmatrix} a^\dagger_i e^{-i\boldsymbol{k}\cdot\boldsymbol{\delta}_1/2} \\ b^\dagger_i e^{i\boldsymbol{k}\cdot\boldsymbol{\delta}_1/2} \end{pmatrix} \; , \qquad (1.23)$$

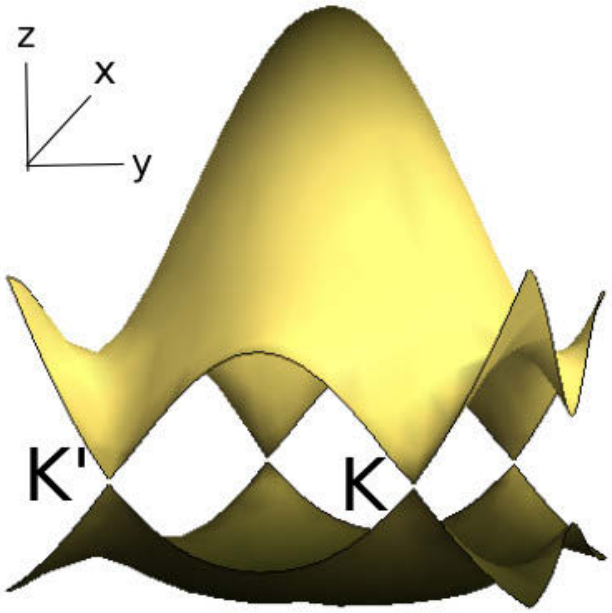

Figure 1.9: Schematic of Band dispersion in graphene. Here $t' = 0.2t$. For the case of $t' = 0$, the two upper and lower band touches at the two pints $\boldsymbol{K}$ and $\boldsymbol{K}'$

where $\boldsymbol{\delta}_1$ is the vector from A to B sublattice (Fig. 1.8) and $\boldsymbol{k}$ is the Bloch momenta. The resulting Hamiltonian has the off-diagonal form ($t' = 0$):

$$\hat{H}_{TB} = \begin{pmatrix} 0 & \Delta_{\boldsymbol{k}} \\ \Delta^*_{\boldsymbol{k}} & 0 \end{pmatrix} , \qquad \Delta_{\boldsymbol{k}} = -t(e^{i\boldsymbol{k}\cdot\boldsymbol{\delta}_1} + e^{i\boldsymbol{k}\cdot\boldsymbol{\delta}_2} + e^{i\boldsymbol{k}\cdot\boldsymbol{\delta}_3}) , \tag{1.24}$$

where $\boldsymbol{\delta}_i$ s are shown in Fig. 1.8, and they cen be expressed as:

$$\boldsymbol{\delta}_1 = \frac{a}{2}(1, \sqrt{3}) , \qquad \boldsymbol{\delta}_2 = \frac{a}{2}(1, -\sqrt{3}) , \qquad \boldsymbol{\delta}_3 = -a(1, 0) . \tag{1.25}$$

The resulting band dispersion has the form:

$$\epsilon_{\boldsymbol{k}} = \pm|\Delta_{\boldsymbol{k}}| = \pm\sqrt{3 + f(\boldsymbol{k})} , \tag{1.26}$$

with

$$f(\boldsymbol{k}) = 2\cos\left(\sqrt{3}k_y a\right)\cos\left(\frac{3k_x a}{2}\right)\cos\left(\frac{\sqrt{3}k_y a}{2}\right) . \tag{1.27}$$

Dirac points

From the dispersion relation, we can find the points in the BZ, for which $\epsilon_{\boldsymbol{k}} = 0$. This points are called the Dirac points because the physics close to this points are governed

by Dirac equations. We find the two corresponding points

$$\boldsymbol{K}, \boldsymbol{K}' = \left(\frac{2\pi}{3a}, \pm\frac{2\pi}{3\sqrt{3}a}\right). \tag{1.28}$$

It can also be noted that

$$\boldsymbol{K}' = -\boldsymbol{K} - \boldsymbol{a}_1^* - \boldsymbol{a}_2^* \equiv -\boldsymbol{K} \ . \tag{1.29}$$

Next-nearest-neighbour correction

For a non-zero t', the full Hamiltonian has dispersion relation

$$\tilde{\epsilon}_{\boldsymbol{k}} = \pm|\Delta_{\boldsymbol{k}}| = \pm\sqrt{3 + f(\boldsymbol{k})} - t' f(\boldsymbol{k}) \ . \tag{1.30}$$

but, as $\partial_{\boldsymbol{k}} f(\boldsymbol{k}) = 0$, near the Dirac points the physics is dominated by the nearest-neighbour term. The presence of non-zero t' brakes the electron-hole symmetry close to the Dirac point, because $f(\boldsymbol{K}, \boldsymbol{K}') = -3$ and it shifts the zero of the energy. The band-dispersion is shown in Fig. 1.9.

1.3.3 Dirac Fermions

To understand the physics close to the Dirac points $\boldsymbol{K}$, we can expand the Hamiltonian (1.24) and its band dispersion (1.26) around that point. If we set $\boldsymbol{q} = \boldsymbol{k} - \boldsymbol{K}$, then upto the first order in $q = |\boldsymbol{q}|$ we get (apart from a phase factor):

$$\begin{aligned} \Delta_{\boldsymbol{K}}(\boldsymbol{q}) &\simeq \frac{3ta}{2}(q_x - iq_y) \\ &= \hbar v_F (q_x - iq_y) \ , \end{aligned} \tag{1.31}$$

where $v_F \approx 10^6$ m/sec is the Fermi velocity. If we expand around $\boldsymbol{K}'$, we obtain

$$\Delta_{\boldsymbol{K}'}(\boldsymbol{q}) = \hbar v_F (q_x + iq_y) = \Delta_{\boldsymbol{K}}^*(\boldsymbol{q}) \ . \tag{1.32}$$

Actually this means that $\boldsymbol{K}$ and $\boldsymbol{K}'$ are connected by time-reversal, as we discuss below. Combining both, in the basis of $(\Psi_{A+}, \Psi_{B+}, \Psi_{A-}, \Psi_{B-})$, where $\pm$ stand for the two Dirac points $\boldsymbol{K}$ and $\boldsymbol{K}'$, we have the mesoscopic Hamiltonian from (1.24):[38,39]

$$H = \begin{pmatrix} H_+ & 0 \\ 0 & H_- \end{pmatrix}, \tag{1.33}$$

$$H_\pm = -i\hbar v_F (\sigma_x \partial_x \pm \sigma_y \partial_y) \ . \tag{1.34}$$

We note that each of this Hamiltonian $H_\pm$ presents 2D Dirac Fermions with linear dispersion relation

$$E_\pm(\boldsymbol{q}) = \pm\hbar|\boldsymbol{q}| \ . \tag{1.35}$$

Here $\pm$ refers to electron/hole dispersion. If we include the correction due to the next-nearest-neighbour interaction, the dispersion relation becomes:

$$\tilde{E}_\pm(\boldsymbol{q}) = 3t' \pm \hbar|\boldsymbol{q}| \ , \tag{1.36}$$

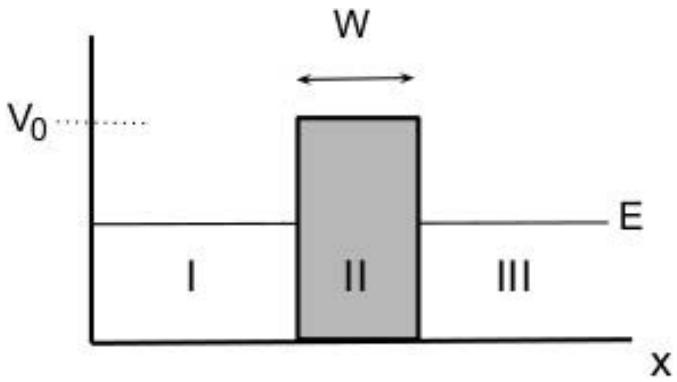

Figure 1.10: The schematic for studying a potential barrier of width W and height V_0 on a x axis of a 2D dirac system. The incident Dirac particle has a energy $E < V_0$.

and hence, the electron-hole symmetry is broken.

The eigenfunction close to $\boldsymbol{K}$ is

$$\psi^{\pm}_{\boldsymbol{K}}(\boldsymbol{q}) = \frac{1}{\sqrt{2}} \begin{pmatrix} e^{-i\phi_{\boldsymbol{q}}/2} \\ \pm e^{i\phi_{\boldsymbol{q}}/2} \end{pmatrix} , \quad \psi^{\pm}_{\boldsymbol{K}'}(\boldsymbol{q}) = \frac{1}{\sqrt{2}} \begin{pmatrix} e^{i\phi_{\boldsymbol{q}}/2} \\ \pm e^{-i\phi_{\boldsymbol{q}}/2} \end{pmatrix} , \tag{1.37}$$

where $\phi_{\boldsymbol{q}} = \tan^{-1}(q_x/q_y)$. This wave-function, although we neglected real spin so far, contains hint about the spin-1/2 nature of the excitation. That can be seen from the fact that, if $\boldsymbol{q}$ rotates once around the Dirac point, the wave-function gets a overall negative sign, as a characteristics of a spin-1/2 particle.

We notice that the wave-functions in Eq. (1.37) are related by time-reversal symmetry. If we set the origin of coordinates in momentum space at the M point of the BZ (see Fig. 1.8), time reversal becomes a reflection with respect to the k_x axis, ie, $(k_x, k_y) \to (k_x, -k_y)$. Graphene also has inversion symmetry.

Chirality

Helicity (which is the same as chirality for mass-less particles) operator is the projection of momentum along the spin direction:

$$\hat{h} = \frac{1}{2}\boldsymbol{\sigma}\frac{\boldsymbol{p}}{|\boldsymbol{p}|} . \tag{1.38}$$

In case of graphene, we can define helicity as projection to the pseudo spin (AB sublattice space) direction. Then it can be shown that

$$\hat{h}\psi^{\pm}_{\boldsymbol{K}} = \pm\frac{1}{2}\psi^{\pm}_{\boldsymbol{K}} . \tag{1.39}$$

and the sign is opposite for $\boldsymbol{K}'$. That means that electron and hole has well defined chirality. If we include the correction due to non-zero t', helicity remains no longer a good quantum number.

1.3.4 Klein tunneling and confinement

Klein paradox[40–44] is a phenomena which prevents confinement of Dirac fermions by potential barrier. If we have a potential barrier of width W and height V_0, as shown in Fig. 1.10, we can compute the total transmission coefficient. For simplicity, we are restricting ourselves to only $\boldsymbol{K}$ point. In this geometry also the momentum along y direction q_y can be taken constant. We can write the wave-function in region I as incoming wave + reflected wave for incident energy E:

$$\psi_I = \frac{1}{\sqrt{2}} \begin{pmatrix} 1 \\ se^{i\phi} \end{pmatrix} e^{i(q_x x + q_y y)} + \frac{r}{\sqrt{2}} \begin{pmatrix} 1 \\ se^{i(\pi-\phi)} \end{pmatrix} e^{i(-q_x x + q_y y)} \ , \tag{1.40}$$

where r is the reflection amplitude and $\phi = \tan^{-1}(q_x/q_y)$. In the region II, it can be written as

$$\psi_{II} = \frac{a}{\sqrt{2}} \begin{pmatrix} 1 \\ s'e^{i\phi'} \end{pmatrix} e^{i(q'_x x + q_y y)} + \frac{r}{\sqrt{2}} \begin{pmatrix} 1 \\ s'e^{i(\pi-\phi')} \end{pmatrix} e^{i(-q'_x x + q_y y)} \ , \tag{1.41}$$

where $q'_x = \sqrt{(V_0 - E)^2/v_F^2 - q_y^2}$ and $\phi = \tan^{-1}(q_x/q_y)$. And finally in region III

$$\psi_{III} = \frac{t}{\sqrt{2}} \begin{pmatrix} 1 \\ se^{i\phi} \end{pmatrix} e^{i(q_x x + q_y y)} \ , \tag{1.42}$$

where $s = \mathbf{sgn}(E)$ and $s' = \mathbf{sgn}(E - V_0)$ denotes whether it is an electron or hole. One can compute the total transmission coefficient by matching the wave-functions at the boundaries. As Dirac equation is first order, there is no need to match derivatives like the schrödinger equation.

In the limit of $V_0 \gg E$, the transmission coefficient has the following form:[45]

$$T(\phi) \simeq \frac{\cos^2\phi}{1 - \sin^2\phi\cos^2(Wq_x)} \ . \tag{1.43}$$

From this equation, it is evident that the transmission is exact at normal incident. This phenomena is called the Klein tunneling. But, for non-zero angle, it is possible to slow down the electron.[46] We also discuss the effect of non-zero incident angle in case of a super-conducting barrier in Chapter 6.

Because of Klein tunneling it is not possible to confine Dirac Fermion by potential barrier. This is because of the fact that, Dirac fermions can tunnel as a hole. As we have seen in Eq. (1.40) - Eq. (1.42), an incident electron tunnels through a hole in region II, where $s' = -1$ for $V_0 > E$. Also, it is related to the fact that, in graphene helicity is a good quantum number. But, to reflect back, helicity must be reversed. So, as long as there is no term breaking the symmetry, back-scattering is forbidden.

Also, because of the possibility of tunneling through a hole channel, the Andreve reflection process in graphene differs from a usual metal case. We discuss this in Chapter 6.

One of the way for confinement in grapehene is to apply magnetic field. It turns out that within a magnetized region the wave-function of the Dirac particles in graphene decays exponentially. We consider in Chapter 5 a finite magnetic ring. Because of the back-scattering from the ring, there are formation of quasi bound state. In the limit of infinitely thick ring, one can achieve confinement of Dirac particles. This has been discussed in details in Ref 47 and 48.

1.4 Discussion

In this chapter we reviewed the physics of topological insulator and graphene. We started from band structure and arrived at an effective Dirac Hamiltonian describing the systems. Although the electronic transport of both the surface of a 3D TI and un-doped graphene are described in a similar manner by a Dirac equation, there are fundamental physical differences in these two systems. TI is rather a phase of matter which has the signature of gap-less Dirac modes at the surface. These modes are protected by the bulk topology, that means a small (time-reversal invariant) impurity can not destroy these gap-less modes. Although different available TI materials have completely different band-structure in the bulk, the surface modes are very similar and can be described by 2D Dirac surface theory. Graphene, on the contrary, has bulk band structure resembling Dirac dispersion at special points of its BZ. These modes are not protected by any topological invariant and can easily be gapped by on-site potential.

Also, the graphene Hamiltonian (1.33) close to the Dirac points have Dirac like form in a pseudo-spin space, which is defined by the A and B sub-lattices. Because of the valley (K, K') and sub-lattice degeneracy, graphene is like 1/4th of a 2D Dirac system. Actually it is possible to have a 2D topological phase in graphene by the action of spin-orbit interaction.

But, while considering transport and interactions, the two system can often be described similarly. For eg, in the case of an applied magnetic field or with magnetisation, both systems can be described by a unified Hamiltonian, which we discuss in Chapter 5. Also, proximity effects in both systems can be modelled similarly, and the result of one system can often be applied to the other system.

Chapter 2

Surface States of 3D Topological Insulator

2.1 Introduction

For a 3D TI with topologically nontrivial surface states, the first predicted material group was Bi_xSb_{1-x}.[49] These surface states were observed[50] in Angle-Resolved Photo-Emission Spectroscopy (ARPES).[i] But these materials are not very good insulator in the bulk (has a small energy gap), so the transport through the gapless surface modes can easily be overtaken by the residual conductivity of the bulk. Also they have rather complicated surface states. More recently Zhang *et al.*[51] theoeretically predicted Bi_2Te_3, Bi_2Se_3 and Sb_2Te_3 as 3D TI with large bulk energy gap ($\sim$0.3 eV) and topologically non-trivial surface state with single Dirac cone. These has been confirmed ARPES experiments as well.[52,53] We will discuss the surface state of these materials in the next chapter.

In this chapter, in Section 2.1 we discuss the topological insulator property for Bi_2Se_3 like material and introduce a low energy model Hamiltonian (around thr TR invariant Γ point) for the topologically nontrivial surface states in these materials. But, for transport experiment, to reduce the contribution of the bulk, it is useful to consider mesoscopic samples, where the surface-to-volume ratio is more advantageous. In particular, thin-film geometries[54,55] and quasi-1D nanowires ("ribbons")[56–59] have been studied experimentally. So, we describe surface states of these geometries in the rest of the chapter.

[i] Angle-resolved photo-emission spectroscopy (ARPES) is a direct experimental technique to observe the the density of single-particle electronic excitations in the reciprocal space of solids. ARPES is one of the most direct methods of studying the electronic structure of the surface of solids. ARPES gives information on the direction, speed and scattering process of valence electrons in the sample being studied (usually a solid). This means that information can be gained on both the energy and momentum of an electron, resulting in detailed information on band dispersion and Fermi surface. This technique is a refinement of ordinary photo-emission spectroscopy.

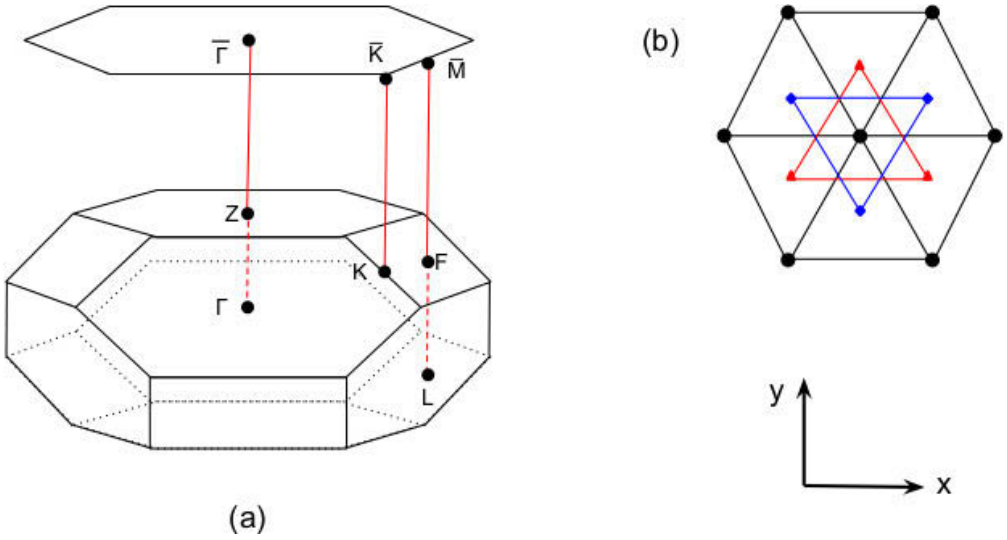

Figure 2.1: (a) Brillouin zone of Bi_2Se_3 and its projection to 2D surface momenta. Different TR inequivalent points are shown. (b) Projection of the crystal structure of Bi_2Se_3 on $x-y$ plane. The red, blue and black corners are projections of the positions of different atoms that define the lattice structure.

2.2 Band Inversion and TI State in Bi_2Se_3 like Materials

The non-trivial topological properties of Bi_2Se_3 , Bi_2Te_3 and Sb_2Te_3 were first investigated by Zhang *et al* (Ref. 51) and later confirmed by ARPES experiments.[52,53] The guiding principle to find such materials was "band inversion", as we discussed in the last chapter, if the valence and conduction band has opposite parities and a band inversion takes place while tuning a physical parameter (like spin-orbit coupling), then there is a possibility that the material is a TI .

All the three materials Bi_2Se_3 , Bi_2Te_3 and Sb_2Te_3 have rhombohedral crystal structure with D^5_{3d} as the crystal symmetry group. A projection of the crystal structure of Bi_2Se_3 is shown in Fig 2.1(b), which has following symmetries:

1. A threefold rotation R_3 along z direction.
2. A twofold rotation R_2 along x axis.
3. Inversion symmetry P for $x \to -x$, $y \to -y$ and $z \to -z$, and
4. Time reversal symmetry $T = i\sigma_2 K$, where σ_2 is the second Pauli matrix acting in spin space and K is the complex conjugation operator.

Ab initio calculations for different crystal parameters are obtained in Ref. 60. The band structure of Bi_2Se_3 has been obtained in Ref. 51 and shown in Fig 2.2. for the case

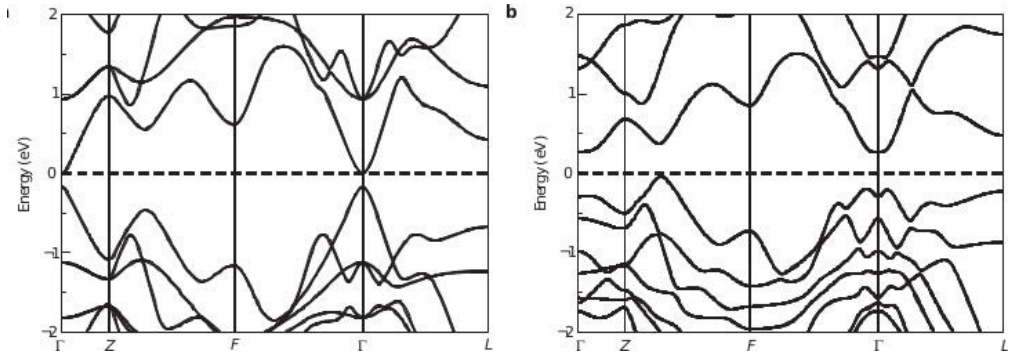

Figure 2.2: Band structure for Bi_2Se_3 without (a) and with (b) spin orbit coupling. The dashed line indicates the Fermi level. With spin orbit coupling it shows a anti-crossing feature. Figure from Ref. 51

without and with spin orbit coupling. Also a bulk energy gap of magnitude 0.3 eV is obtained which matched experimental results.[61,62] By comparing the two figures 2.2(a) and 2.2(b), one can see that there is a anti-crossing feature induced around the Γ ($\boldsymbol{k} = 0$) point by the spin orbit coupling. Which indicates a possible band inversion and suggests that Bi_2Se_3 is a non-trivial insulator.

To verify the possibility one can follow the prescription given by Fu and Kane for calculating Z_2 invariant.[49] In the presence of inversion symmetry parity is a good quantum number and the Z_2 invariants can be determined from the knowledge of the parity of the occupied band eigenstates at the time-reversal invariant momenta points (Γ_i) in the Brillouin zone. Specifically, the Z_2 invariants determined by the quantities:

$$\delta_i = \prod_{m=1}^{N} \xi_{2m}(\Gamma_i) \ . \tag{2.1}$$

Here, $\xi_{2m}(\Gamma_i) = \pm 1$ is the parity eigenvalue of the $2m$th occupied energy band at Γ_i. Because of inversion symmetry, bands can be indexed by parity eigenvalues. Also, $\xi_{2m} = \xi_{2m-1}$ between Kramer's degenerate partners. The product involves the $2N$ occupied bands. The Z_2 invariant $\nu_0 = 0, 1$ for a strong TI is determined from the following identity:

$$(-1)^{\nu_0} = \prod_i \delta_i \ . \tag{2.2}$$

For Bi_2Se_3 , explicit calculation shows that[51] at one of the time reversal invariant point, the Γ ($\boldsymbol{k} = 0$) point, the parity of the highest valence bond changes in the presence of spin orbit coupling. Without spin-orbit coupling Bi_2Se_3 is a trivial insulator (with $\nu_0 = 0$), and so the Z_2 invariant becomes $\nu_0 = 1$ in presence of spin-orbit coupling. So, Bi_2Se_3 is a strong TI with spin-orbit coupling.

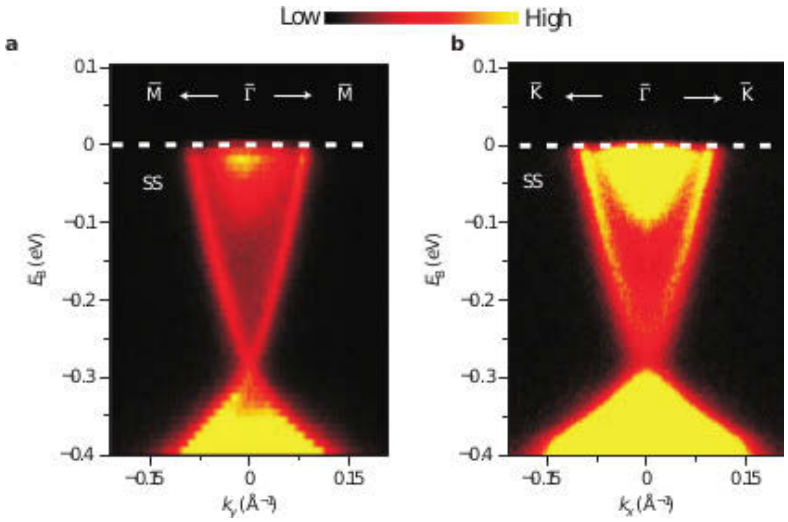

Figure 2.3: Electron dispersion data for High-resolution ARPES measurements of surface electronic band dispersion on Bi_2Se_3 (111) around the $\bar{\Gamma}$ point along (a)$\bar{\Gamma} - \bar{M}$, (b)$\bar{\Gamma} - \bar{K}$ momentum space cuts. The momentum distribution curves corresponding to (a) suggest that two surface bands converge into a single Dirac point at $\bar{\Gamma}$. (Figure from Ref. 52)

Topological surface state

Experimentally Xia *et al.* (Ref. 52) confirmed the existence of gap-less surface states. Fig 2.3 shows the High-resolution ARPES measurements of surface electronic band dispersion on Bi2Se3(111). Electron dispersion data measured with an incident photon energy of 22 eV near the $\bar{\Gamma}$[ii] along two different momentum cross section aroung the $\bar{\Gamma}$ point.

2.2.1 Model Hamiltonian for TI

For better understanding and quantitative predictions for the properties and phenomenon of TI , it is extremely useful to construct a model Hamiltonian for such system describing its essential properties. The model Hamiltonian for the 2D TI HgTe was developed by Bernevig, Hughes and Zhang[14] and was successfully applied for the helical edge sates and the properties under applied magnetic field.

From microscopic consideration it can be realised that[51] the band inversion in Bi_2Se_3 occurs between two hybridized p_z orbitals of opposite parities, of which one belongs to the Se ($|P2_z^- \uparrow (\downarrow)\rangle$) atom and one to the Bi atom ($|P1_z^+ \uparrow (\downarrow)\rangle$). Where $\pm$ denotes the parity of this bands. In the absence of spin orbit coupling, due to the effet of chemical bonding in this molecule and crystal field splitting, $|P2_z^- \uparrow (\downarrow)\rangle$ is the higest valence band and $|P1_z^+ \uparrow (\downarrow)\rangle$ is the lowest conduction band. If the spin orbit coupling strength exceeds certain threshold, these two bands invert at the Γ point and $|P2_z^- \uparrow (\downarrow)\rangle$ becomes the lowest conduction band and $|P1_z^+ \uparrow (\downarrow)\rangle$ becomes the highest

[ii] $\bar{\Gamma}$ is the projection of the time reversal invariant Γ point on a 2D Brillouin zone, shown in Fig 2.1 (b)

M_0 (eV)	A_1 (eVÅ)	A_2 (eVÅ)	B_1 (eVÅ^2)
3.33	2.26	-0.0083	5.74
B_2 (eVÅ^2)	C (eV)	D_1 (eVÅ^2)	D_2 (eVÅ^2)
30.4	-0.28	6.86	44.5

Table 2.1: Parameter values in Eq. (2.4) appropriate for Bi_2Se_3 (taken from Ref. 63).

valence band. Because of the inversion of two bands of opposite parity, a trivial insulator Bi_2Se_3 becomes a non-trivial insulator.

Based on this 4 band structure (including spins), a low energy Hamiltonian can be contructed around Γ point by considering all the symmetries of the system.[51,63] The different parameters of the Hamiltonian can then be obtained by fitting with the band structure obtained by *ab initio* calculaion. In the basis of ($|P1_z^+ \uparrow\rangle$, $|P2_z^- \uparrow\rangle$, $|P1_z^+ \downarrow\rangle$, $|P2_z^- \downarrow\rangle$), denoting Pauli matrices $\boldsymbol{\sigma}$ in spin space and $\boldsymbol{\tau}$ in parity / orbital space, and keeping terms only up to order $\boldsymbol{k}^2$, the Hamiltonian has the form of a 3D Dirac Hamiltonian with a kinetic identity term $\epsilon_0(\boldsymbol{k})$ and $\boldsymbol{k}$ dependent mass term:

$$\begin{aligned} H_b'(\boldsymbol{k}) &= \epsilon_0(\boldsymbol{k}) I_{4\times 4} + \begin{pmatrix} M(\boldsymbol{k}) & A_1 k_z & 0 & A_2 k_- \\ A_1 k_z & -M(\boldsymbol{k}) & A_2 k_- & 0 \\ 0 & A_2 k_+ & M(\boldsymbol{k}) & -A_1 k_z \\ A_2 k_+ & 0 & -A_1 k_z & -M(\boldsymbol{k}) \end{pmatrix} , \\ &= \epsilon_0(\boldsymbol{k})\sigma_0\tau_0 + M(\boldsymbol{k})\sigma_0\tau_z + A_1 k_z \sigma_z\tau_x + A_2\tau_x(k_x\sigma_x + k_y\sigma_y) , \end{aligned} \tag{2.3}$$

with $\epsilon_0 = C + D_1 k_z^2 + D_2(k_x^2 + k_y^2)$, $M = M_0 - B_1 k_z^2 - B_2(k_x^2 + k_y^2)$, $k_\pm = k_x \pm i k_y$ and $\sigma_\pm = (\sigma_x \pm \sigma_y)/2$. The model parameters for Bi_2Se_3 have been determined from first principles,[51,63] and the latest date from Ref. 63 are shown in Table 2.1. From this model one obtains the surface modes which are massless Dirac modes. We have derived this in the context of taking infinite thickness limit of TI film geometry in following section.

This Hamiltonian is equivalent to the following with an unitary transformation U (keeping up to order $\boldsymbol{k}^2$),

$$\begin{aligned} H_b &= U^\dagger H_b' U = \epsilon_0(\boldsymbol{k}) I_{4\times 4} + \begin{pmatrix} M(\boldsymbol{k}) & -iA_1 k_z & 0 & A_2 k_- \\ iA_1 k_z & -M(\boldsymbol{k}) & A_2 k_- & 0 \\ 0 & A_2 k_+ & M(\boldsymbol{k}) & -iA_1 k_z \\ A_2 k_+ & 0 & iA_1 k_z & -M(\boldsymbol{k}) \end{pmatrix} , \\ &= \epsilon_0(\boldsymbol{k})\sigma_0\tau_0 + M(\boldsymbol{k})\sigma_0\tau_z + A_1 k_z\sigma_0\tau_y + A_2\tau_x(k_x\sigma_x + k_y\sigma_y) , \end{aligned} \tag{2.4}$$

with $U = \mathrm{Diag}(1, -i, -i, 1)$. This Hamiltonian, introduced by Liu *et al.*[63] is used frequently in the literature. We will also use this Hamiltonian, although physically the two Hamiltonians (2.3) and (2.4) are the same.

This effective Hamiltonian is very useful while considering low-energy physics in TI . In the rest of the chapter we will consider dispersion and spin texture of TI in different

geometries from this low-energy Hamiltonian.

2.3 Surface States of TI Thin Film

As discussed in the introduction, for transport experiments thin film geometry is more convenient for higher surface to bulk ratio.[54,55] In this section we discuss the surface state of a thin film TI . Later in Chapter 4 we discuss the effect of electron-phonon coupling in this geometry for obtaining the resistivity.

In order to find the surface states in the film geometry, we follow the usual strategy.[51,63,64] For a surface perpendicular to z direction, k_x, k_y are still good quantum numbers, but not k_z. By substituting k_z by $-i\partial_z$ in Eq. (2.4), one gets an one dimentional Schrödinger like equation with k_x, k_y appearing as parameters.

$$H_b = H_0(k_\perp = 0) + H' \ , \tag{2.5}$$

where,

$$H_0 = \begin{pmatrix} h(k_z) & 0 \\ 0 & h(k_z) \end{pmatrix} \ , \tag{2.6}$$

is the part of Eq. (2.4) with $k_x, k_y = 0$. We have

$$h_0(k_z) = \begin{pmatrix} \epsilon_0(k_z) + M_0 - B_1 k_z^2 & -iA_1 k_z \\ iA_1 k_z & \epsilon_0(k_z) - M_0 + B_1 k_z^2 \end{pmatrix} \ , \tag{2.7}$$

and,

$$H' = D_2 k_\perp^2 - B_2 k_\perp^2 \tau_z \sigma_0 + A_2 \tau_x (k_x \sigma_x + k_y \sigma_y) \ . \tag{2.8}$$

We note that $h(k_z)$ is diagonal in spin space, thus its eigenstates conserve spin. We write the general eigenstates of $h(k_z)$ in spin state σ and with energy E_0 as:

$$h(-i\partial_z)\Psi_\sigma = E_0 \Psi_\sigma \ . \tag{2.9}$$

We make a trial solution,

$$\Psi \propto \Psi_\eta e^{-\eta z} \ , \tag{2.10}$$

to get,

$$\begin{pmatrix} C - E_0 + M_0 - D_- \eta^2 & A_1 \eta \\ -A_1 \eta & C - E_0 - M_0 - D_+ \eta^2 \end{pmatrix} \Psi_\eta = 0 \ , \tag{2.11}$$

where $D_\pm = D_1 \pm B_1$. And, we get 4 solutions in η, from

$$\begin{aligned} &\det(h(i\eta) - E_0) = 0 \\ \text{or,} \quad &\tilde{A}\eta^4 + \tilde{B}\eta^2 + \tilde{C} = 0 \ , \end{aligned} \tag{2.12}$$

which gives $\eta(E_0) = \pm\eta_1, \pm\eta_2$ where

$$\eta_1 = \sqrt{\frac{-\tilde{B} + \sqrt{\tilde{B}^2 - 4\tilde{A}\tilde{C}}}{2\tilde{A}}} \quad \text{and} \quad \eta_2 = \sqrt{\frac{-\tilde{B} - \sqrt{\tilde{B}^2 - 4\tilde{A}\tilde{C}}}{2\tilde{A}}} \ , \tag{2.13}$$

with

$$\begin{aligned}\tilde{A} &= D_1^2 - B_1^2 = D_+ D_- \\ \tilde{B} &= A_1^2 - 2(M_0 B_1 + D_1(C - E_0)) \\ \tilde{C} &= (E_0 - C)^2 - M_0^2 \ . \end{aligned} \tag{2.14}$$

So, a general solution can be written as

$$\Psi = \sum_{\alpha=1,2} \sum_{\beta=\pm} c_{\alpha\beta} \psi_{\alpha\beta} e^{-\beta \eta_\alpha z} \ , \tag{2.15}$$

where the $\psi_{\alpha\beta}$ are given by,

$$\psi_{\alpha\beta} = \begin{pmatrix} E_0 - C + M_0 + D_+ \eta_\alpha^2 \\ -A_1 \beta \eta_\alpha \end{pmatrix} \ . \tag{2.16}$$

Now, if the thin film has a width of L and two surfaces at $z = \pm L/2$, then applying the boundary condition

$$\Psi = 0 \qquad \text{at} \quad z = \pm L/2 \ . \tag{2.17}$$

we get two transcendental equations:

$$\begin{aligned} \frac{(E_0 - C + M_0 + D_+ \eta_1^2)\eta_2}{(E_0 - C + M_0 + D_+ \eta_2^2)\eta_1} &= \frac{\tanh(\eta_2 L/2)}{\tanh(\eta_1 L/2)} \\ \text{or} \quad \frac{(E_0 - C + M_0 + D_+ \eta_1^2)\eta_2}{(E_0 - C + M_0 + D_+ \eta_2^2)\eta_1} &= \frac{\tanh(\eta_1 L/2)}{\tanh(\eta_2 L/2)} \ , \end{aligned} \tag{2.18}$$

from which we get the Γ point energies $E_0^{(+)}$, $E_0^{(-)}$ and the corresponding eigenstates Ψ_+ and Ψ_-:

$$\Psi_+ = \mathcal{N}^+ \begin{pmatrix} D_+ \eta^+ f_-^+ \\ A_1 f_+^+ \end{pmatrix} \qquad \Psi_- = \mathcal{N}^- \begin{pmatrix} D_+ \eta^- f_+^- \\ A_1 f_-^- \end{pmatrix} \ , \tag{2.19}$$

where $\mathcal{N}^\pm$ are the normalization constants,

$$\begin{aligned} f_+^\pm(z) &= \frac{\cosh(\eta_1 z)}{\cosh(\eta_1 L/2)} - \frac{\cosh(\eta_2 z)}{\cosh(\eta_2 L/2)}\bigg|_{E=E_0^\pm} \\ f_-^\pm(z) &= \frac{\sinh(\eta_1 z)}{\sinh(\eta_1 L/2)} - \frac{\sinh(\eta_2 z)}{\sinh(\eta_2 L/2)}\bigg|_{E=E_0^\pm} \ , \end{aligned} \tag{2.20}$$

and

$$\begin{aligned} \eta^+ &= \frac{\eta_1^2 - \eta_2^2}{\eta_1 \coth(\eta_1 L/2) - \eta_2 \coth(\eta_2 L/2)}\bigg|_{E=E_0^+} \\ \eta^- &= \frac{\eta_1^2 - \eta_2^2}{\eta_1 \tanh(\eta_1 L/2) - \eta_2 \tanh(\eta_2 L/2)}\bigg|_{E=E_0^-} \ . \end{aligned} \tag{2.21}$$

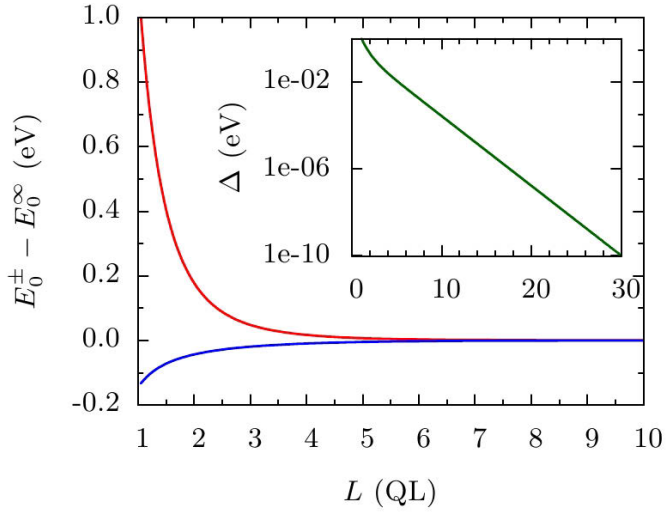

Figure 2.4: E_0^+, E_0^- and Δ as a function of L in units of quantum layers (1 QL = 9.5 Å).

We write the eigenstates of H_0 as (the notation is explained below):

$$\Phi_\uparrow^+ = \begin{pmatrix} \Psi_+ \\ 0 \end{pmatrix}, \Phi_\uparrow^- = \begin{pmatrix} \Psi_- \\ 0 \end{pmatrix}, \Phi_\downarrow^+ = \begin{pmatrix} 0 \\ \Psi_+ \end{pmatrix}, \Phi_\downarrow^- = \begin{pmatrix} 0 \\ \Psi_- \end{pmatrix}, \tag{2.22}$$

whose energies are respectively $E_0^+, E_0^-, E_0^-, E_0^+$.

Now, the effective surface Hamiltonian with finite k_x, k_y is obtained by projecting the Hamiltonian (2.4) in this basis:[51,63,64]

$$H_{\text{eff}} \equiv \int_{-L/2}^{L/2} dz\, (\Phi_\uparrow^+, \Phi_\uparrow^-, \Phi_\downarrow^+, \Phi_\downarrow^-)^\dagger (H_0 + H')(\Phi_\uparrow^+, \Phi_\uparrow^-, \Phi_\downarrow^+, \Phi_\downarrow^-)\ , \tag{2.23}$$

explicitly it is given by a 2×2 block diagonal matrix:

$$\begin{aligned} H_{\text{eff}} \quad = \quad & E_0 I_{4\times4} + D_2 k^2 I_{4\times4} + \\ & \begin{pmatrix} \frac{1}{2}\Delta - B_2 a_z k^2 & -A_2 W k_- & 0 & 0 \\ -A_2 W^* k_+ & -\frac{1}{2}\Delta - B_2 b_z k^2 & 0 & 0 \\ 0 & 0 & -\frac{1}{2}\Delta - B_2 b_z k^2 & -A_2 W^* k_- \\ 0 & 0 & -A_2 W k_+ & \frac{1}{2}\Delta - B_2 a_z k^2 \end{pmatrix}, \end{aligned}$$

with $E_0 = (E_0^+ + E_0^-)/2$, $\Delta = (E_0^+ - E_0^-)$, $k = \sqrt{k_x^2 + k_y^2}$, $W = \langle \Psi_+ | \tau_x | \Psi_- \rangle$. The width dependence of Δ is shwon in Fig. 2.4, which goes to zero exponentially as the width increases. Neglecting k^2 terms, we have,

$$H_{\text{eff}} = E_0 I_{4\times4} + \begin{pmatrix} \frac{1}{2}\Delta & 0 & 0 & -A_2 W k_- \\ 0 & -\frac{1}{2}\Delta & -A_2 W^* k_- & 0 \\ 0 & -A_2 W k_+ & \frac{1}{2}\Delta & 0 \\ -A_2 W^* k_+ & 0 & 0 & -\frac{1}{2}\Delta \end{pmatrix}. \tag{2.24}$$

Now, we can redefine parity Pauli matrices that exchanges in space of (Ψ_+, Ψ_-) as $\boldsymbol{\tau}$. Combining with the spin Pauli matrices $\boldsymbol{\sigma}$, we can write the effective Hamiltonian as:

$$H_{\text{eff}} = E_0\, I_{4\times4} + \frac{\Delta}{2}\,\tau_z\sigma_0 - A_2W\,\tau_x(k_x\sigma_x + k_y\sigma_y)\ , \tag{2.25}$$

where we have used the fact that with parameters from Ref. 63, W is always real. This has a dispersion relation of massive Dirac Fermions:

$$E(k) = E_0 \pm \sqrt{(A_2Wk)^2 + (\Delta/2)^2}\ . \tag{2.26}$$

2.3.1 Semi-infinite Geometry

We can make the width of the film very large and consider only one surface to obtain an semi-infinite geometry. When $L \to \infty$, assuming both η_i have positive real parts,[iii] $\tanh(L\eta_i/2) = 1$ and both the conditions (2.18) becomes:

$$E_0 - C + M_0 - D_+\eta_1\eta_2 = 0\ . \tag{2.27}$$

Considering (2.12), one can solve for energy, $E_0 = C + D_1M_0/B_1$ and

$$\eta_{1,2} = \sqrt{\frac{A_1^2 + 2M_0D_+D_-/B_1 \mp A_1\sqrt{A_1^2 + 4M_0D_+D_-/B_1}}{-2D_+D_-}}\ . \tag{2.28}$$

Imposing the boundary condition $\Psi(z=0) = 0$ and $\Psi(z\to+\infty) = 0$, the corresponding wave-functions are given in spin space by:

$$\Phi_\uparrow = \begin{pmatrix}\Psi_+\\ 0\end{pmatrix},\quad \Phi_\downarrow = \begin{pmatrix}0\\ \Psi_+\end{pmatrix}, \tag{2.29}$$

with (in parity space)

$$\begin{aligned}\Psi_+ =& \mathcal{N}_0\begin{pmatrix}\sqrt{-D_+/D_-}\\ -1\end{pmatrix}(e^{-\eta_1 z} - e^{-\eta_2 z})\\ \to& \mathcal{N}_0\begin{pmatrix}1\\ -1\end{pmatrix}(e^{-\eta_1 z} - e^{-\eta_2 z}) \quad \text{if} B_1 \gg D_1,\end{aligned} \tag{2.30}$$

where, in the limit $B_1 \gg D_1$ considered in Ref. 63, it becomes an eigenstate of τ_x. With $v_F = A_2\sqrt{1-(D_1/B_1)^2}$, the effective surface Hamiltonian, in the basis $\{\Phi_\uparrow, \Phi_\downarrow\}$ becomes, up to first order in k,

$$H_{\text{surf}} = C + \frac{D_1M_0}{B_1} - v_F(\sigma_xk_x + \sigma_yk_y)\ . \tag{2.31}$$

As expected, for $L\to\infty$, we find $\Phi_\uparrow^+ \to \Phi_\uparrow$, $\Phi_\downarrow^+ \to \Phi_\downarrow$, $\Delta \to 0$, $E_0^\pm \to E_0^\infty$, $A_2W \to v_F$.

Apart from the identity term, this is the Dirac equation in 2D, with the linear dispersion relation

$$E(k) = C + \frac{D_1M_0}{B_1} \pm v_Fk\ . \tag{2.32}$$

[iii] which is true for large L, with the parameters from Table 2.1.

2.4 Surface State of TI Nanowire

Nanowire geometry is another case which has larger surface to bulk ratio and can be useful for surface transport experiments. Quasi-1D nanowires ("ribbons")[56–59] have been studied experimentally. Signatures for Aharonov-Bohm interference effects associated with the topological surface state in Bi_2Se_3 nanowires were reported, [56] cf. also related experiments for Sb_2Te_3 nanowires.[58] In this section we discuss the energy spectrum a TI nanowire by diagonalising the low energy Hamiltonian (2.4) we introduced in the last section.

Although in an infinite sample of TI , gap-less surface mode is guaranteed to exist, the energy spectrum of the surface states of a infinitely long nanowire TI is no longer gap-less. Band structure calculations predict a multi-channel wave-guide where all surface modes are gapped.[65–68] Also, the spin is locked with the surface (spin-surface locking, also discussed in Sec. 1.2.8).

To describe the band structure of a finite-length cylindrical nanowire of radius R and with axis along the z direction, due to rotational symmetry in the xy plane, it is useful to switch to cylindrical coordinates (r, ϕ, z). We write

$$k_x^2 + k_y^2 = -(\partial_x^2 + \partial_y^2) = -\frac{1}{r}\partial_r(r\partial_r) - \frac{1}{r^2}\partial_\phi^2. \tag{2.33}$$

We also note that,

$$k_x\sigma_x + k_y\sigma_y = \begin{pmatrix} 0 & k_- \\ k_+ & 0 \end{pmatrix}, \tag{2.34}$$

and rewrite

$$k_\pm \longrightarrow -ie^{\pm i\phi}(\partial_r \pm \frac{i}{r}\partial_\phi). \tag{2.35}$$

The "cylindrical" Pauli matrices $(\sigma_r, \sigma_\phi, \sigma_z)$ then represent the physical spin operator,[51,63]

$$\begin{aligned} \sigma_r &= \hat{\boldsymbol{e}}_{\boldsymbol{r}} \cdot \boldsymbol{\sigma} = e^{-i\sigma_z\phi/2}\sigma_x e^{i\sigma_z\phi/2} \\ \sigma_\phi &= \hat{\boldsymbol{e}}_{\boldsymbol{\phi}} \cdot \boldsymbol{\sigma} = e^{-i\sigma_z\phi/2}\sigma_y e^{i\sigma_z\phi/2} \ , \end{aligned} \tag{2.36}$$

and we refer to their local expectation values as "spin densities" below. The conserved total angular momentum operator is

$$\hat{J} = e^{-i\sigma_z\phi/2}\left(-i\partial_\phi\right)e^{i\sigma_z\phi/2} = -i\partial_\phi + \sigma_z/2, \tag{2.37}$$

which is conserved because of the cylindrical geometry $[H_b, \hat{J}] = 0$. We can then construct eigenstates of the Hamiltonian which are eigenstates of the angular momentum operator $\hat{J}$ with half-integer eigenvalues $j = m + 1/2$:

$$\Psi(r,\phi) = \sum_m \psi_m(r,\phi) = \sum_m \frac{1}{\sqrt{2\pi}} U_m(r) e^{im\phi}, \tag{2.38}$$

where $U_m(r)$ is the radial function. Here, as k is a good quantum number because of the translation symmetry in z direction, and appears as a parameter in the Hamiltonian

and ins eigenstates. We can diagonalise the Hamiltonian and obtain the eigenstates and eigen-energies for a given k and j.

For the nanowire we then construct the eigenfunctions to the Hamiltonian (2.4) with Dirichlet boundary conditions on the surface, i.e., $\Psi(|\boldsymbol{r}| = R) = 0$. This can be achived by expanding the radial function in the basis:

$$U_m(r) = \sum_\nu u_{m\nu}(r) = \sum_\nu \frac{\sqrt{2} J_m(\gamma_{m\nu} r/R)}{R J_{m+1}(\gamma_{m\nu})} \Theta(R - r), \tag{2.39}$$

which vanishes at $r = R$ and are normalised to:

$$\int_0^R r dr \; u_{m\nu}(r) u_{m'\nu'}(r) = \delta_{mm'}\delta_{\nu\nu'}. \tag{2.40}$$

The quantity $\gamma_{m\nu}$ is the νth zeroes of the Bessel function J_m.

We can now expand the Hamiltonian (2.4) in the orthonormal basis $\{\varrho_{m,\nu}(r,\phi)\}$, that satisfies the proper bounadary condition:

$$\varrho^{\sigma\tau}_{m,\nu}(r,\phi) = \frac{e^{im\phi} J_m(\gamma_{m\nu} r/R)}{\sqrt{\pi} R J_{m+1}(\gamma_{m\nu})} \Theta(R - r) \xi_\sigma \eta_\tau, \tag{2.41}$$

where $m \equiv j - \sigma/2$ as before and ξ_σ, η_τ are basis states respectively in spin and parity space with $\sigma = \pm$ and $\tau = \pm$ are eigenvalues of σ_z and τ_z respectively. The resulting band structure by numerical diagonalisation is shown in Fig. 2.5, which shows a minimal gap Δ_s and because of spin-surface locking we get $\langle \sigma_r \rangle = 0$.

With k denoting the conserved momentum along the wire axis (taken along the z direction), and j the half-integer total angular momentum, the dispersion relation of these modes in a nanowire of radius R (Sec. 3) can be shown to be:[65,66]

$$E_{j,\pm}(k) = \pm\sqrt{(v_1 k)^2 + (j v_2/R)^2}, \tag{2.42}$$

where $\hbar = 1$ throughout and $\pm$ for conduction and valence band, respectively. v_1, v_2 are two Fermi velocities in the z and its perpendicular direction. Note that there is a minimal gap $\Delta_s = v_2/R$ for the surface modes since j is half-integer.

For reasonable values of R, we have $\Delta_s \ll \Delta_b$. These surface states are well reproduced by a model of 2D massless Dirac fermions wrapped onto the cylinder surface under the condition that the spin is tangential to the surface and perpendicular to the momentum (spin-surface locking), following Ref. 65,

$$h^{(j)} = \left(-i v_1 \sigma_y \partial_z - \frac{j v_2}{R} \sigma_z \right) , \tag{2.43}$$

where as extension is important for dealing with boundaries, as we will discuss in the next section.

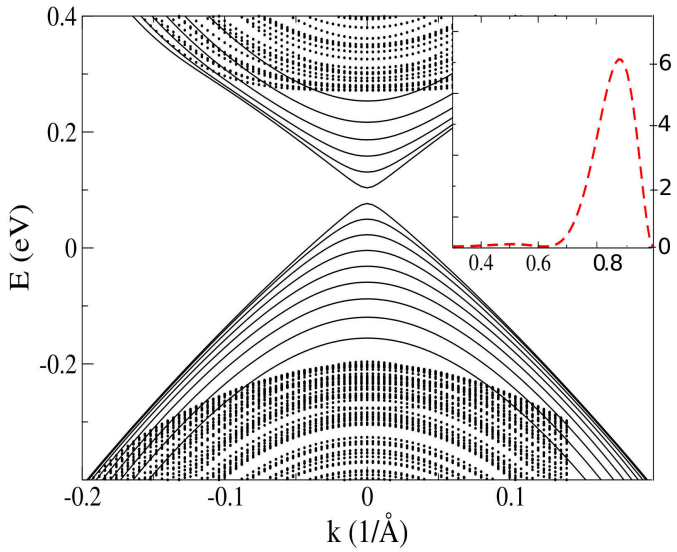

Figure 2.5: Band structure of a TI nanowire with $R = 15\ nm$ obtained by numerical diagonalization of Eq. (2.4). Points refer to bulk states, lines to surface states. Inset: Density ρ (dashed red) and spin density vs radial coordinate (r/R) for the right-moving state $(k, j) = (0.02\ \mathring{A}^{-1}, 1/2)$.

2.5 TI Quantum Dot: Surface states of Finite Nanowire

Experiments probing quantum dot physics in *finite-length* TI nanowires are expected to yield new insights into the exciting physics of TIs, in close analogy to semiconductor nanowires and carbon nanotubes where such experiments have been highly successful.[69,70] This geometry is different from the infinite nanowire because of the presence of the edges of the nanowire. In this section we discuss the band structure of a finite-length nanowire geometry, which forms a TI quantum dot.

We employ three different and independent approaches to understand the system of the cylindrical nanowire of length L and radius R. In this section, starting from the effective low-energy theory of Zhang *et al.* for Bi_2Se_3 (2.4), we have performed detailed numerical calculations for the energy spectrum and the spin texture of the eigenstates. Material parameters were chosen for Bi_2Se_3 as quoted in Ref. 63.

In the next chapter we develop an analytical approach starting from a surface Dirac fermion description has been developed for the same geometry. Most of our numerical results can thereby be quantitatively reproduced within an analytical theory. We have also studied a microscopic tight-binding model (which was first proposed by Fu, Kane, and Mele[71]) for a strong TI in the finite-size nanowire geometry and find qualitatively similar results, which we discuss in Appendix B.

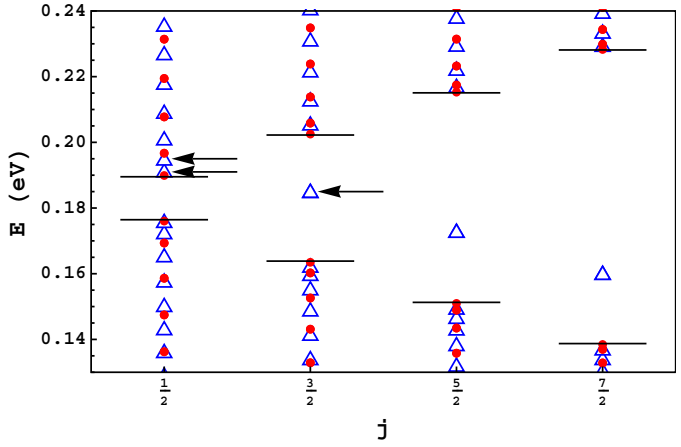

Figure 2.6: Energy spectrum $E_{j,s,\pm}$ from numerical diagonalization of Eq. (2.4) for a cylindrical TI quantum dot with $R = 20\ nm$ and $L = 44\ nm$. Open blue triangles correspond to the numerical results, while filled red circles show the analytical prediction in Eq. (3.26) (in the next chapter). Dashed lines indicate the surface gap for the respective angular momentum (j) mode in an infinitely long nanowire. The spin texture for the zero-momentum state with $j = 1/2$ indicated by the lower left arrow is shown in Fig. 2.7. The spin texture for the next higher state (higher left arrow) is shown in Fig. 2.8. The example of a subgap state (for $j = 3/2$, right arrow) is addressed in Fig. 2.8.

Diagonalisation of Low energy Hamiltonian

For the cylindrical nanowire geometry of length L we construct the eigenfunctions to the Hamiltonian (2.4) with Dirichlet boundary conditions, $\Psi(\boldsymbol{r}) = 0$, on the surface, i.e., for $|z| < L/2$ with $r = R$ (cylinder trunk) and for $|z| = L/2$ with $r < R$ (caps).

This can be achieved by expanding states in a complete orthonormal basis $\{\psi_a(r, \phi, z)\}$, that satisfies these boundary conditions. The quantum numbers $a = (j, \nu, n, \sigma)$ include the half-integer angular momentum j, a radial index $\nu \in \mathbb{N}$, the longitudinal quantum number $n \in \mathbb{N}$, and the spin index $\sigma = \pm$. For $r \leq R$ and $|z| \leq L/2$, the basis is chosen in the form

$$\psi_a(r, \phi, z) = \xi_a(r, \phi, z)\chi_\sigma\eta_\tau \ , \tag{2.44}$$

where $\xi_a(r, \phi, z)$ is the real space orthonormal set that satiesfies the Dirichlet boundary condition ($\xi_a(R, \phi, \pm L/2) = 0$) and has the form:

$$\xi_a(r, \phi, z) = \sqrt{\frac{2}{V}} \sin[\pi n(z/L - 1/2)] e^{im\phi} \frac{J_m(\gamma_{m\nu} r/R)}{J_{m+1}(\gamma_{m\nu})} \ , \tag{2.45}$$

where, as in the case of infinite nanowire (Sec. 2.4) $m \equiv j - \sigma/2$, $V = \pi R^2 L$ is the cylinder volume, and $\gamma_{m\nu}$ denotes the νth zero of the Bessel function J_m [iv]. The χ_σ and

[iv] $J_m(\gamma_{m\nu} r/R) = 0$ at $r = R$ and $\sin[\pi n(z/L - 1/2)] = 0$ at $z = \pm L/2$, thus the function vanishes at the boundary of the cylinder

η_τ are basis states respectively in spin and parity space, where $\sigma = \pm$ and $\tau = \pm$ are eigenvalues of σ_z and τ_z respectively. The basis set (2.45) satisfies the orthonormality relation

$$\int_V d^3\boldsymbol{r}\ \xi_a^*(\boldsymbol{r})\xi_{a'}(\boldsymbol{r}) = \delta_{aa'}. \tag{2.46}$$

Expanding the Hamiltonian H_b [Eq. (2.4)] in this basis, we obtain a matrix representation that allows for numerical calculations in a truncated basis set. Upon increasing the basis set, numerical results for the spectrum turn out to converge rather slowly. We have performed a lattice regularization as in Ref. 1 in order to obtain manageable matrix dimensions. Typically, we achieve convergence with ≈ 8000 basis states for given j.

The solution of the eigenvalue problem then yields the discrete energy spectrum of such a quantum dot, $E = E_{j,s,\pm}$, where $s \in \mathbb{N}$ labels the different states for the conduction or valence ($\pm$) band with given angular momentum j. Taking averages with respect to the corresponding eigenvector $|\Psi_{j,s,\pm}\rangle$ then yields the spatially dependent charge density profile for this state, $\langle\rho\rangle(r,z)$. In addition, one obtains the local spin densities, $\langle\sigma_\alpha\rangle(r,z)$ with $\alpha = r,\phi,z$, and the local parity densities, $\langle\tau_\beta\rangle(r,z)$ with $\beta = x,y,z$. Rotational symmetry implies that all these averages are independent of the angular variable ϕ.

2.5.1 Energy Spectrum and Spin Density

The numerical result for discrete energy spectrum for a TI nanowire dot with $R = 20\ nm$ and $L = 44\ nm$ is shown in Fig. 2.6. The Kramer's degeneracy results in an identical spectrum for $j \to -j$ but with reversed spin and parity (τ_y) directions. We therefore show only the $j > 0$ solutions in Fig. 2.6. Moreover, we focus on the topologically protected surface fermion modes inside the bulk gap Δ_b.

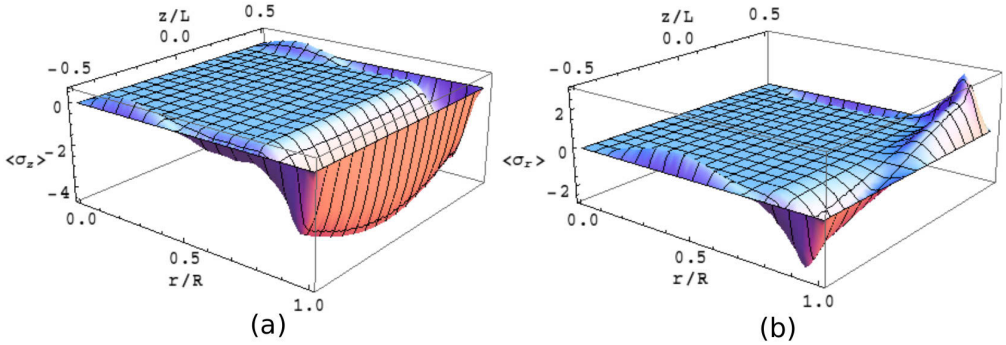

Figure 2.7: (a) and (b) Shows the spin density components $\langle\sigma_z\rangle$ and $\langle\sigma_r\rangle$ respectively in the rz plane, for the zero-momentum state with $j = 1/2$ indicated by the lower left arrow in Fig. 2.6.

There are several noteworthy points about Fig. 2.6. First, it shows that most levels are approximately recovered from the bulk dispersion relation [Eq. (2.42)] by simply

imposing the standard quantization condition

$$k_n = n\pi/L \quad \text{with } n \in \mathbb{N} \tag{2.47}$$

on the longitudinal momentum k. However, here additional states corresponding to $n = 0$ emerge. These *zero-momentum states* are absent for Schrödinger fermions in a box. Note that for each j, there is precisely one $n = 0$ state for the conduction band and one for the valence band. Inspection of the density profiles for these states reveals almost homogeneous charge, spin, and parity densities as a function of the z coordinate. Second, for $j > 1/2$, we find a pair of nearly degenerate *subgap states* inside the surface gap Δ_s. (The near-degeneracy is not visible in Fig. 2.6.) Such a subgap state is localized with equal occupation probability at *both* caps.

Furthermore, electron-hole symmetry is broken under the Zhang model H_b, in contrast to the analytical model we discuss in Chapter. 3, where we found that the energy levels of the finite nanowire are quantised by the condition Eq. (2.47). The electron-hole symmetry breaking is the main reason for the existing discrepancies between Eq. (3.26) and the numerical results, see Fig. 2.6. In fact, we have also carried out additional numerical calculations for an electron-hole symmetric version of Eq. (2.4), where the corresponding results fit almost perfectly to the analytical results of the next chapter. In particular, all subgap states then disappear.

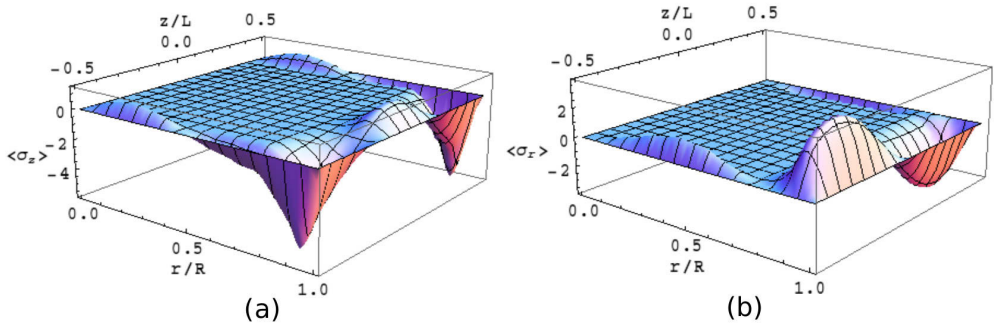

Figure 2.8: (a) and (b) Shows the spin density components $\langle\sigma_z\rangle$ and $\langle\sigma_r\rangle$ respectively in the rz plane, for the next higher level state with $j = 1/2$ indicated by the upper left arrow in Fig. 2.6.

Inspection of the spin densities, $\langle\sigma_\alpha\rangle(r, z)$, and parity densities, $\langle\tau_\beta\rangle(r, z)$, for a given eigenstate $(j, s, \pm)$ yields

$$\langle\sigma_\phi\rangle(r, z) = \langle\tau_x\rangle(r, z) = 0, \tag{2.48}$$

i.e., spin is never oriented in the circumferential direction. In addition, there is now a finite radial spin component within the trunk region ($|z| < L/2$) and a finite z-component within the caps ($|z| = L/2$). Hence, in general, the spin direction for a surface state points out of the surface: *spin-surface locking is broken* in this geometry. This finding is in striking contrast to what happens in an infinite nanowire[66] and for a sphere.[72]

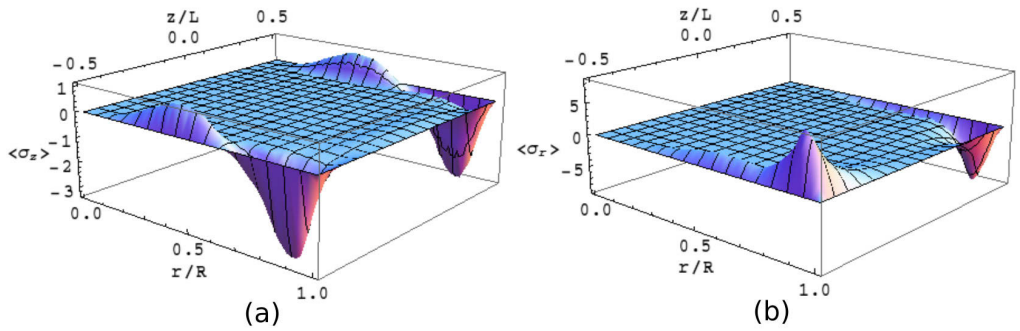

Figure 2.9: Same as Fig. 2.7 but for the "subgap" state with $j = 3/2$ indicated by the right arrow in Fig. 2.6.

Specifically, in the infinite cylinder case, the results corresponding to Fig. 2.7(b) shows $\langle \sigma_r \rangle = 0$ reflecting spin-surface locking.

Figure 2.7 shows the spin density profile for the lowest-lying ("zero-momentum") conduction band state with $j = 1/2$, indicated by the lower left arrow in Fig. 2.6. We indeed find an almost homogeneous spin density profile along the trunk, where spin is mostly aligned along the (negative) z-direction, see Fig. 2.7(a). Also the charge density is practically homogeneous along the z-direction (data not shown). However, there is also a finite radial spin component breaking spin-surface locking, see Fig. 2.7(b). For the cap region, spin is mostly aligned along the radial direction, but again an out-of-plane component, now oriented along the z-axis, is clearly visible. For comparison, Fig. 2.8 shows the respective results for the next higher energy level (upper left arrow in Fig. 2.6). Again we observe that spin-surface locking is violated, while in the infinite cylinder case one finds $\langle \sigma_r = 0 \rangle$ (spin-surface locking).

For $j > 1/2$, our numerical results include an almost degenerate pair of subgap states, where the degeneracy is on top of the Kramer's degeneracy. The charge density is then localized with equal probability near each of the two cylinder caps. A typical example for the spin texture of such a subgap state is shown (for $j = 3/2$) in Fig. 2.9. The out-of-plane spin part is identical on both caps, see Fig. 2.9(a), but the in-plane (radial) component shown in Fig. 2.9(b) has opposite direction.

Comparing our numerical results for parity, charge and spin densities, we find that for each eigenstate, they are linked by a set of general relations. In particular, for the (radially integrated) densities in the trunk region, we find

$$\langle \tau_y \rangle(z) \propto -\langle \sigma_r \rangle(z), \quad \langle \tau_z \rangle(z) \propto \langle \rho \rangle(z). \tag{2.49}$$

Note that in the infinite wire case,[66,73] the parity structure is trivial in the sense that (for large R) the only non-zero component is $\langle \tau_z \rangle$, cf. Sec. 3.2.

In the next chapter we will explain many of the results we obtain for finite nanowire by a surface Dirac fermion theory which is described over the whole cylinder.

2.6 Summary & Discussion

To summarise, in this chapter we have discussed the low energy theory of TI for different experimentally interesting geometries. We started by introducing the general model low energy Hamiltonian for TI close to the Γ point (Eq. 2.3 or Eq. 2.4) based on Bi_2Se_3 type of materials.

We carried out the analytic expression for an effective low energy Hamiltonian (Sec. 2.3) for describing a thin film TI geometry. The resulting dispersion relation is that of massive Dirac Fermions. We later in Chapter 4 study the effect of electron phonon coupling based on this effective Hamiltonian. From this, taking the infinite thickness limit we obtain an effective 2D Dirac Hamiltonian for the flat surface of a 3D TI . The Hamiltonian (spanned in one of the eigenstates of τ_x) has the form of massless Dirac Fermions (apart from the identity term , from Eq. (2.31)):

$$H'_{\text{surf}} = v_F(\sigma_x k_x + \sigma_y k_y). \tag{2.50}$$

This massless Dirac mode, which lies on the surface, is the signature of a TI , where this mode is protected from any time reversal symmetric small perturbation.

Then we discussed the band structure of cylindrical geometry based on the bulk Hamiltonian (2.4). For a nanowire, the dispersion relation (which defines the bands) has the form (2.42):

$$E_{j,\pm}(k) = \pm\sqrt{(v_1 k)^2 + (j v_2/R)^2}, \tag{2.51}$$

for the band with angular momentum j.

Then, in Sec. 2.5 we have studied the band structure of a quantum dot made of a strong topological insulator from the low-energy theory of Zhang *et al.*[51,63] The main conclusions reached are as follows: First, longitudinal momentum quantization implies a discrete sequence of energy levels which can (roughly) be approximated by letting $k \to k_n = n\pi/L$ ($n \in \mathbb{N}$) in Eq. (2.42). Remarkably, in addition we find unconventional "zero-momentum" states (where, formally, $k_n = 0$). In such a state, the charge and spin densities are almost homogeneous along the z-direction. Furthermore, there are subgap states energetically located within the surface mode gap (Δ_s). These states are localized near both caps and show interesting spin texture.

Second, we observe significant out-of-surface components for the spin density associated with all energy eigenstates. Note that an out-of-plane spin texture is only expected when trigonal warping effects are important,[74,75] see also very recent experimental results reporting such features.[76,77] However, to lowest order in momentum (around the Γ point), trigonal warping can be neglected, while we persistently find broken spin-surface locking also at the lowest energy scales.

We compare the results of this finite nanotube geometry with that obtained from the framework of a surface Dirac Fermion theory in the next chapter and discuss possible experimental setups that can verify the exotic features.

Chapter 3

Surface Dirac Fermion Theory for TI Nanotube

3.1 Introduction

Excitations on the 2D surface of a 3D TI around the time-reversal symmetric Dirac point are best described by Dirac Fermion theory as we have discussed in the first chapter (Sec. 1.2.8) as well as for the case of Bi_2Se_3, in the last chapter (Sec. 2.3). In this chapter, we introduce the surface Dirac Fermion theory for the curved surface of a cylindrical TI starting from the low energy Hamiltonian (2.4) for materials like Bi_2Se_3. Along with the Dirac Fermion theory for a flat surface we discussed in the last chapter (Sec. 2.3.1), we then recalculate various properties of a TI quantum dot of the shape of a cylindrical nanotube and compare them with the numerical results we obtained in Sec. 2.5.1.

3.2 Surface Hamiltonian for TI Nanowire

We start with the parity-extended surface Dirac fermion Hamiltonian for an infinitely long nanowire[65,66] (Eq. (2.43))

$$H_D = \left[v_1 \sigma_\phi (-i\partial_z) - \frac{v_2}{R} \sigma_z \hat{J} \right] \mathcal{T}, \tag{3.1}$$

where the total angular momentum operator $\hat{J}$ has been defined as before as the total angular momentum operator (Eq. (2.37)):

$$\hat{J} = e^{-i\sigma_z \phi/2} \left(-i\partial_\phi\right) e^{i\sigma_z \phi/2} = -i\partial_\phi + \sigma_z/2, \tag{3.2}$$

which commutes with the Hamiltonian. $\mathcal{T} = \mathcal{T}^\dagger$ acts in parity space and is determined below. This extension to the parity space is necessary for dealing with boundary, as we will see later. We note that H_D respects all symmetries present in the bulk-Hamiltonian H_b' (Eq. (2.3)). Specifically,

1. azimuthal symmetry, $[H_D, \hat{J}] = 0$ and states are classified by half-integer j (eigenvalues of $\hat{J}$),

$$\psi(\phi, z) = e^{-i\sigma_z \phi/2} \sum_{j \in \mathbb{Z}+1/2} e^{ij\phi}\, \psi_j(z), \tag{3.3}$$

with the 1D spinor $\psi_j(z)$.

2. Time-reversal symmetry (when $\Phi = 0$), with the symmetry operator $\Theta = i\sigma_y\tau_0 K$, where K is the complex conjugation; and

3. finally, Eq. (3.1) exhibits inversion symmetry, $[H_D, \mathcal{I}] = 0$, with the inversion operator

$$\mathcal{I} = R_z R_\phi \sigma_0 \tau_z. \tag{3.4}$$

Here, R_z inverts the z coordinate, $z \to -z$, and R_ϕ shifts $\phi \to \phi + \pi$. The parity structure in Eq. (3.4) follows from the results of Ref. 51 for a bulk TI . Note that under inversion: $\mathcal{I}\sigma_{\phi,r}\mathcal{I}^{-1} = -\sigma_{\phi,r}$, while $[\sigma_z, \mathcal{I}] = 0$.

Evidently, both time-reversal and inversion symmetry are only kept intact when choosing $\mathcal{T} \in \{\tau_0, \tau_z\}$ in Eq. (3.1)[i]. We here set $\mathcal{T} = \tau_z$, as follows from the analytical derivation of Eq. (3.1) in the section 3.2 as well as from numerical calculations based on the Zhang model for the infinite nanowire case.[66]

Using Eq. (3.3), we can now switch to a 1D representation for a given angular momentum (j) channel. For given energy E, the 1D spinor ψ_j obeys the 1D Dirac equation $H^{(j)}\psi_j = E\psi_j$ with[ii]

$$H^{(j)} = \left(-iv_1\sigma_y\partial_z - \frac{jv_2}{R}\sigma_z\right)\tau_z, \tag{3.5}$$

As expected this Hamiltonian gives rise to the dispersion relation as we discussed earlier (Sec. 2.42):

$$E_{j,\pm}(k) = \pm\sqrt{(v_1 k)^2 + (jv_2/R)^2},$$

We also derive the similar Hamiltonian next from a band-inversion model. Where we will note that the representation of the Dirac matrices $\hat{\gamma}_k$ in Eq. (3.10) in terms of products of spin and parity matrices, (in this case in Eq. (3.5)), is multi-valued and leads to a double counting of all surface states derived from Eq. (3.5). Nevertheless, it is technically convenient to proceed in this representation, since the double counting can be easily circumvented, as we show later in Sec. 3.3.1

TI Nanowire surface from band-inversion:

As we discussed in the first chapter, for a Dirac like system, if the mass term changes sign (band-inversion) between two insulators, then the two insulators are not topologically equivalent, and we expect gapless Dirac mode at the edge. If one of the material has Z_2 invariant $\nu_0 = 1$, then the insulator is a strong TI and there exists an odd number of Dirac modes at the edge. We can employ the principle of band-inversion for obtain the surface mode for the Hamiltonian we introduced in last chapter (Eq. (2.3)). Following the

[i] because time reversal contains τ_0 and inversion contains τ_z operatiors in parity space, so the parity operator $\mathcal{T}$ in the Hamiltonian should commute both with τ_0 and τ_z

[ii] In the 1D representation (3.3), the cylindrical Pauli matrices $\sigma_{r,\phi}$ in eq (2.4) are replaced by $\sigma_{x,y}$

gap-inversion model[73] we start from Zhang's bulk Hamiltonian (2.3) within a linear-in-$\boldsymbol{k}$ approximation:

$$H_b' = M\sigma_0\tau_z + \left[v_1 k_z \sigma_z + v_2 \left(k_x\sigma_x + k_y\sigma_y\right)\right]\tau_x + o(k^2) \ , \tag{3.6}$$

where $v_1 = A_1$, $v_2 = A_2$.

For a cylindrical nanowire (of radius R) along the $\hat{z}$ direction, we use cylindrical coordinates and assume that, following Ref. 73, the gap parameter changes sign at $r = R$, i.e., $M(r) = M_0\ \mathrm{sgn}(R - r)$ with $M_0 > 0$. For $r < R$ ($r > R$), the material is then in the topologically nontrivial (trivial) phase. For simplicity, we choose a symmetric in amplitude jump: $M(r) = \mathcal{M}\ \mathrm{sign}(R - r)$, with $\mathcal{M} > 0$. In the cylindrical geometry the total angular momentum operator $\hat{J}$ (3.2) commutes with the Hamiltonian, and also, for infinite nanowire, the momentum along the axis k_z is conserved and appears as a parameter. In the $\hat{J}$-representation, for given $k_z = k$:

$$\psi(r,\phi,z) = e^{ikz}\, e^{-i\sigma_z\phi/2} \sum_j e^{ij\phi}\, \psi_j(r) \ , \tag{3.7}$$

where $\psi_j(r)$ obeys a 1D Dirac equation in radial direction for given energy ϵ (writing (3.6) in cylindrical coordinates):

$$\left(h_j^{(0)} + v_1 k \sigma_z \tau_x\right)\psi_j = \epsilon\psi_j \ , \tag{3.8}$$

with

$$h_j^{(0)} = M\sigma_0\tau_z + v_2\left[-i\left(\partial_r + \frac{1}{2r}\right)\sigma_x + \frac{j}{r}\,\sigma_y\right]\tau_x \ . \tag{3.9}$$

For considering the surface states (as discussed in Sec. 2.3), first we consider the surface states of the Hamiltonian (3.8) with $k = 0$, *viz*, $h_j^{(0)}$. Then we project the whole Hamiltonian on the subspace spanned by these eigenstates, to obtain an effective surface Hamiltonian for finite k. The details of this calculation is shown in Appendix C.

As a result, one finds for the truncated Hamiltonian:

$$h_j = \frac{j v_2}{R}\,\rho_z + v_1 k\,\rho_y \ , \tag{3.10}$$

where ρ_i are the Pauli matrices in the zero-momentum subspace, which are not single valued, and one can calculate all spin-parity matrices, which results in a representation of the Dirac matrices $\hat{\gamma} = \sigma_\mu\tau_\nu$ in the truncated basis. In the limit $R \to \infty$, one finds: Taking $\rho_y = \sigma_y\tau_z$ and $\rho_z = -\sigma_z\tau_z$ (see the last column of the above Table), one gets an effective surface Hamiltonian with the same spin structure as obtained in Eq. (3.5):[66]

$$H^{(j)} = \left(-\frac{j v_2}{R}\,\sigma_z + v_1 k\,\sigma_y\right)\tau_z \ . \tag{3.11}$$

	τ_0	τ_x	τ_y	τ_z
σ_0	$\hat{\gamma}_0$	0	$\hat{\gamma}_x$	0
σ_x	$-\hat{\gamma}_x$	0	$-\hat{\gamma}_0$	0
σ_y	0	$\hat{\gamma}_z$	0	$\hat{\gamma}_y$
σ_z	0	$\hat{\gamma}_y$	0	$-\hat{\gamma}_z$

Table 3.1: Representation of spin-parity matrices in terms of Pauli matrices $\hat{\gamma}_i$ acting in surface-state subspace.

3.2.1 Spin and parity densities

The plane wave solution to the 1D Dirac equation with Hamiltonian $H^{(j)}$ in Eq. (3.5) reads

$$\psi_j(z) = \begin{pmatrix} A_1\chi_j \\ -iA_2\sigma_x\chi_j \end{pmatrix} e^{ikz} + \begin{pmatrix} B_1\chi_j^* \\ iB_2\sigma_x\chi_j^* \end{pmatrix} e^{-ikz}, \tag{3.12}$$

with arbitrary complex coefficients (A_1, A_2, B_1, B_2). The spinors above are in parity space while χ_j acts in spin space,

$$\chi_j = \begin{pmatrix} \cos\gamma_j \\ i\sin\gamma_j \end{pmatrix} \equiv \begin{pmatrix} \sqrt{\frac{1}{2} - \frac{jv_2}{2RE}} \\ i\ \mathrm{sgn}(E)\sqrt{\frac{1}{2} + \frac{jv_2}{2RE}} \end{pmatrix}. \tag{3.13}$$

and the longitudinal momentum $k = k(E)$ follows from the energy

$$E^2 = (v_1 k)^2 + (jv_2/R)^2. \tag{3.14}$$

Below we consider energies where k is real and positive. For a description of the subgap states, in case discussed in Sec. 3.3, evanescent modes need to be studied instead.

In the 1D representation, the inversion operator [Eq. (3.4)] becomes $\mathcal{I} \to \tilde{\mathcal{I}}$ with

$$\tilde{\mathcal{I}} = R_z\sigma_z\tau_z. \tag{3.15}$$

Since Eq. (3.5) stays invariant under inversion, $[H^{(j)}, \tilde{\mathcal{I}}] = 0$, the eigenfunctions (3.12) can be classified as inversion symmetric or antisymmetric ($\sigma = \pm$),

$$\tilde{\mathcal{I}}\psi_j^{(\sigma)}(z) = \sigma\psi_j^{(\sigma)}(z). \tag{3.16}$$

From Eqs. (3.12) and (3.16), after a short calculation, we can therefore infer relations between the coefficients for given inversion symmetry (σ):

$$A_1 = \sigma B_1, \quad A_2 = -\sigma B_2.$$

A general inversion-symmetric (antisymmetric) state thus takes the form

$$\begin{aligned} \psi_j^{(+)} &= \begin{pmatrix} A_1 \\ -iA_2\sigma_x \end{pmatrix} \otimes \begin{pmatrix} \cos\gamma_j\ \cos(kz) \\ -\sin\gamma_j\ \sin(kz) \end{pmatrix}, \\ \psi_j^{(-)} &= \begin{pmatrix} iA_1 \\ A_2\sigma_x \end{pmatrix} \otimes \begin{pmatrix} \cos\gamma_j\ \sin(kz) \\ \sin\gamma_j\ \cos(kz) \end{pmatrix}. \end{aligned} \tag{3.17}$$

Both are parametrized by two complex numbers (A_1 and A_2), where the first (second) spinor refers to parity (spin) space.

We can take local expectation value for the charge, spin, and parity operators in a given general eigenstate $\psi_j^{(\sigma)}$. With $\sin^2(\gamma_{-j}) = \cos^2(\gamma_j)$, the charge density is

$$\langle\rho\rangle(z) = \left(|A_1|^2 + |A_2|^2\right)\left[\cos^2(\gamma_{\sigma j})\cos^2(kz) + \sin^2(\gamma_{\sigma j})\sin^2(kz)\right]. \tag{3.18}$$

For the spin density, we obtain

$$\begin{aligned}
\langle\sigma_r\rangle &= -\frac{\sigma}{2}\left(|A_1|^2 + |A_2|^2\right)\sin(2\gamma_j)\sin(2kz)\\
\langle\sigma_\phi\rangle &= 0\\
\langle\sigma_z\rangle &= \sigma\left(|A_1|^2 - |A_2|^2\right)\left[\cos^2(\gamma_{\sigma j})\cos^2(kz) - \sin^2(\gamma_{\sigma j})\sin^2(kz)\right].
\end{aligned}$$

Similarly, the parity density is obtained in the form

$$\begin{aligned}
\langle\tau_x\rangle &= \sigma\,\mathrm{Im}(A_1A_2^*)\sin(2\gamma_j)\sin(2kz)\\
\langle\tau_y\rangle &= \sigma\,\mathrm{Re}(A_1A_2^*)\sin(2\gamma_j)\sin(2kz)\\
\langle\tau_z\rangle &= \left(|A_1|^2 - |A_2|^2\right)\left[\cos^2(\gamma_{\sigma j})\cos^2(kz) + \sin^2(\gamma_{\sigma j})\sin^2(kz)\right].
\end{aligned}$$

At this stage, the above results hold for an *arbitrary* inversion-symmetric ($\sigma = +$) or antisymmetric ($\sigma = -$) state.

Remarkably, for this parity extended Hamiltonian Eq. (3.5), the circumferentially oriented spin density $\langle\sigma_\phi\rangle$ always vanishes. This is in accordance with our numerical observations (Eq. (2.48)). The current density along the z direction can be obtained from the local operator[66]

$$j_z = v_1\sigma_\phi\tau_z, \tag{3.19}$$

and therefore vanishes identically for these states as well[iii]. This result stays valid for arbitrary inversion-symmetric boundary conditions (which do not mix $\psi_j^{(\pm)}$ states).

In order to reach agreement with the numerical results in Sec. 2.5.1, the coefficients $A_{1,2}$ should obey the three relations

$$\mathrm{Im}(A_1A_2^*) = 0, \quad \mathrm{Re}(A_1A_2^*) > 0, \quad |A_1| \neq |A_2|. \tag{3.20}$$

Indeed, the first relation implies consistency with Eq. (2.48). The second relation ensures that $\langle\tau_y\rangle(z) \propto -\langle\sigma_r\rangle(z)$, see Eq. (2.49). The third relation is required to have non-vanishing spin-parity densities $\langle\sigma_z\rangle$ and $\langle\tau_z\rangle(z)$. Moreover, notice that then $\langle\tau_z\rangle(z) \propto \langle\rho\rangle(z)$, in accordance with Eq. (2.49).

3.3 Finite Nanowire: Matching Trunk and Cap States

For a finite nanowire, the coefficients $A_{1,2}$ in Eq. (3.17) as well as the energy spectrum and the corresponding eigenstates can now be obtained analytically by matching the trunk states, see Eq. (3.17) for $|z| < L/2$, with cap states at $z = \pm L/2$.

[iii] For current-carrying states, one has to impose boundary conditions breaking the inversion symmetry.

Each cap (plane surface of a 3D TI) is described by a surface Dirac Hamiltonian of the form

$$H_{\rm cap} = v_2 \left[-i \left(\partial_r + \frac{1}{2r} \right) \sigma_r + \frac{\hat{J}}{r} \sigma_\phi \right] \tau_x. \tag{3.21}$$

The parity matrix τ_x is uniquely determined by imposing time-reversal and inversion symmetry, and also appears in Eq. (2.3) [in cartesian coordinates, $H_{\rm cap} = v_2 \left(k_x \sigma_x + k_y \sigma_y \right) \tau_x$].

In the angular momentum (1D) representation, for given j and energy E, the cap states $\Psi^{(\sigma)}_{j,\epsilon}(r, z = \pm L/2)$ with parity $\sigma = \pm$, that is, obeying $\tilde{\mathcal{I}} \Psi^{(\sigma)}_{j,\epsilon} = \sigma \Psi^{(\sigma)}_{j,\epsilon}$, are given by ($r < R$):

$$\Psi^{(\sigma)}_{j,\epsilon}(r,z) = \begin{cases} C\, \xi_j(r) \otimes \begin{pmatrix} 1 \\ 1 \end{pmatrix} + D\, \xi^*_j(r) \otimes \begin{pmatrix} 1 \\ -1 \end{pmatrix}, & z = L/2 \\ \\ \sigma \left[D\, \xi_j(r) \otimes \begin{pmatrix} 1 \\ 1 \end{pmatrix} + C\, \xi^*_j(r) \otimes \begin{pmatrix} 1 \\ -1 \end{pmatrix} \right], & z = -L/2 \end{cases}, \tag{3.22}$$

with complex coefficients C, D and the spinor (in spin space) $\xi_j(r)$ is a solution of the Dirac equation in radial direction:

$$\xi_j(r) = \begin{pmatrix} J_{j-1/2}(\omega r) \\ \\ i\, \mathrm{sign}(\epsilon) J_{j+1/2}(\omega r) \end{pmatrix}, \quad \omega = |E|/v_2 \,, \tag{3.23}$$

with J_ν the Bessel function. The other spinors in (3.22) are in parity space.

Matching the trunk states [Eq. (3.17)] and the cap states [Eq. (3.22)] for given j by continuity at $(z, r) = (\pm L/2, R)$, we obtain:

$$\frac{1}{2} \begin{pmatrix} A_1 \left[\chi_j e^{ikL/2} + \sigma \chi^*_j e^{-ikL/2} \right] \\ \\ A_2 \left[\tilde{\chi}_j e^{ikL/2} - \sigma \tilde{\chi}^*_j e^{-ikL/2} \right] \end{pmatrix} = \begin{pmatrix} C\, \xi_j(R) + D\, \xi^*_j(R) \\ \\ C\, \xi_j(R) - D\, \xi^*_j(R) \end{pmatrix}, \tag{3.24}$$

which are four linear equations for the four coefficients (A_1, A_2, C, D). A nontrivial solution follows when the corresponding determinant vanishes, yielding the condition results in the following dispersion equation (for $\sigma = \pm$):

$$\left[J^2_{j-1/2}(\omega R) + J^2_{j+1/2}(\omega R) \right] \sin\left(2\gamma_j\right) \sin(kL) = 0 \,. \tag{3.25}$$

For real-valued $k \geq 0$, this equation can only be satisfied when $\sin(kL) = 0$. This implies the standard longitudinal momentum quantization condition $k_n(E) = n\pi/L$ with $n \in \mathbb{N}_0$. The corresponding eigenenergies then follow from the bulk dispersion relation in Eq. (2.42),

$$E_{j,n,\pm} = \pm \sqrt{(\pi n v_1/L)^2 + (j v_2/R)^2}. \tag{3.26}$$

For a given level, the wave function amplitudes $A_{1,2}$ and C, D then satisfy three conditions plus the overall normalization constraint. With $p = \sigma(-)^n = \pm$ and the above definition of ω, we have $C = pD$ and the relation

$$J_{j+p/2}(\omega R)A_1 + p\ \mathrm{sgn}(E)\ J_{j-p/2}(\omega R)A_2 = 0. \tag{3.27}$$

Moreover, for $p = +$ the third condition reads

$$\cos(\gamma_j)A_1 - 2(-i)^n J_{j-1/2}(u)C = 0, \tag{3.28}$$

while for $p = -$ this instead becomes

$$\sin(\gamma_j)A_1 - 2(-i)^n\ \mathrm{sgn}(E)\ J_{j+1/2}(u)C = 0.$$

These relations determine all possible wavefunctions for the closed cylinder surface.

Of course, since we considered only solutions of Eq. (3.25) with real k, subgap states were not captured. However, within the linear-in-$\boldsymbol{k}$ approximation underlying the approach here, we find that there are no subgap states at all, i.e., the corresponding matching problem with evanescent trunk modes does not permit a nontrivial solution. The numerical approach of Sec. 2.5.1 also indicates that in order to obtain subgap states, it is necessary to include higher-order terms (in $\boldsymbol{k}$) breaking electron-hole symmetry in the Hamiltonian.

3.3.1 Spectrum & eigenstates of the dot

Using the above explicit solution for the wavefunction of the complete cylinder, we obtain the coordinate dependence of all densities of interest. We here describe the results for the trunk region (the curved surface of the cylinder) only. First of all, we recover from Eq. (3.19) and (3.19),

$$\langle\sigma_\phi\rangle = \langle\tau_x\rangle = 0,$$

which is the same as we obtained numerically (Eq. (2.48)). Moreover, the relations

$$\langle\tau_y\rangle \propto -\langle\sigma_r\rangle, \quad \langle\tau_z\rangle \propto \langle\rho\rangle$$

are also reproduced, see Eq. (2.49). Specifically, the dot eigenstates have the energy $E \equiv E_{j,n,\pm}$ specified in Eq. (3.26). We show below that these energies are not degenerate, i.e., only one specific inversion parity σ given by

$$\sigma \equiv \sigma_{j,n,\pm} = \mp(-1)^n \mathrm{sgn}(j) \tag{3.29}$$

will be physically realized. With $k \equiv \pi n/L \geq 0$, we find for the charge and spin densities ($u = |E|R/v_2$)

$$\begin{aligned}
\langle\rho\rangle(z) &\propto 1 - \mathrm{sgn}(E)\frac{j\sigma}{u}\cos(2kz), \\
\langle\sigma_r\rangle(z) &\propto \sqrt{1 - j^2/u^2}\ \sin(2kz), \\
\langle\sigma_z\rangle(z) &\propto \cos(2kz) - \frac{j\sigma}{u}\mathrm{sgn}(E).
\end{aligned} \tag{3.30}$$

These results are in good agreement with the numerical results for the spin texture obtained for the Zhang model in Sec. 2.5.1. In particular, they show explicitly that spin-surface locking is broken.

Interestingly, for each total angular momentum j, there are two zero-momentum states corresponding to conduction and valence band, respectively. Their inversion symmetry properties are determined by

$$\sigma = -\mathrm{sgn}(jE_{j,n=0,\pm}), \tag{3.31}$$

since for states with the opposite value of σ, all densities in Eq. (3.30) vanish. For the physically allowed $k = 0$ state with σ in Eq. (3.31), from Eq. (3.30) we instead find spatially *uniform* densities $\langle\rho\rangle(z)$, $\langle\tau_z\rangle(z)$, and $\langle\sigma_z\rangle(z)$, while all remaining spin or parity density components vanish.

We now compare the densities in Eq. (3.30) to the numerical results in Sec. 2.5.1, and also address the double counting problem mentioned in Sec. 3.2. Eq. (3.27) shows that indeed $\mathrm{Im}(A_1A_2^*) = 0$, in accordance with our numerical results in Sec. 2.5.1, see Eq. (3.20). Also the relation $|A_1| \neq |A_2|$ in Eq. (3.20) is evidently satisfied. However, not all the states can be realized physically, as is clear by comparing to the condition $\mathrm{Re}(A_1A_2^*) > 0$ in Eq. (3.20) found numerically in Sec. 2.5.1. In order to understand this restriction, we note that the operator $\Xi = \sigma_z\tau_z$ commutes both with the cap Hamiltonian [Eq. (3.21)] and with the inversion operator $\tilde{\mathcal{I}}$ [Eq. (3.15)]. This implies by continuity that trunk states [Eq. (3.17)] at the end points ($z = \zeta L/2$ with $\zeta = \pm$) are eigenstates of Ξ as well,

$$\Xi\psi_{j,n}^{(\sigma)}(\zeta L/2) = p\psi_{j,n}^{(\sigma)}(\zeta L/2),$$

where the eigenvalues $p = \sigma(-1)^n$ follow from Eq. (3.17) and the definition of Ξ. For $n = 0$, however, Eq. (3.31) implies that only the eigenvalue $p = -\mathrm{sgn}(jE_{j,0,\pm})$ is physically realized. By continuity, this value must also apply for the full Hilbert space of conduction or valence surface bands. We therefore obtain the "selection rule" in Eq. (3.29) restricting the Hilbert space of allowed states. This explains the condition $\mathrm{Re}(A_1A_2^*) > 0$ and resolves the double-counting problem. We mention in passing that the latter problem is automatically avoided when retaining terms of order $\boldsymbol{k}^2$ in the Hamiltonian, where the spin-parity eigenstates with $p = \pm$ have different energy. In the Dirac theory, this implies a "spontaneously broken symmetry" encoded by Eq. (3.29).

3.3.2 Effective boundary condition

It is also possible to derive the results in Sec. 3.3.1 without explicit construction of the cap states. To that end, let us briefly consider a class of general boundary conditions at the cylinder ends, $z = \zeta L/2$ with $\zeta = \pm$, by imposing the local gauge constraints

$$\psi(\phi, \zeta L/2) = \Lambda_\zeta\, \psi(\phi, \zeta L/2), \tag{3.32}$$

where $\Lambda_\zeta = \Lambda_\zeta^{-1} = \Lambda_\zeta^\dagger$. The spin-parity structure of Λ_ζ can be determined by requiring time-reversal invariance, $[\Lambda_\zeta, \Theta] = 0$, and invariance under inversion, $[\Lambda_\zeta, \mathcal{I}] = 0$. In

addition, we require the boundary operator to commute with H_D, which is a natural assumption for closed surfaces. As a result, with arbitrary angles $\eta_\pm$, we find

$$\Lambda_\zeta = \sin(\eta_\zeta)\sigma_0\tau_z + \cos(\eta_\zeta)\sigma_r\tau_y.$$

Passing to the 1D representation, i.e., for given half-integer j, these constraints read

$$\begin{aligned} \psi_j(\zeta L/2) &= \tilde{\Lambda}_\zeta \psi_j(\zeta L/2), \\ \tilde{\Lambda}_\zeta &= \sin(\eta_\zeta)\sigma_0\tau_z + \cos(\eta_\zeta)\sigma_x\tau_y. \end{aligned} \tag{3.33}$$

Applying the inversion operator $\tilde{\mathcal{I}}$, see Eq. (3.15), to the boundary condition (3.33), we find $\tilde{\Lambda}_+ = \tilde{\Lambda}_-$ and hence $\eta_\pm \equiv \eta$. Only then will inversion symmetry be preserved for the confined states. The parameter η (with $0 \leq \eta < \pi$) cannot be fixed by symmetry considerations alone but depends on the physical boundary condition imposed at the ends, i.e., the boundary matrix $\tilde{\Lambda}$ effectively encodes the matching of trunk states with cap states. Contrary to the commonly employed boundary conditions,[78,79] the operator $\tilde{\Lambda}$ *commutes* with the current operator j_z, see Eq. (3.19), while the anticommutator is always nonzero. Since the boundary conditions are invariant with respect to inversion, they do not mix the states (3.17) with opposite inversion parity σ. Using the boundary condition (3.33), some algebra yields for both solutions and for arbitrary energy E the condition

$$A_1 + \frac{\cos\eta}{1-\sin\eta} A_2 = 0. \tag{3.34}$$

Comparing this to Eq. (3.27), the energy-dependent angle η can be explicitly related to the above wavefunction matching procedure, and the subsequent results in Sec. 3.3.1 can be obtained under a purely 1D description of the trunk states alone.

3.4 Summary & Discussion

We have studied the band structure of a quantum dot made of a strong topological insulator using three different approaches, namely the low-energy theory of Zhang *et al.* in the last chapter (Sec. 2.5), numerical calculations for a tight-binding model on a diamond lattice with strong spin-orbit couplings (Appendix B) and finally we have developed an effective surface Dirac fermion theory in this chapter. The considered geometry, with flat caps terminating a finite-length cylindrical nanowire, is characterized by sharp edges where the cylinder trunk and caps meet. Such edges are also present in typical "mesoscopic" TI devices studied experimentally.[56–59] All three approaches show that spin-surface locking is generally violated due to presence of these edges. As also found in a recent *ab initio* study,[80] a finite reflection probability for Dirac fermions in each part results when two surfaces are patched together. In our case, we have a Fabry-Perot-like setup where standing waves can build up. The resulting spin density then exhibits spatial oscillations reminiscent of a spin density wave state. The spin direction of the oscillatory parts points out of the surface while non-oscillatory spin density contributions stay locked to the surface.

The spectrum of such a quantum dot shows several surprising features including emergence of sub-gap states and broken spin-surface locking. The obtained spectrum

and corresponding spin textures are important ingredients for a theory of mesoscopic transport through TI dots. In general, we also expect Coulomb interactions to be relevant, in particular charging effects should be visible. We plan to address these questions in the future. Moreover, extensions of the theory to include an applied magnetic field, where the typically large and anisotropic Landé factor[63] implies that the Zeeman field is crucial, are also left for future work.

Chapter 4

Electron-phonon Scattering in TI Thin Films

4.1 Introduction

Although an insulator in bulk, the surface modes of a 3D Toplogical Insulator (TI) are conducting because of the presence of gapless Dirac like spectrum as discussed in Chapter 1. But, as mentioned in the Chapter 2, transport experiments for the surface modes are difficult since the surface contribution is often masked by the residual conductivity due to impurities or defects in the bulk. So, it is useful to study a sample of TI where the surface to bulk ratio is advantageous. We discussed also the electronic surface states in two such possible geometries, viz, cylindrical geometries and thin film geometry. In this chapter we study the resistivity in a thin film TI . Such geometries are studied theoretically[81,82] and experimentally[83] in graphene before.

The two main sources of resistivity in an electronic system are due to the effect of backscattering by disorders and because of electron-phonon coupling. Our working assumption below is that electron-phonon scattering is the dominant source of quasi-particle decay and backscattering. Electron-electron interactions are indeed expected to give only sub-leading corrections to the resistivity as long as $T \gtrsim 1$ mK.[84] Disorder effects are more likely to compete with phonon-induced backscattering effects. However, for elevated temperatures, $T \gtrsim 100$ K, phonon effects dominate even for present-day samples, and anticipating higher purity films in the future, this crossover temperature may be lowered significantly.

In this chapter, we provide a detailed theoretical analysis of both the temperature-dependent resistivity $\rho(T)$ and the quasi-particle lifetime $\Gamma(T)$ (observable in ARPES[85,86]) for a thin TI film. The case of electron-phonon coupling in TI in a semi-infinite geometry is carried out in Ref. 87. We, in this chapter often compare the results between the two geometry. We also discuss below that there are substantial difference in behaviors and the limit from thin film to a semi-infinite case is singular.

4.2 Electronic Surface States of TI Film

We have already addressed the electronic structure and an effective Hamiltonian describing the surface modes of a TI thin film in Sec. 2.3. Starting from the bulk Hamiltonian (2.4)

$$\begin{aligned} H_b &= \epsilon_0(\boldsymbol{k})I_{4\times4} + \begin{pmatrix} M(\boldsymbol{k}) & -iA_1k_z & 0 & A_2k_- \\ iA_1k_z & -M(\boldsymbol{k}) & A_2k_- & 0 \\ 0 & A_2k_+ & M(\boldsymbol{k}) & -iA_1k_z \\ A_2k_+ & 0 & iA_1k_z & -M(\boldsymbol{k}) \end{pmatrix} \\ &= \epsilon_0(\boldsymbol{k})\sigma_0\tau_0 + M(\boldsymbol{k})\sigma_0\tau_z + A_1\sigma_0\tau_y + A_2\tau_x(k_x\sigma_x + k_y\sigma_y), \end{aligned} \tag{4.1}$$

the effective surface Hamiltonian (for the film surface as the xy plane and a width L) is found to be:

$$H_{\text{eff}} = E_0\, I_{4\times4} + \frac{\Delta}{2}\,\tau_z\sigma_0 - A_2W\,\tau_x(k_x\sigma_x + k_y\sigma_y). \tag{4.2}$$

where, Pauli matrices $\boldsymbol{\sigma}$ act in the spin space and $\boldsymbol{\tau}$ switches between the two zero momentum solutions $\Psi_{\tau=\pm}(z)$ (Eq. (2.19)) which defines the parity basis. Also the parameters are discussed before and is given in Table 2.1. With $E_0^{(\pm)}$ as the two Γ point (zero momentum) energies, E_0 and Δ are given by:

$$E_0 = \frac{E_0^{(+)} + E_0^{(-)}}{2}, \quad \Delta = E_0^{(+)} - E_0^{(-)}. \tag{4.3}$$

Δ depends on the width L and goes to zero exponentially with the width for the parameters we use (shown in Fig. 2.4 and in inset of Fig. 4.1). The parameter W is discussed in Sec. 2.3 and is always real.

Noting that H_{eff} commutes with $\tau_z\sigma_z$, it can readily be diagonalized by the unitary transformation $U(\mathbf{k}) = \text{diag}(U_+, U_-)$, where $\mathbf{k} = (k_x, k_y)$ and the $U_{\upsilon=\pm}(\mathbf{k})$ are 2×2 matrices in spin space, with υ denoting the eigenvalue of $\tau_z\sigma_z$. With $\tan\alpha = 2A_2W|\mathbf{k}|/\Delta$ and $\tan\theta = k_y/k_x$, we find

$$\begin{aligned} U_{\upsilon=+} &= \begin{pmatrix} e^{-i\theta/2}\cos(\alpha/2) & e^{-i\theta/2}\sin(\alpha/2) \\ -e^{i\theta/2}\sin(\alpha/2) & e^{i\theta/2}\cos(\alpha/2) \end{pmatrix}, \\ U_{\upsilon=-} &= \begin{pmatrix} -e^{-i\theta/2}\sin(\alpha/2) & e^{-i\theta/2}\cos(\alpha/2) \\ e^{i\theta/2}\cos(\alpha/2) & e^{i\theta/2}\sin(\alpha/2) \end{pmatrix}. \end{aligned} \tag{4.4}$$

Switching to second-quantized notation, the eigenstates of H_{eff} correspond to helical fermions with annihilation operator

$$c_{\mathbf{k},\upsilon s} = \sum_\sigma [U_\upsilon(\mathbf{k})]^*_{\sigma s}\; d_{\mathbf{k},\tau=\upsilon\sigma,\sigma}, \tag{4.5}$$

where $d_{\mathbf{k},\tau\sigma}$ annihilates a spin-σ electron with in-plane momentum $\mathbf{k}$ in the transversal state $\Psi_\tau(z)$. The low-energy electronic Hamiltonian (including the chemical potential μ) then takes the final form

$$H_{\text{el}} = \sum_{\mathbf{k};\upsilon,s=\pm} \epsilon_{\mathbf{k},s}c^\dagger_{\mathbf{k},\upsilon s}c_{\mathbf{k},\upsilon s}, \tag{4.6}$$

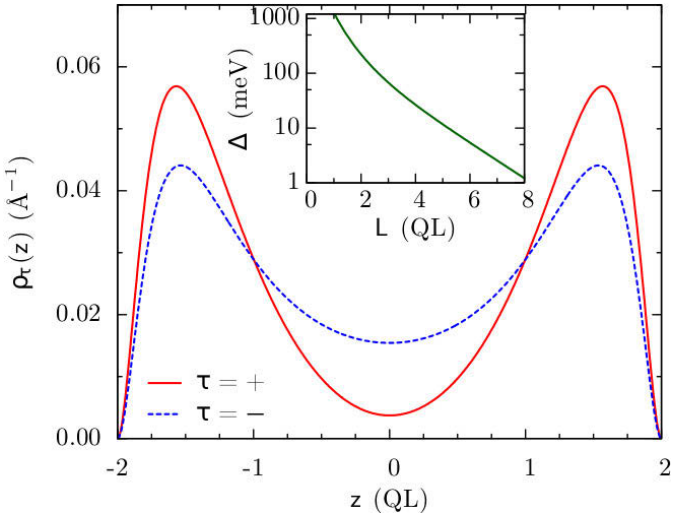

Figure 4.1: Electronic eigenstates for Bi_2Se_3 from Eqs. (4.1) and Table 2.1. Main panel: Densities $\rho_\tau(z)$ in Eq. (4.9) for $L = 4$ QL. Inset: Gap Δ vs thickness L. Note the semi-logarithmic scale.

where the dispersion relation is

$$\epsilon_{\mathbf{k},\pm} = E_0 - E_0^\infty - \mu \pm \frac{\Delta}{2}\sqrt{1 + (2A_2W/\Delta)^2\mathbf{k}^2}. \tag{4.7}$$

We here choose the zero of energy by setting $E_0^\infty = C + D_1M_0/B_1 = \lim_{L\to\infty} E_0^{(\pm)}$. For the parameters of Ref. 63 (noted in Table 2.1), we find $E_0^\infty \simeq 0.22$ eV. Moreover, for $L \to \infty$, the length scales $\eta_\pm^{-1}$ are given by $\eta_+^{-1} \simeq 12.3$ Å and $\eta_-^{-1} \simeq 1.9$ Å. For $kL \gg 1$, the dispersion relation (4.7) is linear, with Fermi velocity $v_F \simeq 2.77 \times 10^5$ m/s. Note that the index $s = \pm$ in Eq. (4.6) does not correspond to spin anymore.

Similarly, the particle density operator $\hat{n}(\mathbf{r}, z)$ with $\mathbf{r} = (x, y)$ is written in terms of the $d_{\mathbf{k},\tau\sigma}$ operators,

$$\hat{n}(\mathbf{r}, z) = \sum_{\mathbf{k},\mathbf{q},\tau,\sigma} e^{-i\mathbf{q}\cdot\mathbf{r}}\rho_\tau(z)d^\dagger_{\mathbf{k}+\mathbf{q},\tau\sigma}d_{\mathbf{k},\tau\sigma}. \tag{4.8}$$

Using Eq. (4.5), the density operator (4.8) can be transformed to the helical basis. We show the single-particle densities for the surface states [Eq. (2.19)],

$$\rho_\tau(z) = \left[\Psi_\tau^\dagger \cdot \Psi_\tau\right](z), \tag{4.9}$$

in Fig. 4.1 for a film thickness of $L = 4$ QL, where 1 QL $\simeq 9.5$Å for Bi_2Se_3.[88] This demonstrates that already for quite thin films, Eq. (2.19) describes surface states. Note that $\rho_\tau(z)$ is an even function of z. The inset of Fig. 4.1 shows the numerically obtained gap $\Delta(L)$, demonstrating the absence of oscillatory behavior for the parameters in Table

2.1 as well as the exponential decay of $\Delta(L)$ due to the exponentially vanishing overlap of both surface states. We note in passing that the parameters in Ref. 51 instead predicts from (4.3) an oscillatory decay of $\Delta(L)$.

4.3 Acoustic Phonons in Film Geometry

Since even at room temperature, one effectively probes low energy scales, we keep only long-wavelength acoustic phonon modes. For these, previous work on related materials has shown[89,90] that isotropic elastic continuum theory provides a reasonable approximation. The phonon eigenmodes in the thin film geometry and their coupling to electronic modes have previously been determined in the context of semiconductor quantum well structures[91] (Note that the semi-infinite case has been treated in Ref. 92). But the coupling to the helical electronic eigenstates in a TI film is different from the semiconductor case. Note that piezoelectric couplings are suppressed by symmetry here,[90] and spin-phonon type couplings[93] are also expected to be sub-dominant to the deformation potential we have taken into account.

Small elastic vibrations in the elastic continuum theory are described by the displacement vector $\mathbf{u}(\boldsymbol{r}, t)$. The Lagrangian of the vibrations in an isotropic system can be expressed as (ρ_M is the mass density):

$$L = \frac{1}{2}\int \left(\rho_M (\partial_t \mathbf{u})^2 - \sum_i \lambda u_{ij}^2 - \sum_{i,k} 2\mu u_{ik}^2 \right) d\boldsymbol{r}, \tag{4.10}$$

where, u_{ij} is the linearized strain tensor

$$u_{ij} = \frac{1}{2}\left(\frac{\partial u_i}{\partial r_j} + \frac{\partial u_j}{\partial r_i} \right). \tag{4.11}$$

The phonon modes are found from the solution of the elastic wave equation (from the above Lagrangian)

$$\frac{\partial^2 \mathbf{u}}{\partial t^2} = c_t^2 \nabla^2 \mathbf{u} + \left(c_l^2 - c_t^2\right) \text{grad div } \mathbf{u} \ , \tag{4.12}$$

with the stress-free boundary condition imposed on the stress tensor ($\sigma_{ij} = \lambda \text{ div } \mathbf{u}\, \delta_{ij} + 2\mu\, u_{ij}$) at $z = \pm L/2$:

$$\sigma_{xz} = \sigma_{yz} = \sigma_{zz} = 0. \tag{4.13}$$

Here $c_t = \mu/\rho_M$ and $c_l = (\lambda + 2\mu)/\rho_M$ are velocities transverse and longitudinal acoustic waves. The Lame parameters λ and μ are related to the Young modulus (Y) and the bulk modulus (K), and for Bi_2Se_3 are found to be in GPa:[94,95]

$$K = \lambda + \frac{2}{3}\mu \approx 38 \pm 3, \quad Y = \frac{9K\mu}{3K + \mu} \approx 57 \pm 2. \tag{4.14}$$

Then the two velocities are found to be $c_t \approx 1700$ m/s, $c_l \approx 2900$ m/s. Also, the density of Bi_2Se_3 is $\rho_M = 7680$ kg/m^3.[96]

In a confined film type geometry, the resulting solutions of the wave equation can be categorized into different modes. Following the notation in Ref.,[91] we label the modes by the quantum numbers $\Lambda = (\mathbf{q}, n, \lambda)$, with surface momentum $\mathbf{q} = (q_x, q_y)$, branch index n, and mode type $\lambda \in (H, S, A)$ explained below. With $\mathbf{r} = (x, y)$ and surface area $\mathcal{A}$, the displacement field operator takes the form

$$\mathbf{U}(\mathbf{r}, z, t) = \sum_{\Lambda} \frac{1}{\sqrt{2\rho_M \mathcal{A}\Omega_\Lambda}} \mathbf{u}_\Lambda(z) e^{i(\mathbf{q}\cdot\mathbf{r} - \Omega_\Lambda t)} b_\Lambda + \text{h.c.}, \tag{4.15}$$

where b_Λ is a bosonic annihilation operator. The noninteracting phonon Hamiltonian is

$$H_p = \sum_{\Lambda} \Omega_\Lambda (b_\Lambda^\dagger b_\Lambda + 1/2). \tag{4.16}$$

The orthonormal eigenmodes $\mathbf{u}_\Lambda(z)$ describe linear combinations of $e^{\pm i k_{l,t} z}$ waves, where Ω_Λ is the dispersion relation of a given phonon mode Λ (discussed later), and

$$k_{l,t} = \sqrt{(\Omega_\Lambda / c_{l,t})^2 - q^2}, \tag{4.17}$$

with $k_{l,t} = i\kappa_{l,t} \equiv i\sqrt{q^2 - (\Omega_\Lambda/c_{l,t})^2}$ when $\Omega_\Lambda < c_{l,t} q$. First, the horizontal shear mode, $\lambda = H$, with $\mathbf{u}_H \parallel \hat{e}_z \times \hat{e}_q$ (where $\hat{e}_q = \mathbf{q}/q$) decouples from all other modes and does not generate a deformation potential; hence it is not discussed further. The remaining modes are given by

$$\mathbf{u}(z) = \left(iq\phi_l - \frac{d\phi_t}{dz} \right) \hat{e}_q + \left(\frac{d\phi_l}{dz} + iq\phi_t \right) \hat{e}_z \tag{4.18}$$

where, $e_q = \mathbf{q}/q$ and

$$\phi_{l,t} = a_{l,t} \cos(k_{l,t} z) + b_{l,t} \sin(k_{l,t} z) \tag{4.19}$$

and the stress-free boundary conditions at $z = \pm L/2$ yield

$$\begin{aligned} 2iq \frac{d\phi_l}{dz} - (q^2 - k_t^2)\phi_t &= 0, \\ 2iq \frac{d\phi_t}{dz} + (q^2 - k_t^2)\phi_l &= 0. \end{aligned} \tag{4.20}$$

Since both equations have to be fulfilled at $z = \pm L/2$, we have four linear equations for the four unknown parameters $(a_{l,t}, b_{l,t})$. Setting the corresponding determinant to zero, we obtain the following two possibilities. First, for symmetric modes ($\lambda = S$), we have the condition

$$(q^2 - k_t^2)^2 \cos(k_l L/2) \sin(k_t L/2) + 4q^2 k_l k_t \sin(k_l L/2) \cos(k_t L/2) = 0. \tag{4.21}$$

Numerical solution of this transcendental equation obtains the quantized set of dilatational phonon frequencies $\Omega_{\Lambda=(\mathbf{q},S,n)}$. The corresponding eigenvector, $\mathbf{u}_\Lambda(z)$, follows from Eqs. (4.18) and (4.19) with $a_t = b_l = 0$ and

$$a_l = \frac{2\mathcal{N}_S q}{\cos(k_l L/2)}, \quad b_t = \frac{i\mathcal{N}_S (q^2 - k_t^2)}{k_t \cos(k_t L/2)}. \tag{4.22}$$

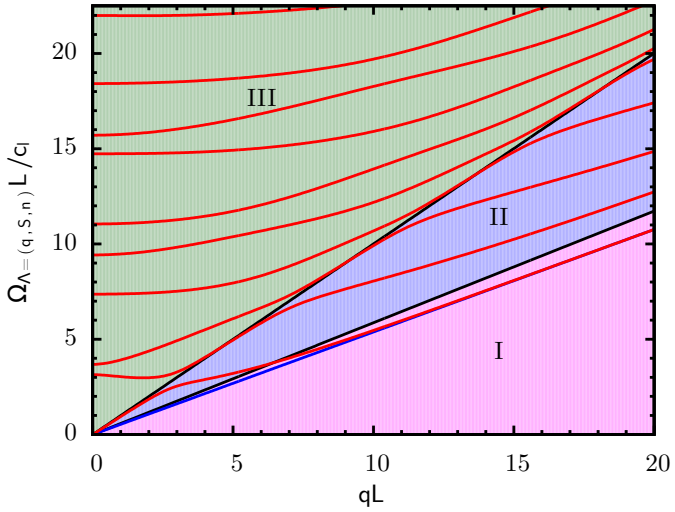

Figure 4.2: Phonon dispersion relation, Ω_Λ vs q, for the symmetric ($\lambda = S$) mode (red solid curves). Shown are the ten lowest branches corresponding to the index n. Dashed lines separate regions I, II, and III (see main text). The dash-dotted line gives the dispersion relation in Eq. (4.24); note that the $n = 1$ mode coincides with the Rayleigh mode for $qL \gg 1$.

Second, for antisymmetric modes ($\lambda = A$), we arrive again at the condition in Eq. (4.21) but with the exchange cos $\leftrightarrow$ sin. Solving that equation yields the set $\Omega_{\Lambda=(\mathbf{q},A,n)}$ of quantized flexural phonon modes. The eigenvector $\mathbf{u}_\Lambda(z)$ follows again from Eqs. (4.18) and (4.19), where now $a_l = b_t = 0$ and

$$b_l = \frac{2\mathcal{N}_A q}{\sin(k_l L/2)}, \quad a_t = \frac{-i\mathcal{N}_A(q^2 - k_t^2)}{k_t \sin(k_t L/2)}. \tag{4.23}$$

The normalization factors $\mathcal{N}_{\lambda=S,A}$ appearing in Eqs. (4.22) and (4.23) are given by:

$$\begin{aligned}\mathcal{N}_S^{-2} &= \frac{\Omega_\Lambda^2}{2c_t^2}\left[\frac{c_t^2}{c_l^2}\frac{4q^2L}{\cos^2(k_lL/2)}\left(1+\frac{\sin(k_lL)}{k_lL}\right)\right.\\ &\left.+\frac{(q^2-k_t^2)^2L}{k_t^2\cos^2(k_tL/2)}\left(1-\frac{\sin(k_tL)}{k_tL}\right)-8(q^2-k_t^2)\frac{\tan(k_tL/2)}{k_t}\right],\end{aligned}$$

and

$$\begin{aligned}\mathcal{N}_A^{-2} &= \frac{\Omega_\Lambda^2}{2c_t^2}\left[\frac{c_t^2}{c_l^2}\frac{4q^2L}{\sin^2(k_lL/2)}\left(1-\frac{\sin(k_lL)}{k_lL}\right)\right.\\ &\left.+\frac{(q^2-k_t^2)^2L}{k_t^2\sin^2(k_tL/2)}\left(1+\frac{\sin(k_tL)}{k_tL}\right)+8(q^2-k_t^2)\frac{\cot(k_tL/2)}{k_t}\right].\end{aligned}$$

Numerical solution of Eq. (4.21) yields the spectrum, Ω_Λ, for the symmetric mode ($\lambda = S$). The result is shown in Fig. 4.2. We distinguish three different regions, namely a case where both k_l and k_t are purely imaginary (region I), when only k_l is purely imaginary but k_t is real (region II), and finally a case where both k_l and k_t are real (region III). We observe from Fig. 4.2 that the $n = 1$ mode is the finite-width analogue of the well-known Rayleigh surface mode.[92,97] It has the dispersion relation

$$\Omega = c_R q, \quad c_R \simeq 0.92 c_t. \tag{4.24}$$

In fact, for $qL \gg 1$, both Eq. (4.21) and the corresponding equation for $\lambda = A$ reduce to

$$(q^2 + \kappa_t^2)^2 = 4q^2 \kappa_t \kappa_l.$$

As discussed in Ref. 97, this equation readily yields the sound velocity c_R of the Rayleigh mode.

4.3.1 Electron-phonon coupling

The dominant coupling of the above phonon modes to the electronic surface states comes from the deformation potential,[87] which couples the local electronic density $\hat{n}(\mathbf{r}, z)$ [Eq. (4.8)] to the divergence of the displacement vector, $\nabla \cdot \mathbf{U}(\mathbf{r}, z)$, see Eq. (4.15). Since the surface state density $\rho_\tau(z)$ in Eq. (4.9) is even in z, the antisymmetric phonon mode ($\lambda = A$) does not couple to the surface states. We therefore keep only the symmetric phonon mode from now on (and omit the index $\lambda = S$). Transforming Eq. (4.8) to the helical basis, see Eq. (4.5), the second-quantized electron-phonon coupling Hamiltonian reads

$$H_{\mathrm{e-ph}} = \frac{\alpha}{\sqrt{\mathcal{A}}} \sum_{\mathbf{q},\mathbf{k},n;\upsilon,s,s'} M^{(\upsilon,s,s')}_{\mathbf{k},\mathbf{q},n} b_{\mathbf{q},n} c^\dagger_{\mathbf{k}+\mathbf{q},\upsilon s} c_{\mathbf{k},\upsilon s'} + \mathrm{H.c.}, \tag{4.25}$$

where the M matrix elements involve the unitary matrices $[U_\upsilon(\mathbf{k})]_{s\sigma}$ in Eq. (4.4),

$$\begin{aligned} M^{(\upsilon,s,s')}_{\mathbf{k},\mathbf{q},n} &= -\frac{1}{\sqrt{2\rho_M \Omega_{q,n}}} \left(\frac{\Omega_{q,n}}{c_l}\right)^2 \sum_\sigma [U_\upsilon(\mathbf{k}+\mathbf{q})]^*_{s\sigma} [U_\upsilon(\mathbf{k})]_{\sigma s'} \\ &\quad \times \int_{-L/2}^{L/2} dz\ \rho_{\tau=\upsilon\sigma}(z) \phi_l(z), \end{aligned} \tag{4.26}$$

with the phonon dispersion $\Omega_{q,n}$ in Fig. 4.2; ϕ_l is given by Eqs. (4.19) and (4.22). The deformation potential strength α in Eq. (4.25) can be estimated as follows. The high-temperature behavior of the on-shell imaginary part of the electronic self-energy is (see Sec. 4.5)

$$\mathrm{Im}\Sigma(k, T) = -\pi \lambda_k k_B T, \tag{4.27}$$

which allows to experimentally extract the dimensionless effective electron-phonon coupling constant λ_k. The relation (4.27) has been observed for Bi_2Se_3 in ARPES experiments,[98] and $\lambda = 0.25 \pm 0.05$ has been measured. In these experiments, the Fermi level was near the bottom of the conduction band, $\mu \simeq 0.28$ eV, and k in Eq. (4.27) corresponds to energies ≈ 50 to 100 meV above the Dirac point. Computing λ_k within

our model, see Sec. 4.5, the observed value for λ corresponds to $\alpha = (30 \pm 8)$ eV. We employ the value $\alpha = 30$ eV below.

The total Hamiltonian employed in the following sections is then given by

$$H = H_{\rm el} + H_{\rm ph} + H_{\rm e-ph},$$

which are mentioned in Eqs. (4.6), (4.16) and (4.25). We first address the phonon-induced resistivity ρ in Sec. 4.4 and then turn to the quasi-particle lifetime in Sec. 4.5.

4.4 Resistivity

Here we discuss the T-dependent phonon contribution to the electrical resistivity, ρ, in the TI film, using the Hamiltonian described in Sec. 4.2. As explained in Sec. 4.3.1, only symmetric (dilatational) phonon modes can cause a finite resistivity for the low-energy surface states within the bulk gap. We compute ρ within the framework of the linearized Boltzmann equation,[99] which has also been employed previously for the related graphene case.[81,82] The resulting quasi-classical estimate for ρ is valid[81] as long as ρ is small compared to the resistance quantum, $\rho \ll h/e^2 \simeq 25.8$ kΩ. We sketch the standard derivation[81,82,91,100] for ρ in Appendix D. The result takes the form

$$\frac{1}{\rho} = \frac{e^2}{2} \sum_{\upsilon,s=\pm} \int \frac{d\mathbf{k}}{(2\pi)^2}\, v_{\mathbf{k},s}^2 \tau_\upsilon(\epsilon_{\mathbf{k},s}) \left[-\partial_\epsilon n_F(\epsilon_{\mathbf{k},s})\right], \tag{4.28}$$

where the dispersion relation for helical fermions [Eq. (4.7)] defines the group velocity, $v_{\mathbf{k},s} = \hat{e}_k \cdot \nabla_{\mathbf{k}} \epsilon_{\mathbf{k},s}$. Moreover, $n_F(\epsilon)$ is the Fermi function, and the energy-dependent electron-phonon transport scattering rate (inverse time) is

$$\frac{1}{\tau_\upsilon(\epsilon_{\mathbf{k},s})} = \sum_{\mathbf{q},s'} \left(1 - \frac{v_{\mathbf{k}+\mathbf{q},s'}}{v_{\mathbf{k},s}} \cos\theta_{\mathbf{k},\mathbf{q}}\right) \frac{1 - n_F(\epsilon_{\mathbf{k}+\mathbf{q},s'})}{1 - n_F(\epsilon_{\mathbf{k},s})} W_{(\mathbf{k},\upsilon s)\to(\mathbf{k}+\mathbf{q},\upsilon s')}, \tag{4.29}$$

where $\theta_{\mathbf{k},\mathbf{q}}$ is the angle between $\mathbf{k}$ and $\mathbf{k}+\mathbf{q}$, and the transition probabilities are obtained from Fermi's golden rule. Using Eq. (4.25), we find

$$\begin{aligned} W_{(\mathbf{k},\upsilon s)\to(\mathbf{k}+\mathbf{q},\upsilon s')} &= \frac{2\pi\alpha^2}{\mathcal{A}} \sum_{n;\nu=\pm} \nu n_B\left(\nu\Omega_{q,n}\right) \left|M_{\mathbf{k},\mathbf{q},n}^{(s',s)}\right|^2 \\ &\quad \times \delta\left(\epsilon_{\mathbf{k},s} + \nu\Omega_{q,n} - \epsilon_{\mathbf{k}+\mathbf{q},s'}\right), \end{aligned} \tag{4.30}$$

where $n_B(\epsilon)$ is the Bose function. While the M matrix elements (4.26) depend on the index $\upsilon = \pm$, we note that $|M|^2$ and therefore the transition probabilities W are υ-independent. This also implies that τ_υ does actually not depend on υ.

With the polar angle θ between $\mathbf{k}$ and $\mathbf{q}$, such that

$$\cos\theta_{\mathbf{k},\mathbf{q}} = \frac{k + q\cos\theta}{\sqrt{k^2 + q^2 + 2kq\cos\theta}}, \tag{4.31}$$

and taking into account the angular integration, the momentum relaxation rate can be written as:

$$\frac{1}{\tau(\epsilon_{\mathbf{k},s})} = \alpha^2 \sum_{n,\nu} \int_0^\infty q dq\, \mathcal{F}^{(\nu)}_{k,n,s}(q)\, \nu n_B(\nu\Omega_{q,n}) \frac{1 - n_F(\epsilon_{\mathbf{k}s} + \nu\Omega_{q,n})}{1 - n_F(\epsilon_{\mathbf{k}s})}, \tag{4.32}$$

where $\mathcal{F}^{(\nu)}_{k,n,s}(q)$ is the "transport Eliashberg function[87]"

$$\begin{aligned} \mathcal{F}^{(\nu)}_{k,n,s}(q) &= \sum_{s'} \int_{-\pi}^{\pi} \frac{d\theta}{2\pi} \left[1 - \frac{v_{\mathbf{k}+\mathbf{q},s'}}{v_{\mathbf{k},s}} \cos\theta_{\mathbf{k},\mathbf{q}}\right] \left|M^{(s',s)}_{\mathbf{k},\mathbf{q},n}\right|^2 \\ &\quad \times \delta\left(\epsilon_{\mathbf{k},s} + \nu\Omega_{q,n} - \epsilon_{\mathbf{k}+\mathbf{q},s'}\right). \end{aligned} \tag{4.33}$$

The θ-integration in Eq. (4.33) can then be carried out analytically, which is useful when computing $\mathcal{F}$ numerically, and the final expression is mentioned in Appendix E.

For low temperatures, the quasi-elastic approximation,

$$\Omega_{q,n} \ll \sqrt{(\Delta/2)^2 + (A_2 W k)^2},$$

is applicable and allows to simplify the full result for $\mathcal{F}$ to the ν-independent form

$$\mathcal{F}_{k,n,s}(q) = \Theta\left(2k - q\right) \frac{1}{\pi\sqrt{(2k/q)^2 - 1}} \frac{\sqrt{(\Delta/2)^2 + (A_2 W k)^2}}{(A_2 W k)^2} \left|M^{(s,s)}_{\mathbf{k},\mathbf{q},n}\right|^2 \Big|_{\theta_0}, \tag{4.34}$$

where $\Theta(y)$ is the Heaviside function and $\theta = \theta_0$ determines the polar angle between $\mathbf{k}$ and $\mathbf{q}$ appearing in the matrix element M, and is defined in the Appendix E. Note that there is no contribution from inter-band transitions at low temperatures.

4.4.1 Asymptotic behavior with temperature

The low and the high-temperature behavior in this system is measured with respect to the Bloch-Grüneisen temperature,[81,87]

$$T_{\mathrm{BG}} = 2k_F c_R / k_B, \tag{4.35}$$

with the Rayleigh velocity c_R in Eq. (4.24). $k_F(L)$ is defined by $\epsilon_{k_F,s=+} = 0$ with the dispersion relation (4.7).

For $T \ll T_{\mathrm{BG}}$, the $\mathcal{F}$ function can be approximated by the quasi-elastic expression [Eq. (4.34)]. It receives the dominant contribution from the $n = 1$ branch corresponding to the Rayleigh surface phonon. For small q, we find $\Omega_{q,n=1} = c_s q$ with $c_s = 2754$ m/s (which is slightly below c_l), see also Fig. 4.2. In addition, we have, phonon wave-function

$$\phi_l(z) = 2(c_t/c_s)^2/(q\sqrt{L})$$

and considering $c_s \ll \min(|v_{k_F}|, A_2 W)$, we have

$$\mathcal{F}_{k_F,1,\pm}(q) = \frac{(c_t/c_l)^4}{\pi\rho_M |v_{k_F}| c_s k_F^2} \frac{q^2}{L}.$$

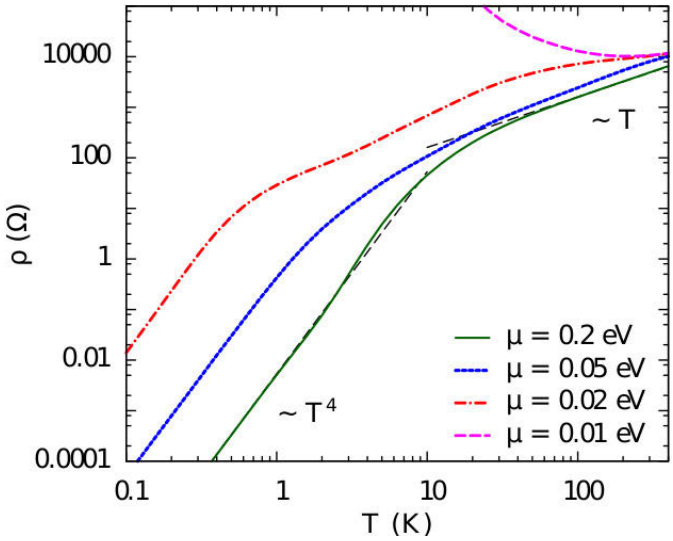

Figure 4.3: Phonon contribution to the resistivity ρ vs temperature T for a TI film of width $L = 4$ QL and several values of the chemical potential μ. Dashed lines indicate the analytical results for low [Eq. (4.36)] and high [Eq. (4.38)] temperatures. Note the double-logarithmic scale.

This allows us to perform all remaining integrations and yields a T^4 law for the resistivity at low temperatures,

$$\rho(T \ll T_{\mathrm{BG}}) = \frac{h}{e^2} A \left(\frac{T}{T_{\mathrm{BG}}}\right)^4, \tag{4.36}$$

where the dimensionless prefactor A is

$$\begin{aligned} A &= \frac{8\gamma k_F \alpha^2}{\pi \rho_M v_{k_F}^2 c_s} \left(\frac{c_t c_R}{c_l c_s}\right)^4 \frac{1}{L}, \\ \gamma &= \left[\int_{-\infty}^{\infty} dx \frac{2e^x}{[(\pi^2 + x^2)(e^x + 1)]^2}\right]^{-1} \simeq 68.4295. \end{aligned} \tag{4.37}$$

In the opposite high-temperature limit, essentially all phonon branches indexed by n contribute to the transport Eliashberg function (4.33), see Appendix E. Then the relaxation rate $\tau^{-1}(\epsilon_{\mathbf{k},s})$ in Eq. (4.32) is basically a linear function of the energy. Since the linear term does not contribute to ρ after integration in Eq. (4.28), we obtain the approximation $1/\rho \simeq (e^2/h) v_{k_F} k_F \tau(\epsilon = 0)$, where Eq. (4.32) yields the linear high-temperature law

$$\rho(T \gg T_{\mathrm{BG}}) = \frac{h}{e^2} C \frac{T}{T_{\mathrm{BG}}} \tag{4.38}$$

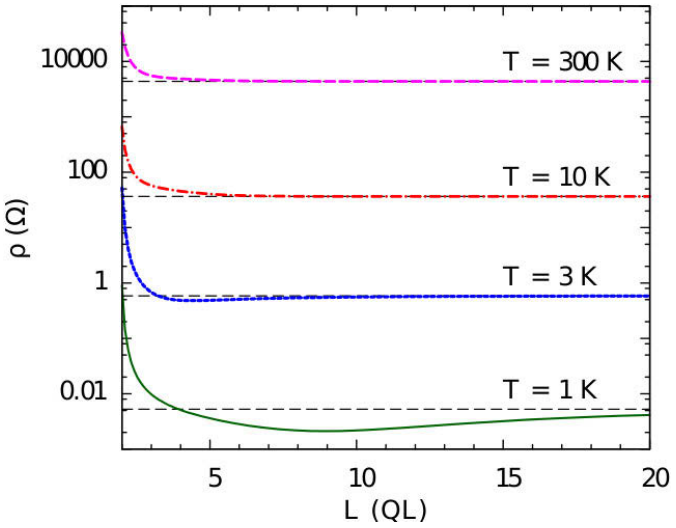

Figure 4.4: Width (L) dependence of the phonon contribution to the resistivity ρ for $\mu = 0.2$ eV and several temperatures. The dashed horizontal line indicates one-quarter of the resistivity $\rho_\infty(T)$ in the semi-infinite geometry of Ref. 87 with otherwise identical parameters.

with the dimensionless prefactor

$$C = \frac{2\alpha^2 c_R}{v_{k_F}} \sum_{n,\nu=\pm} \int_0^\infty q dq \frac{\mathcal{F}^{(\nu)}_{k_F,n,+}(q)}{\Omega_{q,n}}. \tag{4.39}$$

In Fig. 4.3 we show the full temperature dependence of ρ obtained numerically for a fixed width $L = 4$ QL and several values of the chemical potential μ. In that case, when measured relative to E_0^∞, we have $E_0^+ \simeq 16$ meV and $\Delta/2 \simeq 13$ meV. For the lowest μ in Fig. 4.3, the Fermi level is thus located inside the surface gap and one has a very large resistivity, where the quasi-classical approach is not reliable in any case. For low temperatures, $T < T_{\rm BG}$, the analytical result (4.36) with $\rho \propto T^4$ is nicely reproduced by numerics. In this temperature regime, only the Rayleigh mode ($n = 1$) is relevant. In the high-temperature limit, both the $\rho \propto T$ scaling and the prefactor C in Eq. (4.39) are also consistent with our numerical findings.

$L \to \infty$ limit

In the low temperature limit, for $L \to \infty$, A given in (4.37) obviously vanishes. This suggests that for elevated temperatures (but still $T < T_{\rm BG}$) and finite L, the T^4 law is no more the case. Actually, as shown in reference 87, for the semi-infinite geometry, the low-temperature behavior is $\rho \propto T^5$. We can estimate the crossover temperature T_c as follows. For $T < T_{\rm BG}$, we expect an expansion of the form

$$(e^2/h)\rho = A(T/T_{\rm BG})^4 + \frac{B}{4}(T/T_{\rm BG})^5,$$

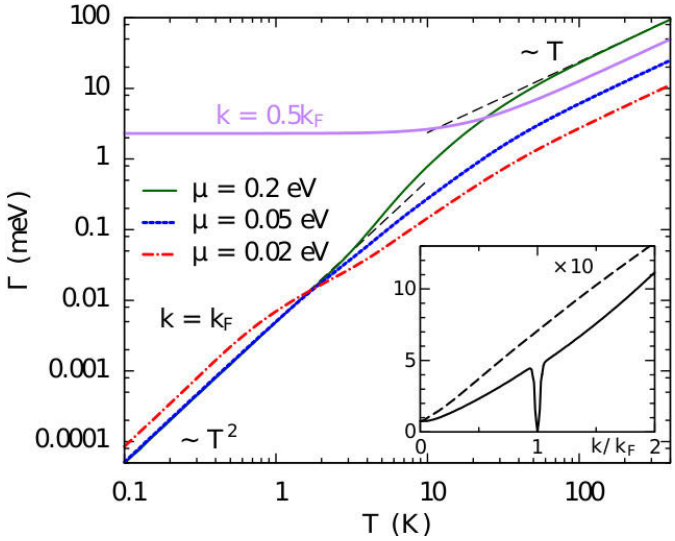

Figure 4.5: Main panel: T-dependence of the decay rate Γ of a TI film of width $L = 4$ QL for $k = k_F$ and $k = 0.5k_F$. For $k = 0.5k_F$, only the $\mu = 0.2$ eV result is displayed. Dashed lines indicate the low- and high-temperature laws ($\Gamma \propto T^2$ and $\propto T$), respectively. Inset: k-dependence of Γ for $\mu = 0.2$ eV and two different temperatures: $T = 3$ K (solid line) and $T = 300$ K (dashed line; the shown result has to be multiplied by 10).

with $A \propto 1/L$ in Eq. (4.36) and the L-independent constant B given in Ref. 87:

$$B = \frac{1488\zeta(5)C_B}{\pi} \frac{\alpha^2 c_R^3 k_F^2}{\rho_M v_F^2 c_l^4} \ , \tag{4.40}$$

where $\zeta(5) \approx 1.037$ and $C_B \approx 1.20$. The crossover from the T^4 law (for $T \lesssim T_c$) to the T^5 law (for $T_c \lesssim T < T_{\rm BG}$) thus happens around the temperature $T_c = (4A/B)T_{\rm BG}$. This gives $T_c \simeq 0.14 T_{\rm BG}/(k_F L)$, which is independent of the chemical potential since $T_{\rm BG} \propto k_F$. For $L = 4$ QL, we obtain $T_c \approx 0.9$ K. The T^4 law can thus only be observed for very thin and clean TI films.

Finally, Fig. 4.4 shows the width (L) dependence of ρ at fixed chemical potential and for several T. Two noteworthy observations can be drawn from Fig. 4.4: First, for low temperatures we observe a "dip" in Fig. 4.4, where $\rho(L) < \rho(L \to \infty)$ for intermediate values of L.

We also note that, for $L \to \infty$, $\rho(L)$ approaches 1/4 of the single-surface value $\rho_\infty(T)$ obtained for the semi-infinite geometry.[87] Naively, we would expect $\rho(L \to \infty) = \rho_\infty/2$ because of the presence of two surfaces in the film geometry. This discrepancy indicates that the $L \to \infty$ limit is singular, and it is not possible to really decouple both surfaces in such an interacting system; see also Ref. 101 and 102 for a related discussion.

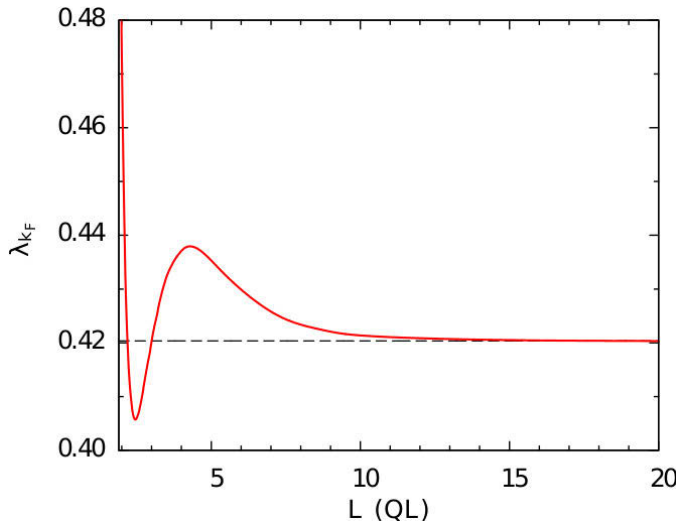

Figure 4.6: Width (L) dependence of the effective electron-phonon coupling constant at the Fermi level λ_{k_F} for $\mu = 0.2$ eV. The dashed horizontal line indicates one-half of the effective coupling constant in the semi-infinite geometry with otherwise identical parameters.

4.5 Lifetime Broadening

Next we discuss the quasi-particle lifetime (inverse decay rate) for the surface fermions in the TI film due to their coupling to phonons, see $H_{\rm e-ph}$ in Eq. (4.25), which implies a finite linewidth of ARPES spectral features. The decay rate, $\Gamma_k(T) = -2{\rm Im}\Sigma$, follows from the imaginary part of the on-shell self-energy $\Sigma_{s=+}(\mathbf{k}, \omega = \epsilon_{\mathbf{k},s=+})$.

Expanding up to second order in $H_{\rm e-ph}$, the "rainbow" diagram yields the self-energy

$$\begin{aligned}\Sigma_s(\mathbf{k},\omega) &= \alpha^2 \sum_{n,s'} \int \frac{d\mathbf{q}}{(2\pi)^2} \left| M^{(s',s)}_{\mathbf{k},\mathbf{q},n} \right|^2 \\ &\times \sum_{\nu=\pm} \nu \frac{n_B(\nu\Omega_{q,n}) + n_F(\epsilon_{\mathbf{k}+\mathbf{q},s'})}{\omega + i0^+ + \nu\Omega_{q,n} - \epsilon_{\mathbf{k}+\mathbf{q},s'}}.\end{aligned} \tag{4.41}$$

Introducing the Eliashberg function $F^{(\nu)}_{k,n,s}(q)$ exactly as the transport Eliashberg function $\mathcal{F}$ in Eq. (4.33) but without the factor $[1-(v_{\mathbf{k}+\mathbf{q},s'}/v_{\mathbf{k},s})\cos\theta_{\mathbf{k},\mathbf{q}}]$, the quasi-particle decay rate follows as

$$\begin{aligned}\Gamma_k(T) &= \alpha^2 \sum_{n,\nu} \int_0^\infty q dq\; F^{(\nu)}_{k,n,+}(q) \\ &\times \left[n_B(\Omega_{q,n}) + n_F(\Omega_{q,n} + \nu\epsilon_{k,+}) \right].\end{aligned} \tag{4.42}$$

Expanding this result for high temperatures, $T \gg T_{\rm BG}$, as in Sec. 4.4.1 yields, see also

Eq. (4.27), a linear T-dependence,

$$\begin{aligned} \Gamma_k(T \gg T_{\rm BG}) &= 2\pi\lambda_k k_B T, \\ \lambda_k &= \frac{\alpha^2}{2\pi}\sum_{n,\nu}\int_0^\infty qdq\,\frac{F^{(\nu)}_{k,n,+}(q)}{\Omega_{q,n}}. \end{aligned} \tag{4.43}$$

The L-dependence of λ_k is shown for $k = k_F$ in Fig. 4.6. We observe an oscillatory dependence, with a saturation at one-half of the corresponding semi-infinite result.

For low temperatures and $k = k_F$, the decay rate is dominated by the $n = 1$ phonon mode with $q \to 0$. After some algebra, we find that this implies a T^2 law,

$$\Gamma_{k_F}(T \ll T_{\rm BG}) = \frac{4\pi(c_t/c_l)^4(k_F c_R\alpha)^2}{\rho_M|v_{k_F}|c_s^3}\frac{1}{L}\left(\frac{T}{T_{\rm BG}}\right)^2. \tag{4.44}$$

Again, when $T \gtrsim T_c$, the T^2 law (which scales $\propto 1/L$) competes with the L-independent T^3 law found in Ref. 87, see Sec. 4.4. Finally, when $k \neq k_F$ and $T \ll T_{\rm BG}$, the quasi-particle decay rate saturates at the finite value

$$\Gamma_{k\neq k_F} = \alpha^2\sum_n\int_0^\infty qdq\,\Theta(|\epsilon_{k+}| - \Omega_{q,n})\;F^{(\nu)}_{k,n,+}(q). \tag{4.45}$$

with $\nu = \mathrm{sgn}(k_F - k)$.

Figure 4.6 shows that the $L \to \infty$ limit of the decay rate always tends to $\Gamma_\infty(T)/2$, where Γ_∞ is the corresponding decay rate for the semi-infinite geometry.[87] This discrepancy with the naive expectation $\Gamma(L \to \infty) = \Gamma_\infty$ has the same origin as the anomalous factor $1/2$ appearing in the large-L behavior of the resistivity discussed in Sec. 4.4.

4.6 Summary & Discussion

Here we have studied the effects of long-wavelength acoustic phonons on the topologically protected surface fermions in topological insulator films. Our model employs the established low-energy electronic Hamiltonian and an isotropic elastic continuum approach for the phonons, with the deformation coupling providing the dominant interaction mechanism. The electron-phonon coupling turns out to be surprisingly strong, in accordance with recent ARPES results.[98]

Using a quasi-classical approach, we have computed the temperature-dependent resistivity of the film due to phonon backscattering, and found a linear T dependence above the Bloch-Grüneisen temperature. In this temperature regime, the phonon-induced resistivity can overcome the disorder-induced (T-independent) contribution and should be observable with present samples. Similarly, the linear T dependence of the quasi-particle decay rate found here is observable[98] in ARPES experiments. The low-temperature behaviors of the resistivity and of the quasi-particle decay rate are probably more difficult to observe.

Here, we note that, in an usual metal also the resistivity becomes proportional to temperature at large temperature. This reflects the bosonic nature of the phonons that

scatter the electrons: at temperatures greater than the Debye temperature, the phonon population in any given mode is proportional to T, hence the number of scatterers and the resistivity are proportional to T. At low temperature, resistivity in Graphene also varies as $\propto T^4$.

Possible experiment

To the best of our knowledge, no detailed measurements for the temperature dependence of the TI film resistivity have been reported so far. In the related case of a 2D graphene monolayer, a similar comparison of theory[81,82] to experiment[83] has turned out to be successful. Remarkably, the electron-phonon coupling observed in Ref. 98 and independently estimated by Ref. 87 turns out to be quite large. Under room temperature conditions, the resulting lifetime of helical quasi-particles is therefore short, and the resistivity is rather large. This behavior is substantially different from what is found in graphene. We suspect that this is (partially) due to the different Debye temperatures in both materials.

Possible future extension

An interesting extension of our work would be to include the effects of a magnetic field. Magneto-transport measurements in thin films were recently performed[103] and found clear evidence for Landau level formation associated with the massless Dirac fermions forming on both surfaces. The observed broadening of the Landau levels was assigned to disorder and/or interaction effects, but at elevated temperatures, our analysis indicates that electron-phonon interactions may be relevant as well.

Chapter 5

Magnetic Scattering

5.1 Introduction

In the first chapter we discussed that, despite being structurally completely different, the low energy properties of un-doped graphene and 2D surface of a 3D TI corresponds to massless 2D Dirac Fermions. This calls for a unified description of their transport properties.

There already are many theoretical efforts to advancing the scattering theory of Dirac fermions on graphene in electrostatic potentials,[39,104] in particular for the Coulomb impurity.[105] In this chapter, we instead study the scattering of massless Dirac fermions by a local *magneto static perturbation*. The model we used describes in a unified manner, the effects of spatially inhomogeneous orbital magnetic fields, exchange-mediated fields due to adjacent ferromagnetic (FM) layers and Zeeman fields in topological insulators, as well as strain- or defect-induced pseudo-magnetic fields in graphene. For the Schrödinger fermions realized in 2D semiconductor electron gases, such perturbations, e.g., magnetically defined barriers, steps, and quantum wells, have been investigated both theoretically[106–109] and experimentally.[110,111]

Previously the theoretical works on TIs in inhomogeneous magnetic fields has addressed only a few setups. For the transmission of an electron through a magnetic barrier (assumed homogeneous in the transverse direction), as a function of either exchange field or applied bias voltage, Mondal *et al.*[112,113] predict an oscillatory behavior or even a complete suppression of the transmission probability, and hence of the conductance. A spin valve geometry with two adjacent magnetic barriers, characterized by non-collinear exchange fields, has also been studied.[114] As a model for a classical magnetic impurity, the spin-resolved density of states was calculated for a disc-shaped magnetic field profile.[115,116]

For graphene, a vector potential perturbation can again be due to external orbital fields, but may also describe the effects of strain[39,117–121] and dislocations or other topological defects.[122] Several theoretical works have addressed aspects of the electronic structure and the transmission properties for Dirac fermions in graphene in the presence of inhomogeneous magnetic fields. The simplest case is encountered for effectively 1D

problems with translational invariance in the (say) y-direction, e.g., for a magnetic step or a magnetic barrier.[47,48,123] For suitable 1D magnetic field profiles, it is possible to have magnetic waveguides (along the y-direction),[124,125] where electron-electron interaction effects play an important role.[126] Periodic magnetic fields, i.e., 1D magnetic superlattices, have also been addressed.[127–130]

For a radially symmetric fields, total angular momentum conservation again simplifies the problem and gives an effective 1D theory. This has allowed for studies of quantum dot or antidot geometries,[47,48,131,132] where true bound states, not affected by Klein tunneling, may exist. In quantum dot setups, interaction effects become important for strong confinement.[133] When the vector potential corresponds to an infinitely thin solenoid, we encounter an ultra-relativistic Dirac fermion generalization of the celebrated Aharonov-Bohm (AB) calculation.[134,135] This generalization was discussed before,[136–141] and exact results for the transmission amplitude can be deduced. Recent studies have also addressed the current induced by an AB flux[142] and the behavior of the conductance when the chemical potential is precisely at the Dirac neutrality point.[143] Such an AB conductance can be probed experimentally in ring-shaped graphene devices.[144,145]

In this chapter, we formulate a general scattering theory approach for massless 2D Dirac fermions in the presence of such magnetic perturbations. In Sec. 5.2, we introduce the model and outline its application to graphene and topological insulators. In Sec. 5.3, we formulate the general scattering theory, previously given for electrostatic potentials,[104] for the magnetic case. The scattering amplitude and cross section are specified, and we discuss the Born approximation in Sec. 5.3.2. For the radially symmetric case, total angular momentum conservation allows to express the scattering amplitude in terms of phase shifts for given total angular momentum, which we discuss in Sec. 5.3.3. In sections 5.4, we present a applications of this formalism, where we consider *ring-shaped field profiles*. This case also contains the AB solenoid in a certain limit and we discuss how our phase-shift analysis recovers known results for the AB effect.

5.2 Model Hamiltonian

Our starting point is the generalized Hamiltonian including the possible magnetic effects. With the Pauli matrices $\boldsymbol{\sigma} = (\sigma_x, \sigma_y, \sigma_z)$ and the momentum operator $\boldsymbol{p} = -i\hbar(\partial_x, \partial_y, 0)$, the single-particle model reads ($e > 0$)

$$H = v_F \boldsymbol{\sigma} \cdot \Big(\boldsymbol{p} + \frac{e}{c} \boldsymbol{A}(\boldsymbol{r}) \Big) + \boldsymbol{\sigma} \cdot \boldsymbol{M}(\boldsymbol{r}) - eV(\boldsymbol{r}), \tag{5.1}$$

where the external static vector potential, $\boldsymbol{A}(\boldsymbol{r}) = (A_x, A_y, A_z)$ with $\boldsymbol{r} = (x, y)$, included by minimal coupling, describes orbital magnetic fields and (for graphene) strain-induced pseudo-magnetic fields. In addition, for the TI case, we allow for a Zeeman field or for exchange fields caused by nearby ferromagnets, whose components are contained in the field $\boldsymbol{M}(\boldsymbol{r}) = (M_x, M_y, M_z)$, where prefactors such as the Bohr magneton or the Landé factor are included.

The non-magnetic model ($\boldsymbol{A} = 0$, $\boldsymbol{M} = 0$) for graphene and TI are already discussed in Sec. 1.3.3 and Sec. 2.3.1 respectively. The Fermi velocity in graphene is $v_F \simeq 10^6$ m/s, while for a TI surface state, a typical value for Bi_2Se_3 is $v_F \approx 5 \times 10^5$ m/s.

Both the vector potential $\boldsymbol{A}$ and the field $\boldsymbol{M}$ can now be combined to a vector field

$$\boldsymbol{\Lambda}(\boldsymbol{r}) \equiv \boldsymbol{A} + \frac{c}{ev_F}\boldsymbol{M}, \tag{5.2}$$

which contains all considered "magnetic" perturbations. Interesting physics also follows in the presence of both $\boldsymbol{\Lambda}(\boldsymbol{r})$ and a scalar potential $V(\boldsymbol{r})$, but we put $V(\boldsymbol{r}) = 0$ below.

For the formulation of the scattering theory, it is convenient to employ cylindrical coordinates, $x = r\cos\phi$ and $y = r\sin\phi$, with unit vectors $\hat{e}_r = (\cos\phi, \sin\phi, 0)$, $\hat{e}_\phi = (-\sin\phi, \cos\phi, 0)$, and $\hat{e}_z$. With $\boldsymbol{\Lambda} = \Lambda_r\hat{e}_r + \Lambda_\phi\hat{e}_\phi + \Lambda_z\hat{e}_z$, Eq. (5.1) takes the compact form

$$\begin{aligned} H &= v_F e^{-i\phi\sigma_z/2}\tilde{H}e^{i\phi\sigma_z/2}, \\ \tilde{H} &= \left(-i\hbar\partial_r + \frac{e}{c}\Lambda_r\right)\sigma_x + \left(\frac{1}{r}J_z + \frac{e}{c}\Lambda_\phi\right)\sigma_y, \end{aligned} \tag{5.3}$$

where the total angular momentum operator is

$$J_z = -i\hbar\partial_\phi + \hbar\sigma_z/2. \tag{5.4}$$

For the case of azimuthal symmetry, $\partial_\phi\Lambda_{\phi,r} = 0$, this is a conserved quantity, $[J_z, H] = 0$, with eigenvalues $\hbar j$ for half-integer j. In Eq. (5.3) we have put $\Lambda_z = 0$, which is the case for all fields studied below.

For the Hamiltonian (5.3), one writes the Schrödinger equation $i\hbar\partial_t\psi = H\psi$, and obtains the corresponding continuity equation

$$\partial_t(\psi^\dagger\psi) + \boldsymbol{\nabla}\cdot(\psi^\dagger\boldsymbol{\sigma}\psi) = 0\ . \tag{5.5}$$

From this one can identify the current operator $\boldsymbol{j} = \psi^\dagger\boldsymbol{\sigma}\psi$. Also, as we discuss in Sec. 1.2.8, in a TI surface the spin and surface are locked and the spin density ($\boldsymbol{s}$) is perpendicular to momentum, that is

$$\boldsymbol{s}\cdot\boldsymbol{j} = 0\ .$$

So, we write the spin density operator

$$\boldsymbol{s} = \frac{\hbar}{2}(\hat{e}_z\times\boldsymbol{\sigma})\ . \tag{5.6}$$

Under stationary conditions, the continuity equation (5.5) implies the relation

$$\sum_{i=x,y}\partial_i\left(\psi^\dagger\sigma_i\psi\right) = 0\ , \tag{5.7}$$

which is linked to the unitarity property of the scattering matrix. Equation (5.3) then allows to describe the following setups for the TI surface state. First, an orbital magnetic field has only effects when it is oriented perpendicular to the surface, $\boldsymbol{B}_{\rm orb} = B_z(r,\phi)\hat{e}_z$.

In cylindrical coordinates, we can then choose some gauge for the vector potential $\boldsymbol{A}$ such that

$$B_z(r,\phi) = \frac{1}{r}\left(\partial_r(rA_\phi) - \partial_\phi A_r\right), \tag{5.8}$$

while A_z drops out and is put to zero.

Secondly, to describe the coupling of surface Dirac fermions to an *in-plane exchange field* $\boldsymbol{H}(\boldsymbol{r}) = (H_x, H_y, 0)$, e.g., due to the magnetization of a nearby FM layer, we write

$$\boldsymbol{\Lambda} = (c/ev_F)\boldsymbol{M} \ ,$$

with $\boldsymbol{M} = (-H_y, H_x, 0)$, where we used the spin Pauli matrices in Eq. (5.6). For a Zeeman field, we can proceed in complete analogy where $\boldsymbol{H}$ now denotes the Zeeman field. A Zeeman or exchange field oriented along the $\hat{e}_z$ direction can open a gap in the spectrum, and here we assume that such fields are not present. While the orbital field breaks time reversal invariance, the Zeeman or exchange fields represent a time-reversal invariant perturbation. Then $\boldsymbol{\Lambda}$ is determined by the magnetic field itself, and hence is not a gauge field anymore.

In the case of *graphene* the Pauli matrices $\boldsymbol{\sigma}$ are related to the two triangular sublattices constituting graphene's honeycomb lattice. We assume that no spin-flip mechanisms are relevant, i.e., physical spin is conserved. We can then focus on one specific Dirac fermion flavor with fixed valley index and spin direction. This excludes exchange or Zeeman fields, i.e., we put $\boldsymbol{M} = 0$ and hence $\boldsymbol{\Lambda} = \boldsymbol{A}$ for graphene. Note that Zeeman fields in graphene are generally small compared to orbital fields.[126] Moreover, we consider only smoothly varying vector potentials such that it is indeed sufficient to retain only one K point.[47] Equation (5.3) can then describe the following cases. First, we may have an orbital magnetic field, precisely as for the TI case. Second, pseudo-magnetic fields generated by strain-induced forces,[39,116,118–121] or by various types of defects, e.g., dislocations,[122] also correspond to a vector potential, where time reversal invariance implies that $\boldsymbol{A}$ has opposite sign at the two K points. $\boldsymbol{A}(\boldsymbol{r})$ can then be expressed explicitly in terms of the strain tensor,[122] where the resulting pseudo-magnetic field is also oriented along the $\hat{e}_z$ axis and $A_z = 0$. In addition, strain causes a scalar potential $V(\boldsymbol{r})$, which is, however, strongly reduced by screening effects. The combination of orbital and pseudo-magnetic fields may allow to design a valley filter, since the total (orbital plus pseudo-magnetic) fields can differ significantly at both K points.[146]

5.3 Scattering Theory

In the quantum theory of time-independent elastic scattering, we search for the solution $|\psi\rangle$ of the total Hamiltonian

$$H = H_0 + V,$$

where H_0 is the free particle Hamiltonian with eigenstate $|\phi\rangle$

$$H_0|\phi\rangle = E|\phi\rangle,$$

V represents the potential due to scatterer, such that $|\psi\rangle \to |\phi\rangle$ in the limit of $V \to 0$, and also they require to have the same eigenvalue E, as the process is elastic:

$$(H_0 + V)|\psi\rangle = E|\psi\rangle. \tag{5.9}$$

The scattering theory argues that the solution is:

$$|\psi\rangle = \frac{1}{E - H_0}|\psi\rangle + |\phi\rangle. \tag{5.10}$$

If $|\phi\rangle = |\psi_{\rm in}\rangle$ represents the incoming wave, then the scattering theory is better formulated by defining the solution $|\psi\rangle = |\psi_{\rm in}\rangle + |\psi_{\rm out}\rangle$, where $|\psi_{\rm out}\rangle$ is the out-going wave scattered from the potential, and represented by spherical wave. Then the equation (5.10) looks like:

$$|\psi_{\rm in}\rangle + |\psi_{\rm out}\rangle = \frac{1}{E - H_0}(|\psi_{\rm in}\rangle + |\psi_{\rm out}\rangle) + |\psi_{\rm in}\rangle. \tag{5.11}$$

This integral equation can be solved iteratively. In the first Born approximation (ref. landau), we approximate $(|\psi_{\rm in}\rangle + |\psi_{\rm out}\rangle) \approx |\psi_{\rm in}\rangle$ on the right side of the equation.

Following Landau-Lifshitz,[97] if, in 2D, the incoming wave is of the form

$$\psi_{\rm in}(r, \phi) \propto e^{ikx}, \tag{5.12}$$

then the scattered wave can be written as

$$\psi_{\mathbf{out}} = F(\phi)\frac{e^{ikr}}{\sqrt{-2ir}}, \tag{5.13}$$

where $F(\phi)$ is called the *scattering amplitude*. We have chosen the normalisation similar as Ref. 104 and 97. The physical quantities of interest are differential ($d\sigma/d\phi$), total ($\sigma_{\mathbf{tot}}$) and transport (σ_r) cross sections:

$$\begin{aligned} \frac{d\sigma}{d\phi} &= |F(\phi)|^2, \\ \sigma_{\rm tot} &= \int_0^{2\pi} d\phi\ |F(\phi)|^2 = \sqrt{\frac{8\pi}{k}}\ {\rm Im}F(0), \\ \sigma_{\rm tr} &= \int_0^{2\pi} d\phi\ (1 - \cos\phi)\ |F(\phi)|^2\ , \end{aligned} \tag{5.14}$$

where the second equation represents optical theorem.

For given energy $E = \hbar v_F k$, where $k > 0$ throughout, the Dirac equation, $H\psi = E\psi$ with Eq. (5.3), has scattering solutions that we wish to obtain in the presence of magnetic perturbations of the type in Eq. (5.16). [i] We are then looking for a solution $\psi(r, \phi) = \psi_{\rm in} + \psi_{\rm out}$ consisting, in the asymptotic regime $r \to \infty$, of a plane wave ($\propto e^{ikx}$) propagating along the positive x-direction,

$$\psi_{\rm in}(r, \phi) = \frac{1}{\sqrt{2}} e^{ikr\cos\phi} \begin{pmatrix} 1 \\ 1 \end{pmatrix}, \tag{5.15}$$

[i] The solution for $E = -\hbar v_F k$ follows simply by reversing the sign of the lower spinor component.[147]

5.3.1 Multipole expansion

Our scattering theory approach considers magnetic fields [described by $\mathbf{\Lambda}(\boldsymbol{r})$ in Eq. (5.3)] that smoothly vary on the scale of a lattice spacing and constitute a *local* perturbation, i.e., a well-defined cylindrical multipole expansion exists. $\Lambda_z = 0$ is assumed throughout, as it opens up a gap. Furthermore, we assume that $\Lambda_r = 0$.

As we show below, for orbital fields we can always choose a gauge where $A_r = 0$. For strain-induced fields, strictly speaking, the problem is not gauge invariant, and we cannot impose gauge conditions. However, in a more narrow sense, a gauge degree of freedom still exists.[122]

For $r \to \infty$, with complex-valued coefficients $\alpha^{(\phi)}_{l,m} = \left(\alpha^{(\phi)}_{l,-m}\right)^*$, we have the multipole expansion

$$\Lambda_\phi(r,\phi) = \frac{\alpha\Phi_0}{2\pi r} + \sum_{l=2}^{\infty}\sum_{m=-\infty}^{\infty} \frac{e^{im\phi}}{r^l}\alpha^{(\phi)}_{l,m}, \tag{5.16}$$

where α denotes the total flux in units of the flux quantum $\Phi_0 = 2\pi\hbar c/e$.

In the case of orbital magnetic field, $\mathbf{\Lambda} = \boldsymbol{A}$, where we can exploit gauge invariance. We start from a more general situation with $A_r \neq 0$, expressed as in Eq. (5.16) with coefficients $\alpha^{(r)}_{l,m}$, and also allow for nonzero coefficients $\alpha^{(\phi)}_{l=1,m\neq 0}$. We now show that one can choose a gauge where $A_r = 0$ and $\alpha^{(\phi)}_{1,m\neq 0} = 0$. Indeed, gauge invariance implies that for arbitrary functions $g(x,y)$, we are free to replace $A_i \to A_i + \partial_i g$. Using a multipole expansion for $rg(r,\phi)$ with coefficients $g_{l,m}$, an equivalent gauge choice thus follows by the replacement

$$\begin{aligned} \alpha^{(\phi)}_{l,m} &\to \alpha^{(\phi)}_{l,m} + img_{l,m}, \\ \alpha^{(r)}_{l,m} &\to \alpha^{(r)}_{l,m} - (l-1)g_{l,m}. \end{aligned}$$

We then choose the gauge function

$$g_{l>1,m} = \frac{\alpha^{(r)}_{l,m}}{l-1}, \quad g_{l=1,m\neq 0} = \frac{i\alpha^{(\phi)}_{1,m}}{m}.$$

In the new gauge, we arrive at Eq. (5.16) plus the radial component

$$A_r = \sum_m \frac{e^{im\phi}}{r}\alpha^{(r)}_{1,m}.$$

Using Eq. (5.8), the orbital field expansion (with $r > 0$) reads

$$B_z(r,\phi) = -\sum_{l=1}^{\infty}\sum_{m=-\infty}^{\infty} \frac{e^{im\phi}}{r^{l+1}}\left[(l-1)\alpha^{(\phi)}_{l,m} + im\delta_{l,1}\alpha^{(r)}_{1,m}\right].$$

The $m = 0$ term in A_r neither generates flux nor magnetic fields and can be omitted. Magnetic field profiles with $\alpha^{(r)}_{1,m} \neq 0$ arise only in time-dependent settings and will not be studied here. As a consequence, the radial component vanishes, $A_r = 0$, and we arrive at Eq. (5.16).

5.3.2 Born approximation

For small perturbation $\Lambda_\phi(r,\phi)$, one can evaluate the scattering amplitude within the first Born approximation.[148] Strictly speaking, the long-ranged part $\Lambda_\phi \propto \alpha/r$ in Eq. (5.16) can not be treated perturbatively, and in this section we assume $\alpha = 0$.

The unperturbed state is the incoming plane wave $\psi_{\rm in}$, Eq. (5.15). Within lowest-order perturbation theory, the scattered wave obeys

$$[H_0 - E]\psi_{\rm out} = -\frac{ev_F}{c}\Lambda_\phi \ \hat{e}_\phi \cdot \boldsymbol{\sigma} \ \psi_{\rm in}, \tag{5.17}$$

where H_0 is the unperturbed Dirac Hamiltonian. Multiplying both sides of Eq. (5.17) by $H_0 + E$ and noting that in real-space representation, the retarded Green's function $(H_0^2 - E^2)^{-1}$ is given by the Hankel function $H_0^{(1)}$,[104,149]

$$\begin{aligned}\psi_{\rm out}(\boldsymbol{r}) &= \frac{-i\pi}{2\sqrt{2}\hbar\Phi_0}\int d^2\boldsymbol{r}' \ H_0^{(1)}(k|\boldsymbol{r}-\boldsymbol{r}'|)(\boldsymbol{\sigma}\cdot\boldsymbol{p}' + \hbar k) \\ &\times \ \Lambda_\phi(r',\phi') \ [\hat{e}_{\phi'}\cdot\boldsymbol{\sigma}] \ e^{ikr'\cos\phi'}\begin{pmatrix}1\\1\end{pmatrix}.\end{aligned}$$

The asymptotic large-ρ behavior of the Hankel function (where $\eta = 1, 2 = \pm$) is[149]

$$H_\nu^{(\eta)}(\rho) \simeq \sqrt{\frac{2}{\pi\rho}} \ e^{\pm i(\rho - (2\nu+1)\pi/4)}, \tag{5.18}$$

which implies that $\psi_{\rm out}$ for $r \to \infty$ has the form

$$\psi_{\rm out}(r,\phi) = F(\phi)\frac{e^{ikr}}{\sqrt{-2ir}}\begin{pmatrix}1\\ e^{i\phi}\end{pmatrix}. \tag{5.19}$$

After some algebra, we obtain the scattering amplitude in Born approximation,

$$\begin{aligned}F(\phi) &= \frac{\sqrt{2\pi k}}{\Phi_0}e^{-i\phi/2}\int_0^\infty r dr \int_0^{2\pi} d\phi' \ \sin\phi' \\ &\times \ e^{-2ikr|\sin(\phi/2)|\sin\phi'} \ \Lambda_\phi(r,\phi'+\phi/2).\end{aligned} \tag{5.20}$$

For radially symmetric perturbations, $\partial_\phi\Lambda_\phi = 0$, the ϕ'-integration can be done, and we obtain

$$\begin{aligned}F(\phi) &= -2\pi i\frac{\sqrt{2\pi k}}{\Phi_0}e^{-i\phi/2} \\ &\times \ \int_0^\infty r dr \ J_1\left(2kr|\sin(\phi/2)|\right) \ \Lambda_\phi(r),\end{aligned} \tag{5.21}$$

with the J_1 Bessel function.

5.3.3 Radially symmetric case

Here we address the full (beyond Born approximation) scattering solution for radially symmetric perturbations, $\mathbf{\Lambda} = \Lambda_\phi(r)\hat{e}_\phi$. In that case, the total angular momentum operator J_z in Eq. (5.4) is conserved and has eigenvalues $\hbar j$ with $j \equiv m + 1/2$ (m is an integer). We thus expand the spinor wavefunction in terms of angular momentum partial waves $\psi_m(r) \equiv (f_m, ig_m)^T$,

$$\psi(r,\phi) = e^{-i\phi\sigma_z/2} \sum_{m=-\infty}^{\infty} e^{i(m+1/2)\phi}\ \psi_m(r), \tag{5.22}$$

where the Dirac equation yields

$$\left[-i\left(\partial_r + \frac{1}{2r}\right)\sigma_x + \frac{m+1/2+\varphi(r)}{r}\sigma_y\right]\psi_m = k\psi_m. \tag{5.23}$$

The magnetic flux (in units of the flux quantum Φ_0) enclosed by a circle of radius r around the origin is

$$\varphi(r) \equiv \frac{2\pi r}{\Phi_0}\Lambda_\phi(r), \tag{5.24}$$

where $\alpha = \varphi(\infty)$ in Eq. (5.16). The continuity relation (5.7) must hold for each partial wave ψ_m separately, and implies in the cylindrical coordinates

$$\partial_r\left(r\psi_m^\dagger\sigma_x\psi_m\right) = 0. \tag{5.25}$$

Introducing dimensionless radial coordinates, $\rho \equiv kr$, a closed equation for the upper component, $f_m(\rho)$, follows,

$$\begin{aligned}\left[\frac{1}{\rho}\partial_\rho(\rho\partial_\rho) + 1 - \left(\frac{1}{4\rho^2} + W_m^2 + W_m'\right)\right] f_m = 0,\\ W_m(\rho) \equiv \frac{m+1/2+\varphi(\rho/k)}{\rho},\end{aligned} \tag{5.26}$$

where $W_m' \equiv \partial_\rho W_m$. The lower component is obtained from

$$g_m(\rho) = -\left(\partial_\rho + \frac{1}{2\rho} - W_m\right) f_m. \tag{5.27}$$

These relations imply a general expression for the scattering amplitude $F(\phi)$ under radially symmetric magnetic perturbations, and thus for the various cross sections in Eq. (5.14). For $\rho \to \infty$, the term $\propto \alpha/r$ in Eq. (5.16) dominates and the general solution to Eq. (5.26) is given in terms of Hankel functions,

$$f_m(\rho) = a_m H^{(1)}_{m+\alpha}(\rho) + b_m H^{(2)}_{m+\alpha}(\rho), \tag{5.28}$$

with complex coefficients a_m and b_m. The lower spinor component then follows from Eq. (5.27),

$$g_m(\rho) = a_m H^{(1)}_{m+\alpha+1}(\rho) + b_m H^{(2)}_{m+\alpha+1}(\rho). \tag{5.29}$$

Using the asymptotic forms of the Hankel function (5.18) the continuity relation (5.25) implies $a_m = b_m e^{2i\tilde{\delta}_m}$, i.e., the outgoing wave can differ from a free spherical wave only by a phase shift $\tilde{\delta}_m$, which depends on the magnetic perturbation and is determined in the next section. Using the Bessel function expansion formula

$$e^{i\rho\cos\phi} = \sum_m i^m e^{im\phi} J_m(\rho)$$

and the asymptotic behavior of $H_\nu^{(1,2)}$, Eq. (5.18), we find

$$b_m = \frac{i^m}{2} e^{-i\pi\alpha/2}. \tag{5.30}$$

We then obtain the scattering amplitude in terms of phase shifts as for the electrostatic case,[104]

$$F(\phi) = \frac{-i}{\sqrt{2\pi k}} \sum_m \left(e^{2i\delta_m} - 1\right) e^{im\phi}, \tag{5.31}$$

but δ_m includes the total flux α,

$$\delta_m \equiv \tilde{\delta}_m - \pi\alpha/2. \tag{5.32}$$

As a consequence, qualitatively different effects beyond the electrostatic case arise, such as the AB effect. The cross sections in Eq. (5.14) are then given by

$$\begin{aligned} \sigma_{\rm tot} &= \frac{4}{k} \sum_m \sin^2(\delta_m), \\ \sigma_{\rm tr} &= \frac{2}{k} \sum_m \sin^2(\delta_{m+1} - \delta_m). \end{aligned} \tag{5.33}$$

Scattering theory has thus been reduced to the determination of the phase shifts δ_m. In the electrostatic case,[104] the phase shifts obey the symmetry relation $\delta_m = \delta_{-m-1}$, implying the absence of backscattering, $F(\pi) = 0$. In the magnetic case under consideration here, in general this symmetry relation breaks down, and hence backscattering is not suppressed anymore, $F(\pi) \neq 0$. This is closely related to the fact that magnetic fields can confine massless Dirac particles.[47]

5.4 Ring-Shaped Magnetic Fields

In this section we consider the scattering states for a radially symmetric ring-shaped magnetic field. The scattering setup is schematically sketched in the inset of Fig. 5.1.

5.4.1 Infinitesimally thin ring

We first study the exactly solvable model of an infinitesimally thin ring of radius R around the origin, where $\Lambda_\phi(r)$ follows from Eq. (5.24) with

$$\varphi(r) = \alpha\Theta(r - R), \tag{5.34}$$

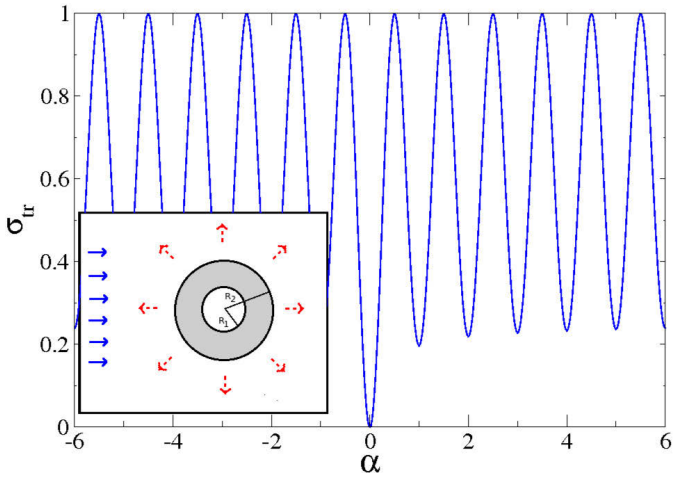

Figure 5.1: Transport cross section $\sigma_{\rm tr}$ (in units of $2/k$) vs dimensionless flux α for a finite-width magnetic ring, see Sec. 5.4.3, with $kR_1 = 0.01$ and $R_2 = 2R_1$. (We here also allow for $\alpha < 0$.) The numerical results are close to the ideal AB prediction for the infinitely thin solenoid, $\sigma_{\rm tr} = (2/k)\sin^2(\pi\alpha)$. Inset: Schematic scattering geometry. The plane wave (blue solid arrows) coming in along the $\hat{e}_x$ direction is scattered by a ring-shaped magnetic field present for $R_1 < r < R_2$ (shaded region). The outgoing spherical wave is indicated by red dashed arrows.

where Θ is the Heaviside step function and, as before, α is the dimensionless total flux through the ring surface area. For the orbital field case, this implies $B_z(r) = (\alpha\Phi_0/2\pi R)\delta(r-R)$. With $\rho = kr$ and $\mathcal{R} \equiv kR$, the solution to Eq. (5.26) is

$$f_m(\rho) = \begin{cases} a_m J_m(\rho), & \rho < \mathcal{R}, \\ b_m \left(e^{2i\tilde{\delta}_m} H^{(1)}_{m+\alpha}(\rho) + H^{(2)}_{m+\alpha}(\rho) \right), & \rho > \mathcal{R}, \end{cases} \tag{5.35}$$

with b_m in Eq. (5.30). The requirement of continuity of $\psi_m(r)$ at $r = R$, together with Eq. (5.27), leads to two boundary conditions for f_m. With $\mathcal{R}^{\pm} \equiv \mathcal{R} \pm 0^+$, they read

$$f_m\left(\mathcal{R}^+\right) = f_m\left(\mathcal{R}^-\right), \quad f'_m\left(\mathcal{R}^+\right) - f'_m\left(\mathcal{R}^-\right) = \frac{\alpha}{\mathcal{R}} f_m(\mathcal{R}), \tag{5.36}$$

where again $f' = \partial_\rho f$. The coefficient a_m and the phase shift $\tilde{\delta}_m$ appearing in Eq. (5.35) then follow from the boundary conditions (5.36).

- When $J_m(\mathcal{R}) \neq 0$, the phase shift $\tilde{\delta}_m$ can be determined by evaluation of the logarithmic derivative

$$\begin{aligned} \mathcal{L}_m &\equiv \frac{d \ln f_m(\rho = \mathcal{R}^+)}{d\rho} = \frac{\alpha}{\mathcal{R}} + \frac{J'_m(\mathcal{R})}{J_m(\mathcal{R})} \\ &= \frac{m+\alpha}{\mathcal{R}} - \frac{J_{m+1}(\mathcal{R})}{J_m(\mathcal{R})}, \end{aligned} \tag{5.37}$$

where we used the second boundary condition in Eq. (5.36). As a result, with the Neumann function Y_ν, we find

$$\tan\tilde{\delta}_m = \frac{J'_{m+\alpha}(\mathcal{R}) - \mathcal{L}_m J_{m+\alpha}(\mathcal{R})}{Y'_{m+\alpha}(\mathcal{R}) - \mathcal{L}_m Y_{m+\alpha}(\mathcal{R})}, \tag{5.38}$$

while a_m is given by

$$a_m = b_m \frac{e^{2i\tilde{\delta}_m} H^{(1)}_{m+\alpha}(\mathcal{R}) + H^{(2)}_{m+\alpha}(\mathcal{R})}{J_m(\mathcal{R})}. \tag{5.39}$$

Equation (5.38) stays valid beyond the thin-ring limit when a more general form for $\mathcal{L}_m$ is used, see Sec. 5.4.3.

- For the special case $J_m(\mathcal{R}) = 0$, Eq. (5.35) implies $e^{2i\tilde{\delta}_m} = -H^{(2)}_{m+\alpha}(\mathcal{R})/H^{(1)}_{m+\alpha}(\mathcal{R})$ and, using $f'_m(\mathcal{R}^+) = f'_m(\mathcal{R}^-)$,

$$a_m = b_m \frac{e^{2i\tilde{\delta}_m} \partial_{\mathcal{R}} H^{(1)}_{m+\alpha}(\mathcal{R}) + \partial_{\mathcal{R}} H^{(2)}_{m+\alpha}(\mathcal{R})}{J'_m(\mathcal{R})}.$$

Equations (5.38) and (5.39) include these relations when taking the limit $J_m(\mathcal{R}) \to 0$ and $\mathcal{L}_m \to \infty$.

5.4.2 Aharonov-Bohm scattering amplitude

In 1959 it was demonstrated by Aharonov and Bohm (AB)[134] that particles whose classical trajectories are confined to regions of space where no forces can act may still experience deflections because of quantum mechanical effects. The simplest example of this effect is the case of scattering of charged particles by a solenoid of infinitesimally small radius.

We can consider the $R \to 0$ limit of the above setting, which corresponds to the pure solenoid case. This allows us to study the Aharonov-Bohm (AB) effect for ultra-relativistic Dirac fermions. In order to extract the singular part, we first rewrite $f_m(r)$ in Eq. (5.28) as

$$f_m(r) = 2b_m \frac{e^{i\tilde{\delta}_m}}{\sin(\pi\alpha)} \Big[\sin(\pi\alpha - \tilde{\delta}_m)\ J_{m+\alpha}(kr) + (-)^m \sin(\tilde{\delta}_m)\ J_{-(m+\alpha)}(kr) \Big]. \tag{5.40}$$

Imposing regularity for $f_m(r)$ as $r \to 0$ requires the phase shift (5.32) to be $\delta_m = -(\pi\alpha/2)\mathrm{sgn}(m+\alpha)$.[ii] Correspondingly, for $R \to 0$, the scattering amplitude (5.31) is given by

$$F(\phi) = \frac{-i}{\sqrt{2\pi k}} \left[\left(e^{-i\pi\alpha} - 1\right) \sum_{m=-[\alpha]}^{\infty} e^{im\phi} + \left(e^{i\pi\alpha} - 1\right) \sum_{m=-\infty}^{-[\alpha]-1} e^{im\phi} \right], \tag{5.41}$$

[ii] As $J_{-\nu}(r)$ with $\nu > 0$ is not well behaved at $r = 0$

where $\alpha = [\alpha] + \{\alpha\}$, with integer part $[\alpha]$ and non-integer part $0 \leq \{\alpha\} < 1$. Summation of the series in Eq. (5.41) yields[136]

$$F(\phi) = \frac{-i}{\sqrt{2\pi k}}\Big(2\pi\delta(\phi)[\cos(\pi\alpha) - 1] + e^{-i([\alpha]+1/2)\phi}\frac{\sin(\pi\alpha)}{\sin(\phi/2)}\Big). \tag{5.42}$$

Up to the forward scattering ($\phi = 0$) amplitude, Eq. (5.42) reproduces the AB result,[134,135,137] here obtained in terms of scattering phase shifts. Note that the forward scattering δ-term, missing in the AB calculation,[134] naturally appears in our phase shift analysis and is essential for establishing unitarity of the scattering matrix.[136,141]

In alternative approaches to obtain $F(\phi)$ for the ideal solenoid, following the original AB method,[134] the asymptotics of the exact wavefunction is computed from its integral representation. As a result, the incident wave corresponding to Eq. (5.15) has an additional phase factor $e^{-i\pi\alpha\ \mathrm{sgn}(\sin\phi)}e^{-i\alpha\phi}$, i.e., one has a multi-valued incoming plane wave. The precise relation between these two approaches has been discussed in several works and is still under debate,[136–141] albeit the difference is of little relevance to experimentally observable quantities. In particular, the transport cross section σ_{tr} in Eq. (5.14) does not depend on the forward scattering amplitude at all. We conclude that our approach is able to reproduce the AB effect, $\sigma_{\mathrm{tr}} = (2/k)\sin^2(\pi\alpha)$, with oscillations as function of the dimensionless flux parameter α. In particular, $\sigma_{\mathrm{tr}} = 0$ for integer α.

5.4.3 Magnetic ring of finite width

We now generalize the setup to a finite width, with $R_1 < R_2$ denoting the inner and outer radii of the ring, cf. the inset of Fig. 5.1. Again, $\Lambda_\phi(r)$ in Eq. (5.24) is expressed in terms of a dimensionless flux function $\varphi(r)$. When Λ_ϕ is a vector potential, the associated magnetic field $B_z(r) = B$ is taken uniform within the ring region and zero outside; for concreteness, we take $B \geq 0$. This profile allows for an exact solution, while more general smooth field profiles can be treated within the Wentzel-Kramers-Brillouin (WKB) approximation, see Sec. 5.4.4.

We use dimensionless coordinates ($\rho = kr$ and $\mathcal{R}_{1,2} = kR_{1,2}$) and flux parameters,

$$\nu_{1,2} = \frac{\pi B R_{1,2}^2}{\Phi_0}, \quad \nu \equiv \frac{\nu_1}{\mathcal{R}_1^2} = \frac{\nu_2}{\mathcal{R}_2^2}, \quad \alpha = \nu_2 - \nu_1. \tag{5.43}$$

The function φ then reads with $r = \rho/k$:

$$\varphi(r) = \begin{cases} 0, & \rho < \mathcal{R}_1, \\ \nu\rho^2 - \nu_1, & \mathcal{R}_1 < \rho < \mathcal{R}_2, \\ \alpha, & \rho > \mathcal{R}_2. \end{cases} \tag{5.44}$$

For $R_1 \to R_2$, this reduces to Eq. (5.34). In particular, α in Eq. (5.44) again denotes the total dimensionless flux.

For given $j = m + 1/2$, the components of the Dirac spinor ψ_m obey Eqs. (5.26) and (5.27), with Eq. (5.44) now determining $W_m(\rho)$. The solutions for $r < R_1$ and $r > R_2$

are as in Eq. (5.35),

$$f_m(\rho) = \begin{cases} a_m J_m(\rho), & \rho < \mathcal{R}_1, \\ b_m \left(e^{2i\tilde{\delta}_m} H^{(1)}_{m+\alpha}(\rho) + H^{(2)}_{m+\alpha}(\rho) \right), & \rho > \mathcal{R}_2, \end{cases} \tag{5.45}$$

where a_m and $\tilde{\delta}_m$ are to be determined, and b_m is given in Eq. (5.30). For $R_1 < r < R_2$, Eq. (5.26) can be solved in terms of the confluent hypergeometric functions Φ and Ψ,[149]

$$\begin{aligned} f_m(\rho) &= \rho^{|\tilde{m}|} e^{-\nu\rho^2/2} \Big[c_m \Phi(\xi_m, 1+|\tilde{m}|; \nu\rho^2) \\ &+ d_m \Psi(\xi_m, 1+|\tilde{m}|; \nu\rho^2) \Big], \\ \xi_m &\equiv 1 + \tilde{m}\Theta(\tilde{m}) - 1/4\nu, \quad \tilde{m} \equiv m - \nu_1. \end{aligned} \tag{5.46}$$

The coefficients c_m and d_m, together with a_m and the phase shift $\tilde{\delta}_m$ in Eq. (5.45), follow by matching ψ_m at $r = R_{i=1,2}$. Taking into account that W_m is a continuous function of ρ, we have

$$f_m\left(\mathcal{R}_i^+\right) = f_m\left(\mathcal{R}_i^-\right), \quad f'_m\left(\mathcal{R}_i^+\right) = f'_m\left(\mathcal{R}_i^-\right), \tag{5.47}$$

where the second condition follows by continuity of the lower spinor component g_m.

It is convenient to introduce the transfer matrix $\hat{\mathcal{T}}_m$ connecting the solutions at $\rho = \mathcal{R}_1^+$ and $\mathcal{R}_2^-$,

$$\begin{pmatrix} f_m(\mathcal{R}_2^-) \\ f'_m(\mathcal{R}_2^-) \end{pmatrix} = \hat{\mathcal{T}}_m \begin{pmatrix} f_m(\mathcal{R}_1^+) \\ f'_m(\mathcal{R}_1^+) \end{pmatrix} = a_m \hat{\mathcal{T}}_m \begin{pmatrix} J_m(\mathcal{R}_1) \\ J'_m(\mathcal{R}_1) \end{pmatrix}. \tag{5.48}$$

Explicitly, the transfer matrix for the magnetic ring of finite width is

$$\hat{\mathcal{T}}_m = \begin{pmatrix} \Phi_2 & \Psi_2 \\ \Phi'_2 & \Psi'_2 \end{pmatrix} \begin{pmatrix} \Phi_1 & \Psi_1 \\ \Phi'_1 & \Psi'_1 \end{pmatrix}^{-1}, \tag{5.49}$$

where we use the abbreviation

$$\Phi_{i=1,2} \equiv \mathcal{R}_i^{|\tilde{m}|} e^{-\nu_i/2} \Phi(\xi_m, 1+|\tilde{m}|; \nu_i),$$

and similarly for Ψ_i. We mention in passing that for the infinitesimally thin magnetic ring in Sec. 5.4.1 (where $R_1 = R_2 = R$), the transfer matrix is $\hat{\mathcal{T}}_m = \begin{pmatrix} 1 & 0 \\ \alpha/\mathcal{R} & 1 \end{pmatrix}$.

For the finite-width ring, using Eq. (5.45) the phase shift $\tilde{\delta}_m$ is then again given by Eq. (5.38), with $\mathcal{R} \to \mathcal{R}_2$ and the logarithmic derivative $\mathcal{L}_m$ replaced by

$$\mathcal{L}_m = \frac{u_{m,2}}{u_{m,1}}, \quad \begin{pmatrix} u_{m,1} \\ u_{m,2} \end{pmatrix} = \hat{\mathcal{T}}_m \begin{pmatrix} J_m(\mathcal{R}_1) \\ J'_m(\mathcal{R}_1) \end{pmatrix}. \tag{5.50}$$

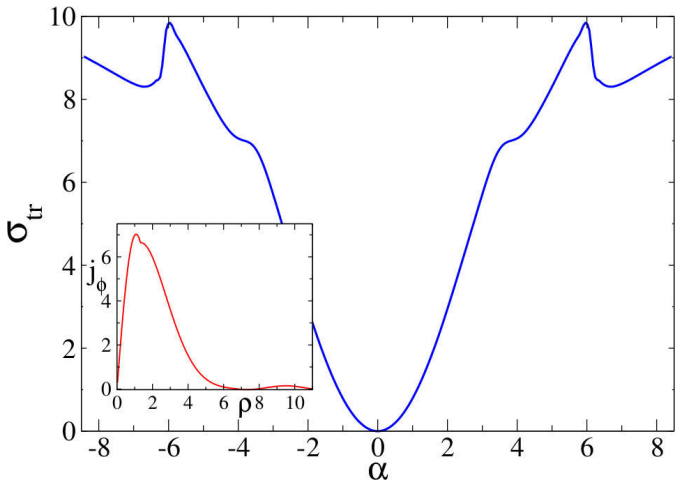

Figure 5.2: The main panel is as in Fig. 5.1 but for $kR_1 = 1.32$ and $R_2 = 5R_1$. Inset: Current density $j_\phi(\rho) = \hat{e}_\phi \cdot \boldsymbol{j}$ vs radial coordinate ρ for the quasi-bound state with $j = 3/2$ present at $\alpha \simeq 6$.

With the above expressions, it is straightforward to compute the scattering phases $\delta_m = \tilde{\delta}_m - \pi\alpha/2$ numerically for the finite-width ring geometry. Thereby we obtain[iii] the scattering amplitude $F(\phi)$ from Eq. (5.31) and the transport cross section $\sigma_{\rm tr}$ from Eq. (5.33).

Numerical results obtained under this approach are shown in Figs. 5.1 and 5.2. First, in the main panel of Fig. 5.1, we show the transport cross section $\sigma_{\rm tr}$ as a function of the total flux α. In this example, both radii R_1 and R_2 were chosen very small, such that scattering by the ring is close to the one by an ideal AB solenoid. As a consequence, we observe the AB oscillations with unit flux period. In contrast to the ideal AB result, a complete suppression of scattering for $\alpha \in \mathbb{Z}$ is observed in the finite-width ring only for $\alpha = 0$, while the maximum value $\sigma_{\rm tr} = 2/k$ for half-integer α is still perfectly realized. In fact, the phase shift analysis in Sec. 5.4.2 shows that a given oscillation period is determined by one specific m value in the ideal AB case. For the non-ideal finite-width ring, other total angular momenta also start to contribute, and this mixing effect destroy the perfect constructive interference needed for $\sigma_{\rm tr} = 0$. On the other hand, the destructive interference responsible for the maxima of $\sigma_{\rm tr}$ at half-integer α is more robust since it is dominated by a single m value.

In Fig. 5.2, we study scattering by a much larger ring. In this case, the AB effect is absent, which can be understood by noting that the Fermi wavelength $(2\pi/k)$ of the particle is now smaller than the outer circumference $2\pi R_2$ of the ring. Quantum interference of waves surrounding the obstacle in opposite directions is then largely averaged out, and, moreover, the wavefunction can partially penetrate into the ring area.

[iii] In the numerical evaluation, we sum over all angular momentum states $|j| < 40$ (with $j = m + 1/2$). Scattering phases with very large $|j|$ are difficult to compute reliably yet average out in practice.

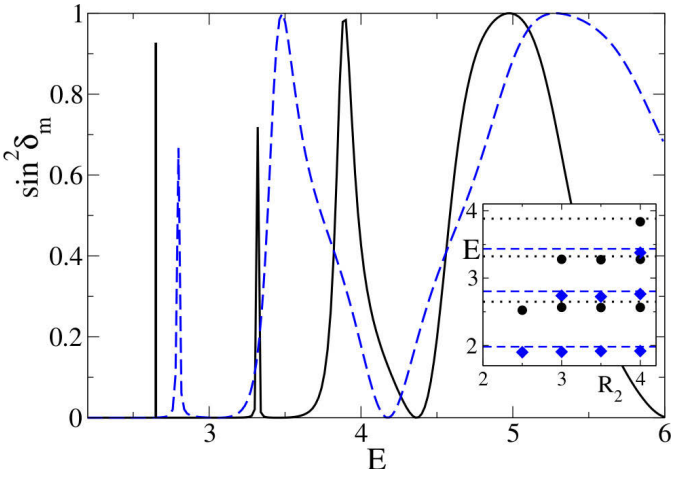

Figure 5.3: Partial cross section $\sin^2\delta_m$ vs energy E for a ring-shaped confinement as in Sec. 5.4.3. The numerical results are for total angular momentum states with $m = 1$ (solid black) and $m = -1$ (dashed blue curve). The radii are $R_2 = 7R_1$ and $R_1 = 0.5\ell_B$ with $\ell_B = \sqrt{2c/eB}$, and energies are in units of $\hbar v_F/\ell_B$. Inset: WKB results for quasi-bound state energies E_r vs R_2 (lengths in units of ℓ_B), for $m = 1$ (black circles) and $m = -1$ (blue diamonds) with fixed $R_1 = 0.5\ell_B$. For comparison, the exact levels for infinite R_2 from Ref. 48 are shown for $m = 1$ (dotted black) and $m = -1$ (dashed blue curve).

However, a remarkable peak feature at $\alpha \approx 6$ appears now in the transport cross section, see Fig. 5.2. This feature can be traced to the appearance of a quasi-bound state with $j = 3/2$ at this flux value (for the considered energy), which then causes a scattering resonance, cf. our discussion in Sec. 5.4.4. The inset of Fig. 5.2 shows the current density profile for precisely this quasi-bound state. While the radial component vanishes, $j_r = 0$, we find a circularly oriented current, $j_\phi \neq 0$, which is mainly localized inside the ring ($r < R_1$) and represents a current-carrying bound state. We note that more quasi-bound states appear for larger α, causing additional peak features in $\sigma_{\rm tr}(\alpha)$ beyond those shown in Fig. 5.2.

5.4.4 Quasi bound state and scattering resonances

The magnetic confinement built up by the ring-shaped field can generate quasi-bound states, which for $R_2 \to \infty$ become true bound states.[47,48] The quasi-bound state spectrum then causes resonances in the scattering amplitude when the energy $E = \hbar v_F k$ is varied. For given total angular momentum $j = m+1/2$, the corresponding phase shift $\delta_m(E)$ goes through the value $\pi/2$ as E crosses a resonance level E_r. The corresponding resonance width Γ_r can be estimated from[148]

$$(d/dE)\cot\left[\delta_m(E = E_r)\right] = -2/\Gamma_r.$$

To access these resonances, we first put Eq. (5.26) into a canonical form with separated kinetic and potential energy terms. The substitution $f_m(\rho) = \rho^{-1/2}\tilde{f}_m(\rho)$ yields

$$\left[-\partial_\rho^2 + V_m(\rho)\right]\tilde{f}_m = \tilde{f}_m, \quad V_m \equiv W_m^2 + W_m', \tag{5.51}$$

where $V_m(\rho)$ is an effective potential energy for the radial motion and the lower spinor component is $g_m = \rho^{-1/2}(-\partial_\rho + W_m)\tilde{f}_m$.

In this form, Eq. (5.51) can be treated within the standard WKB approach, which represents an attractive alternative to semiclassical approaches to the Dirac equation as it avoids the appearance of non-Abelian Berry phases.[131,150,151] For a magnetic ring as in Sec. 5.4.3, the effective potential V_m has a hard repulsive core for $r \to 0$ plus a barrier at larger distances, i.e., a quantum well is formed with classically allowed motion for $r_0 < r < r_1$. The "turning points" $r_{0,1}$ here depend on the energy $E = \hbar v_F k$ under consideration. For finite R_2, this barrier is of finite width and quasi-bound states within the well region may exist. The classically forbidden region $r_1 < r < r_2$ (where r_2 is another turning point) then corresponds to tunneling trajectories where the "particle" escapes from the well region. For $R_2 \to \infty$, the barrier becomes infinitely wide and this escape probability vanishes, i.e., we obtain true bound states in the well region. Using the radial variable $r = \rho/k$, Eq. (5.51) reads

$$\begin{aligned} &\left[-\partial_r^2 + U_m(r)\right]\tilde{f}_m(r) = \epsilon\tilde{f}_m(r), \\ &U_m(r) = w_m^2 + \partial_r w_m, \quad w_m(r) = kW_m(kr), \end{aligned} \tag{5.52}$$

where the modified Bohr-Sommerfeld quantization condition for the *complex-valued "energy"* $\epsilon \equiv k^2$ is[152]

$$\begin{aligned} &\int_{r_0}^{r_1} dr\ \sqrt{\epsilon - U_m(r)} = \pi\left(n + \frac{1}{2} - \frac{\chi(a)}{2\pi}\right), \\ &\chi(a) = \frac{1}{2i}\ln\left(\frac{\Gamma(ia+1/2)}{\Gamma(-ia+1/2)\left[1+e^{-2\pi a}\right]}\right) \\ &\qquad + a(1-\ln a), \\ &a = \frac{1}{\pi}\int_{r_1}^{r_2} dr\ \sqrt{U_m(r) - \epsilon}, \end{aligned} \tag{5.53}$$

with $n = 0, 1, 2, \ldots$ and the Gamma function $\Gamma(z)$. The complex resonance values for ϵ solving Eq. (5.53) can be found numerically. Equation (5.53) is formally exact for the case of a parabolic barrier, but also applies for an arbitrary smooth potential and is expected to remain accurate[152] even for small n. We now write

$$\epsilon = (k - i\gamma/2)^2 \approx k^2 - ik\gamma.$$

For a quasi-bound level with energy $E_r = \hbar v_F k$, the resonance width is then $\Gamma_r = \hbar v_F \gamma$. Using $\mathrm{Im}\chi(a) \approx e^{-2\pi a}/2$ for $a \gtrsim 1$, we obtain

$$\Gamma_r/\hbar = T_k^{-1} e^{-2\pi a}, \tag{5.54}$$

where the period of radial motion is

$$T_k = \frac{2k}{v_F} \int_{r_0}^{r_1} \frac{dr}{\sqrt{k^2 - U_m(r)}}.$$

Our numerical results for the partial cross section, $\sin^2 \delta_m$, as a function of energy, and the WKB results for the corresponding quasi-bound state energies E_r are shown in Fig. 5.3. Here we take the field profile as in Sec. 5.4.3.[iv] With increasing R_2 (keeping R_1 fixed), new quasi-bound energy levels localized in the well region appear, see inset of Fig. 5.3. Very good agreement with exact quantum calculations[48] for the infinite barrier case ($R_2 \to \infty$) is observed, i.e., these energy levels remain basically unchanged when increasing R_2. The only noticeable deviation from the exact spectrum of Ref. 47 is seen for $m = 0$, where the potential $U_{m=0}(r)$ creates an infinitely attractive well for $r \to 0$. In that case, the WKB approximation becomes questionable in that "steep" region. The main panel in Fig. 5.3 illustrates the sequence of quasi-bound states present because of the magnetic confinement. The corresponding scattering resonances appear as peaks in the transport cross section $\sigma_{\rm tr}$ when varying energy or the effective flux parameter α.

5.5 Summary & Discussion

In this chapter we have studied scattering of massless two-dimensional Dirac fermions by magnetic perturbations of various types. The model is applicable to quantum transport in monolayer graphene and for the surface state of strong topological insulators. The magnetic fields can correspond to orbital or Zeeman fields, strain-induced fields in graphene, or exchange fields generated by ferromagnets.

The full scattering solution was discussed in detail for radially symmetric perturbations, where the scattering amplitude can be expressed in terms of phase shifts in a given total angular momentum channel, and within the Born approximation for the general case. Our approach now allows for a systematic study of the scattering of Dirac fermions on magnetostatic perturbations.

As applications, we have studied scattering by magnetic impurities within the Born approximation, and fully nonperturbative scattering for the case of ring-shaped magnetic fields. The Born approximation is only valid when the perturbation has zero total flux ($\alpha = 0$). For the ring-shaped field case, as one increases the lateral size (R_2) of the magnetic perturbation, we have a crossover from the Aharonov-Bohm case to a regime dominated by scattering resonances. In the first case, $R_2 \to 0$, particle trajectories surround the flux region but essentially do not penetrate it, leading to the oscillatory transport cross section $\sigma_{\rm tr} \propto \sin^2(\pi\alpha)$. In the second case, where the particle wavelength is small against the size of the perturbation, $kR_2 > 1$, the AB oscillations in $\sigma_{\rm tr}(\alpha)$ are absent. However, now quasi-bound states arise due to the magnetic confinement, causing scattering resonances which show up as peaks in $\sigma_{\rm tr}(\alpha)$.

[iv] In order to avoid artefacts caused by treating sharp boundaries within the WKB approach, we have used a smoothening of the field steps.

Chapter 6

Electronic Transport Through Hybrid Structures in Graphene

6.1 Introduction

The existence of Dirac-like quasi-particles in graphene (discussed in Sec. 1.3.2) has motivated a lot of research work in exploring also the effects due to the proximity of a superconductor. Graphene is not a natural superconductor by itself. However superconductivity in a graphene layer can be induced in the presence of a superconducting electrode near it via the proximity effect. Then one can form various hybrid structures with normal graphene and superconductor junctions. If graphene is confined between two superconducting barrier, due to the formation of bound states, various resonance effects are observed in transport.

In this chapter, in the first section we discuss some phenomenon associated with proximity effects. Then in section 2 and 3 we discuss the resonant tunneling in a superconducting double barrier (SDB) structure in graphene and its consequences in quantum charge pumping.

6.2 Superconducting Proximity and Andreev Reflection

The **proximity effect**[153] is the occurrence of superconducting-like properties in non-superconducting materials placed in electrical contact with a superconductor (S). It has been understood that superconducting correlation could extend over a large length scale in a normal metal (N), even in the absence of attractive electron-electron interactions.[154–156] The actual energy gap in the metal is determined not by a pairing interaction as in a BCS superconductor but by the diffusion of single quasi-particles in the normal metal, which is a result of the remote interaction felt by the electronic state when entering the metal. The role of the Andreev reflection (described below) is central to the proximity effect since it provides the elementary mechanism for converting single electron states from a normal metal to Cooper pairs in the superconducting condensate. The actual proximity effect is the result of an interplay between Andreev reflection at the normal metal - superconductor (NS) interface and long-range coherence in the normal metal.

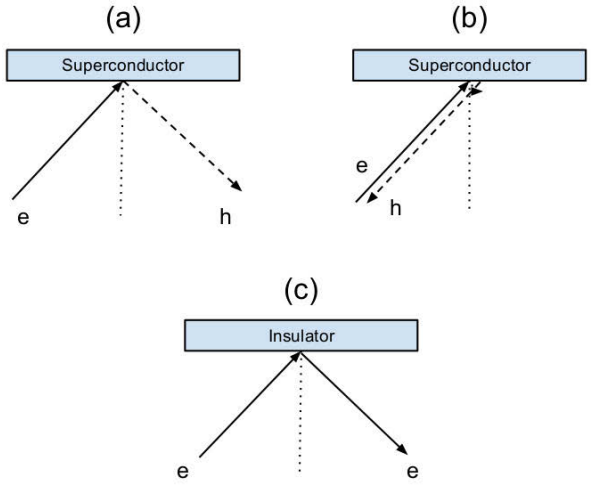

Figure 6.1: (a) Specular Andree reflection, (b) retro Andreev reflection, (c) normal reflection. Specular AR appears in the case of graphene and is discussed in Sec. 6.2.3.

At the interface of a normal metal and superconductor , because of the existence of an energy gap at the Fermi energy in the density of states of the superconductor, the transfer of single electron from the normal metal with an energy ϵ below the gap Δ is forbidden[i]. However, an incoming electron can be transferred into the superconductor if a second electron is also transferred through the interface thus forming a Cooper pair into the superconductor. In terms of single excitations, this process is equivalent to the reflection of a hole. This process conserves energy but a net $2e$ charge is transfered to the superconductor and is called the "**Andreev reflection**" (AR) process.[157]

As the low energy electron transport in graphene is governed by Dirac equation, the Andreev reflection in graphene is fundamentally different from normal metals.[158,159] While in case of metal, the hole is reflected back along the path of the incident electron (retro-reflection), the Andreev reflection can be both retro and specular in case of graphene. Fig. 6.1(a) and (b) shows the two type of AR. Here we give a brief description of Andreev reflection process in both cases:

6.2.1 Andreev reflection process

Andreev reflection process can be understood from the interaction term (or, pairing term) of the mean-field BCS Hamiltonian, which is known as Bogoliubov – de Gennes (BdG)

[i] discussed in Appendix F, Eq. (F.6)

Hamiltonian (Appendix F). The pairing term has the following form:

$$H_p(\mathbf{k}) = \left(\bar{\Delta} c_{-\mathbf{k}\downarrow} c_{\mathbf{k}\uparrow} + \Delta c^{\dagger}_{\mathbf{k}\uparrow} c^{\dagger}_{-\mathbf{k}\downarrow}\right). \tag{6.1}$$

The interaction can be interpreted in two ways: we can regard $\bar{\Delta} c_{-\mathbf{k}\downarrow}$ as a term that converts two particles into a condensed pair (cooper pair);

$$e^- + e^- \rightleftharpoons \text{Cooper Pair}^{-2} \ . \tag{6.2}$$

Alternatively, by writing $c_{-\mathbf{k}\downarrow} = h^{\dagger}_{\mathbf{k}\uparrow}$ as a hole creation operator, $H_p(\mathbf{k}) = \bar{\Delta} h^{\dagger}_{\mathbf{k}\uparrow} c_{\mathbf{k}\uparrow} + \text{H.C.}$ describes the scattering of an electron into a condensed pair (represented by $\bar{\Delta}$) and a hole, which is an "Andreev reflection" process:

$$e^- \rightleftharpoons \text{Cooper Pair}^{-2} + h^+ \ . \tag{6.3}$$

Andreev reflection "reflects" electrons into holes, reversing their charge and velocity, yet it conserves spin and momentum. Because, for a hole in the state $(-\mathbf{k}\downarrow)$ has spin up, momentum $+\mathbf{k}$. So, this process for normal metal is a *retro* reflection process.

Amplitude of Andreev reflection:

In the presence of superconductivity, an excitation in a metal is conveniently represented by a two-component wave function, the components describing electrons ($\psi_e(\vec{r})$) and holes ($\psi_h(\vec{r})$). The wave function obeys the Bogoliubov – de Gennes (BdG) equation, which is the equivalent of schrödinger equation for BCS superconductor:

$$\begin{pmatrix} \hat{H} & e^{i\phi}\Delta \\ e^{-i\phi}\Delta^* & -\hat{H}^* \end{pmatrix} \begin{pmatrix} \psi_e(\vec{r}) \\ \psi_h(\vec{r}) \end{pmatrix} = \epsilon \begin{pmatrix} \psi_e(\vec{r}) \\ \psi_h(\vec{r}) \end{pmatrix}, \tag{6.4}$$

where the energy is counted from the Fermi level, so that $\hat{H} = H - E_F$, $H = -(\hbar^2/2m)(\nabla + ieA(r)/\hbar c)^2 + U(r)$ being the Hamiltonian for electrons in the absence of any superconductors. The superconducting gap Δ and phase ϕ are position-dependent and vanish in the normal part of the nanostructure. It is enough for our purposes to assume that Δ and ϕ are constant in the superconducting region.

For a plane wave solution $\propto \exp(ikr)$ for the BdG equation (6.4), we have

$$\hbar k = \sqrt{2m(E_F \pm \sqrt{(\epsilon^2 - \Delta^2)})}. \tag{6.5}$$

In the normal metal ($\Delta = 0$), for $\epsilon \ll E_F$, we have from Eq. (6.5), $k = k_F \pm \epsilon/\hbar v_F$. where the $\pm$ stands for electron and hole propagation. For the case of superconducting region, the corresponding condition is $k = k_F \pm \sqrt{\epsilon^2 - \Delta^2}$.

Let us consider an ideal (no scattering) contact between a normal metal (region N) ($x < 0$) and a superconductor (region S) ($x > 0$). For solving this 1D problem, we consider the soution in the normal metal of the form:

$$\psi_N(x<0) = \begin{pmatrix} 1 \\ 0 \end{pmatrix} e^{ix\epsilon/\hbar v_F} + r_A \begin{pmatrix} 0 \\ 1 \end{pmatrix} e^{-ix\epsilon/\hbar v_F} \ . \tag{6.6}$$

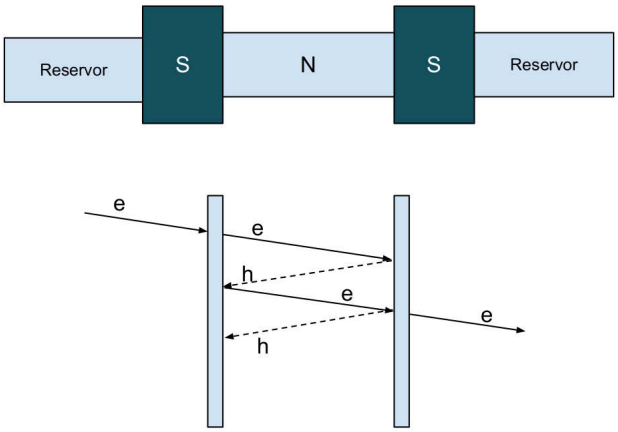

Figure 6.2: Formation of Andreev bound state by multiple Andreev reflection and resonant tunneling

In the superconducting region, in case of $\epsilon < \Delta$, the convergent wavefunction is taken as:

$$\psi_S(x > 0) = \begin{pmatrix} u \\ v \end{pmatrix} e^{-x\sqrt{\Delta^2-\epsilon^2}/\hbar v_F} \ . \tag{6.7}$$

Matching them at the interface ($x = 0$), we get the amplitude of Andreev reflection

$$r_A = e^{-i\cos^{-1}\left(\frac{\epsilon}{\Delta}\right)-i\phi} \ . \tag{6.8}$$

So, as expected, in this case, with $\epsilon < \Delta$, the electron is totally Andreev reflected ($|r_A|^2 = 1$).

For the case of $\epsilon > \Delta$, the amplitude of Andreev reflection is:

$$r_A = e^{-i\phi}\left(\frac{\epsilon}{\Delta} - \frac{\sqrt{\epsilon^2-\Delta^2}}{\Delta}\right) \ , \tag{6.9}$$

so, $|r_A|^2 < 1$ and it decreases with increasing incident energy.

6.2.2 Resonant tunneling and Andreev bound state

Lets consider an one dimensional system consisting of a normal metal (N) separating two superconducting barrier (S) of finite width, as depicted in Fig. 6.2. Let us now consider an electron in N region at sufficiently low energy. It will experience Andreev reflections trying to get to either superconductor. The resulting hole experiences the same problem: it cannot escape the nanostructure and is converted back to an electron in the course of the escape attempt. This bound motion will give rise to bound states with discrete energy levels.

This bound states can affect the Andreev reflection amplitude of the whole system and gives rise to tunneling resonances. For an incident electron from the left side to the first barrier with an energy ϵ, the total tunneling amplitude is calculated by summing up all possible paths (because of multiple reflection) as:[160]

$$\begin{aligned} T &= t_{ee}^{(1)} P_e \left(1 + r_{he}^{(2)} P_h r_{eh}^{(1)} P_e + \cdots\right) t_{ee}^{(2)} \\ &= t_{ee}^{(1)} P_e \left(\frac{1}{1 - r_{he}^{(2)} P_h r_{eh}^{(1)} P_e}\right) t_{ee}^{(2)}, \end{aligned} \tag{6.10}$$

where $t^{(i)}$ is the tunneling amplitudes of electron through barrier $i = 1, 2$, $r_{eh}^{(i)}$ ($r_{eh}^{(i)}$) is the Andreev reflection amplitude at barrier i for hole (electron) to reflect as electron (hole). P_e and P_h are respectively the phase acquired by the right moving electron and left moving hole while traveling by a path L in the N region: (from Eq. (6.5))

$$P_{e/h} = e^{\pm i\sqrt{2m(E_F \pm \epsilon)}}. \tag{6.11}$$

The transmission resonance occurs when the denominator of T in Eq. (6.10) vanishes. This will give the equation for determining energies the quasi bound-state in the system.

6.2.3 BDG equation & Andreev reflection in graphene:

Let us consider a graphene sheet in the xy plane. A superconducting electrode covers the region $x > 0$, while the region $x < 0$ is in the normal graphene (non-superconducting) state. The excitations (electron, hole) are described by the generalized Bogoliubov-De Gennes equation:[158]

$$\begin{pmatrix} (H - E_F) & e^{i\phi}\Delta \\ e^{-i\phi}\Delta^* & -(THT^{-1} - E_F) \end{pmatrix} \begin{pmatrix} \psi_e(\vec{r}) \\ \psi_h(\vec{r}) \end{pmatrix} = \epsilon \begin{pmatrix} \psi_e(\vec{r}) \\ \psi_h(\vec{r}) \end{pmatrix}, \tag{6.12}$$

where H the single-particle Hamiltonian in graphene, and T the time-reversal operator. The single-particle Hamiltonian we discussed in Sec. 1.3.3 (Eq. (1.33)),

$$H = \begin{pmatrix} H_+ & 0 \\ 0 & H_- \end{pmatrix}, \tag{6.13}$$

$$H_\pm = -i\hbar v_F(\sigma_x \partial_x \pm \sigma_y \partial_y) + U, \tag{6.14}$$

which acts on a four-dimensional spinor $(\Psi_{A+}, \Psi_{B+}, \Psi_{A-}, \Psi_{B-})$. The indices A, B label the two sublattices of the honeycomb lattice of carbon atoms, while the indices $\pm$ label the two valleys of the band structure. The Pauli matrices σ_i act on the sublattice index. The time-reversal operator interchanges the valleys and in the absence of a magnetic field, the Hamiltonian is time-reversal invariant, $THT^{-1} = H$. Substituting this in Eq. (6.12) we obtain two decoupled sets of four equations each, of the form

$$\begin{pmatrix} (H_\pm - E_F) & e^{i\phi}\Delta \\ e^{-i\phi}\Delta^* & -(H_\pm - E_F) \end{pmatrix} \begin{pmatrix} \psi_e(\vec{r}) \\ \psi_h(\vec{r}) \end{pmatrix} = \epsilon \begin{pmatrix} \psi_e(\vec{r}) \\ \psi_h(\vec{r}) \end{pmatrix}, \tag{6.15}$$

Because of the valley degeneracy it suffices to consider one of these two sets. For simplicity we can take H_+, the Eq. (6.15) leads to a four-dimensional Dirac-Bogoliubov-De Gennes (DBDG) equation. The solution of this equation is discussed in Appendix G, where we see that for an incident electron of energy ϵ with an y momentum (parallel to the interface) k_y and an angle of incidence α, the reflected hole has an angle of reflection α', where

$$\alpha = \sin^{-1}[\hbar v_F k_y/(\epsilon + E_F)] \ , \quad \alpha' = \sin^{-1}[\hbar v_F k_y/(\epsilon - E_F)] \ , \tag{6.16}$$

E_F is the Fermi energy. Now, if $\epsilon < E_F$, the reflected hole is an empty state in the conduction band and if $\epsilon > E_F$, hole is an empty state in the valence band. A conduction-band hole moves opposite to its wave vector, so we see that α and α' are of opposite sign (retro-reflection). A valence-band hole, in contrast, moves in the same direction as its wave vector, so α and α' are of same sign (specular reflection). The physical reason of the specular AR is the same as Klein tunneling (Sec. 1.3.4), that because of the Dirac spectrum, an electron can Andreev reflected both as a conduction band hole or a valence band hole.

The presence of the SAR process in graphene may lead to qualitatively different behavior in many transport phenomena. But, in our considered geometry, as we will concentrate on resonant tunneling, we will mostly stay in the retro-reflection regime (we discuss the effect of SAR in Sec. 6.3.3). Also, experimentally it is difficult to reach the specular reflection regime.[158]

6.2.4 Crossed Andreev reflection (CAR)

An even more intriguing example where the proximity effect manifests itself is the phenomenon of crossed Andreev reflection (CAR) which can take place in a normal metal-superconductor-normal metal (NSN) junction, provided the distance between the two normal metals is less than or equal to the phase coherence length of the superconductor. This is a nonlocal process where an incident electron from one of the normal leads pairs up with an electron from the other lead to form a Cooper pair and jumps into the superconductor. CAR occurs in competition with elastic co-tunneling or EC, the quantum mechanical tunneling of electrons between the normal leads via an intermediate state in the superconductor.

Due to the presence of the Dirac-like energy spectrum, like specular Andreev Reflection (SAR), graphene can also exhibit specular crossed Andreev reflection (SCAR) in a proximity induced graphene NSN junction. The effect of CAR in graphene has been studied earlier in[161,162] in the context of detecting entangled states in graphene. However, transport properties of a superconducting double barrier (SDB) geometry in graphene, i.e. graphene NSNSN junctions, was not studied so far, where resonance effects can be more important.

6.3 Resonant Tunneling through Superconducting Double Barrier in Graphene

In general, electronic confinement in graphene is experimentally challenging due to the effect of Klein tunneling (Sec. 1.3.4). In the recent past, resonant tunneling has been considered in doped graphene (single barrier) $n-p-n$ junctions[46] and in normal

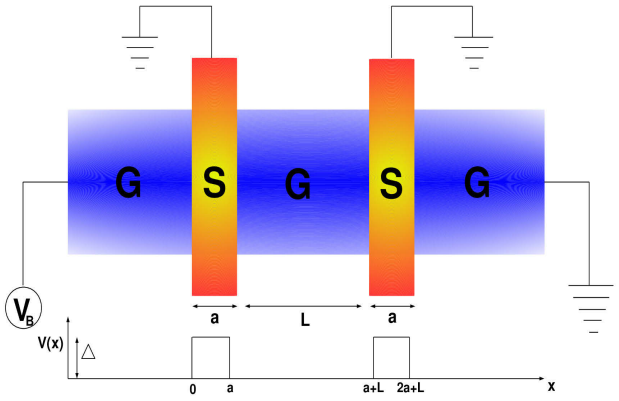

Figure 6.3: Cartoon of the SDB structure in a graphene sheet. Two patches at the two places on the graphene sheet depict superconducting material deposited on top of it. The schematic of the potential profile seen by an incident electron is shown below.

double barrier structures[163,164] where resonance effects on the transmission have been investigated. But here again, the problem of resonant transmission through doped double barriers in graphene has not been investigated. Motivated by this, we studied resonant tunneling through a superconducting double barrier (SDB) structure in graphene, which, because of the correspondence between AR and Klein tunneling[165] would also be valid for a doped graphene $n-p-n-p-n$ junction.

In our analysis, we consider a clean graphene sheet in the x-y plane. The SDB structure is formed by depositing thin strips of superconducting material on top of the graphene sheet at two places. This induces a finite superconducting gap ($\Delta_i e^{i\phi_i}$) in the barrier regions as a result of the proximity effect of the superconducting patches. Here Δ_i and ϕ_i are the pair potentials and order parameter phases on the two patches respectively (i refers to the index of the strips). The geometry is shown in Fig. 6.3. The space dependence of the order parameter can be expressed as

$$V(x) = \Delta e^{i\phi}\Theta(x)\Theta(-x+a) + \Delta e^{i\phi}\Theta(x-a-L)\Theta(2a+L-x)\ , \tag{6.17}$$

where a is the width of the superconducting barrier in graphene and L is the distance between the two barriers. Here we assume that the spatial variation of potential steps is slow on the scale of the lattice spacing so that inter-valley scattering is suppressed. Also here Θ is the Heaviside Θ-function, and we have taken $\phi_1 = \phi_2 = \phi$, since we will not be looking at supercurrents (Josephson effect).

Processes

As discussed before in section 6.2, if the width a of the superconducting strips is of the order of the phase coherence length of the superconductors, the normally incident electron can be transmitted across the barriers both as an electron (electron co-tunneling (CT))

and as a hole, via the retro crossed Andreev reflection (CAR) process and specular crossed Andreev reflection (SCAR). And the electron can be reflected back by retro Andreev reflection (AR) and specular Andreev reflection (SAR). Here, we restrict ourselves to spin singlet (s-wave) superconductors so that the electron and the hole are taken from opposite spin bands in order to allow the Cooper pair to jump into the superconductor with net spin zero.

Our aim now is to obtain the net quantum mechanical amplitudes for reflection, transmission, AR (and SAR) and CAR (and SCAR) of an electron incident on the SDB structure, after it has traversed both the barriers. A double barrier structure can always lead to resonances and this can affect the transmissions and the reflections through the system. For non-relativistic electrons, this scenario has been studied before.[160,166] For relativistic electrons, the standard paradigm is that one cannot obtain confined carrier states for normal incidence[40,158] due to Klein tunneling. However, discrete energy levels can be found for carriers in graphene based quantum wires, as long as they have a non-zero component parallel to the barrier.[163] Moreover, for normal incidence, discrete Andreev bound levels are also found between two superconductors in graphene.[167,168]These levels can clearly lead to resonant transmissions in a SDB structure in graphene.

6.3.1 Scattering matrix for single barrier:

For an initial state Ψ_{in} of incident particle on a superconducting barrier, as discussed in Sec. 6.3, combining all four processes reflection, Andreev reflection (AR), crossed Andreev reflection (CAR) and co-tunneling (CT), the final state of the wavefunction Ψ_{out} is related to the initial state by the $\mathbb{S}$-matrix of the single barrier system as:

$$\Psi_{out} = \mathbb{S}\ \Psi_{in}. \tag{6.18}$$

Here the $\mathbb{S}$-matrix is the combination of all the four processes and can be written as:

$$\mathbb{S} = \mathbb{R} + \mathbb{R}_A + \mathbb{T} + \mathbb{T}_A, \tag{6.19}$$

where $\mathbb{R}$, $\mathbb{R}_A$, $\mathbb{T}$, $\mathbb{T}_A$ are respectively reflection, AR, CT and CAR matrix, which are each 4×4, as the wavefunction has four components. The numerical values for these amplitudes can be obtained by matching the electron and hole wave-functions between the normal and proximity induced superconducting graphene at each of the four interfaces and the numerical results for the resonances are discussed in Sec. 6.3.4. It is possible to construct the net amplitudes for different processes for a double barrier system form these matrices by summing up all possible paths as discussed below in Sec. 6.3.2.

Let us first consider the AR matrices which converts electrons (holes) to holes (electrons) at each interface. The elements of the AR matrix can be derived using

$$\begin{aligned}
\mathbb{R}_A\psi^{e+} &= r_{A,he}\psi^{h-} \\
\mathbb{R}_A\psi^{e-} &= r_{A,he}\psi^{h+} \\
\mathbb{R}_A\psi^{h+} &= r_{A,eh}\psi^{e-} \\
\mathbb{R}_A\psi^{h-} &= r_{A,eh}\psi^{e+}\ ,
\end{aligned} \tag{6.20}$$

where $t_{A,eh}$ and $t_{A,he}$ are AR coefficients for holes and electrons for the NS interface. Each of this conditions gives two equations, and we have only 8 non zero elements in the matrix $\mathbb{R}_A$ if there is no reflection. More explicitly, the matrix elements $(\mathbb{R}_A)_{i,j}$ are[ii]:

$$\begin{aligned}
(\mathbb{R}_A)_{3,1} &= r_{A,he}\frac{e^{i\alpha'/2}+e^{-i\alpha'/2}e^{i\alpha}}{e^{-i\alpha/2}+e^{i\alpha/2}e^{i\alpha}}\sqrt{\frac{\cos\alpha}{\cos\alpha'}}\\
(\mathbb{R}_A)_{3,2} &= r_{A,he}\frac{e^{i\alpha'/2}e^{i\alpha}-e^{-i\alpha'/2}}{e^{i\alpha/2}e^{i\alpha}+e^{-i\alpha/2}}\sqrt{\frac{\cos\alpha}{\cos\alpha'}}\\
(\mathbb{R}_A)_{4,1} &= r_{A,he}\frac{e^{-i\alpha'/2}-e^{i\alpha'/2}e^{i\alpha}}{e^{-i\alpha/2}+e^{i\alpha/2}e^{i\alpha}}\sqrt{\frac{\cos\alpha}{\cos\alpha'}}\\
(\mathbb{R}_A)_{4,2} &= r_{A,he}\frac{e^{-i\alpha'/2}e^{i\alpha}+e^{i\alpha'/2}}{e^{i\alpha/2}e^{i\alpha}+e^{-i\alpha/2}}\sqrt{\frac{\cos\alpha}{\cos\alpha'}},
\end{aligned} \tag{6.21}$$

In particular, for $\alpha = 0$, the matrix is much more simple and can be written as:

$$\mathbb{R}_A = \begin{pmatrix} 0 & 0 & r_{A,eh} & 0\\ 0 & 0 & 0 & r_{A,eh}\\ r_{A,he} & 0 & 0 & 0\\ 0 & r_{A,he} & 0 & 0 \end{pmatrix}. \tag{6.22}$$

We can also write down the 4×4 transmission matrix $\mathbb{T}_C = \mathbb{T} + \mathbb{T}_A$ which allows for both normal transmission and CAR through a single barrier. This matrix is defined by

$$\begin{aligned}
\mathbb{T}_C\psi^{e\pm} &= t_e\psi^{he\pm} + t_{A,e}\psi^{h\pm}\\
\mathbb{T}_C\psi^{h\pm} &= t_h\psi^{eh\pm} + t_{A,h}\psi^{e\pm},
\end{aligned} \tag{6.23}$$

where $t_{A,eh}$ and $t_{A,he}$ are CAR coefficients for holes and electrons through the barrier; t_h and t_e are the CT coefficients for holes and electrons for the barrier. We find that the matrix elements are given by

$$\mathbb{T}_C = \frac{1}{V}\begin{pmatrix} t_e & 0 & t_{A,eh}\cos\alpha_+ & it_{A,eh}\sin\alpha_-\\ 0 & t_e & it_{A,eh}\sin\alpha_- & -t_{A,eh}\cos\alpha_+\\ t_{A,he}\cos\alpha_+ & it_{A,he}\sin\alpha_- & t_h & 0\\ it_{A,he}\sin\alpha_- & -t_{A,he}\cos\alpha_+ & 0 & t_h \end{pmatrix},$$

where $V = \sqrt{\cos\alpha\cos\alpha'}$, $\alpha_\pm = (\alpha \pm \alpha')/2$. Clearly $\mathbb{T}_B$ includes both normal transmission and CAR. It is also clear that $\mathbb{T}_B$ can be written as $\mathbb{T}_B = \mathbb{T} + \mathbb{T}_A$ where $\mathbb{T}$ is a 4×4 matrix with two non-zero 2×2 diagonal blocks and $\mathbb{T}_A$ is a 4×4 matrix with two non-zero 2×2 non-diagonal blocks.

[ii]The other elements of the matrix $\mathbb{R}_A$ are found by interchanging $\alpha \leftrightarrow -\alpha'$, $r_{A,he} \to r_{A,eh}$ and also changing their positions to the other off-diagonal block.

6.3.2 Andreev bound levels

Andreev bound states are formed due to multiple Andreev reflections (for non zero incidence angle, by multiple *retro* Andreev reflections only). To sum up all possible paths, we need to take into account the phase a particle acquires while traveling in between the superconductors. The phase matrix relating the electron and hole wave-function when it traverses the normal graphene region through a distance L (the distance between the two superconductors) is given by

$$\mathbb{M} = \lambda^{-1}\mathbb{D}\lambda \ , \tag{6.24}$$

where

$$\lambda = \begin{pmatrix} \Lambda & 0 \\ 0 & \Lambda' \end{pmatrix} \ , \tag{6.25}$$

and $\mathbb{D}$ is a diagonal matrix with the entries $(e^{ikL}, e^{-ikL}, e^{ik'L}, e^{-ik'L})$ denoting the phases picked up by the left and right moving electrons and holes respectively. The Λ and Λ' matrices which rotate the momentum operator to an arbitrary basis are given by

$$\Lambda = \Lambda^{-1} = \frac{1}{\sqrt{2\cos\alpha}} \begin{pmatrix} e^{-i\alpha/2} & e^{i\alpha/2} \\ e^{i\alpha/2} & -e^{-i\alpha/2} \end{pmatrix} \tag{6.26}$$

with

$$\Lambda' \ = \ \frac{1}{\sqrt{2\cos\alpha'}} \begin{pmatrix} e^{-i\alpha'/2} & -e^{i\alpha'/2} \\ e^{i\alpha'/2} & e^{-i\alpha'/2} \end{pmatrix} \ . \tag{6.27}$$

The condition for resonance or for a bound state in the normal graphene region between the two superconductors is now just the condition that the total transmission computed as

$$\begin{aligned} \psi_T &= \mathbb{T}_C \left[\mathbb{M} + \mathbb{M}\mathbb{R}_A\mathbb{M}\mathbb{R}_A\mathbb{M} + \dots\right] \mathbb{T}_C\psi^{e+} \\ &= \mathbb{T}_C\mathbb{M}\left[\mathbb{I} - \mathbb{R}_A\mathbb{M}\mathbb{R}_A\mathbb{M}\right]^{-1} \mathbb{T}_C\psi^{e+} \end{aligned} \tag{6.28}$$

has a vanishing denominator. This is precisely the condition for the Andreev bound states formed by *retro* ARs *without the presence of reflection*. From this condition, one can find the corresponding Andreev bound state energy levels. Note that if we want the total transmission of electrons, we just need to replace $\mathbb{T}_C$ by $\mathbb{T}$ and if we want the total CAR of holes, we need to replace $\mathbb{T}_C$ by $\mathbb{T}_A$. Both of them show the effect of the resonances[iii]. We will discuss the effect of specular reflection (along with SAR) in the Sec. 6.3.3. In our analysis we have used left-right symmetry, but we have been careful to maintain the distinction between electron and hole parameters, since exact electron-hole symmetry only exists at $\epsilon = 0$. At any finite energy, the symmetry is broken.

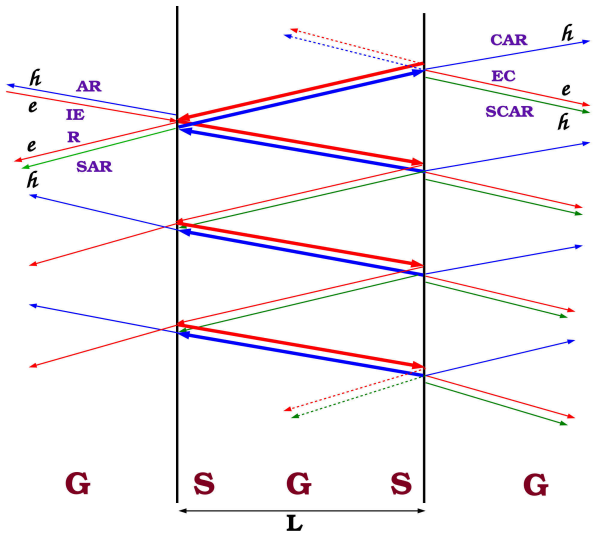

Figure 6.4: The electron and hole paths contributing to the formation of Andreev bound levels between the two superconductors. The electrons have been shown as red lines, the retro AR, CAR holes as blue lines and the SAR, SCAR holes as green lines. The bound levels formed by multiple retro AR have been shown as thick red and blue lines. However, not all possible paths have been shown in the figure.

6.3.3 Effect of reflection and SAR

For normal incidence in graphene, due to chirality (Sec. 1.3.3), normal reflection is prohibited and we have pure Andreev bound states between the two superconductors. Normal bound states (formed by multiple ordinary reflections) are, in any case, not possible in graphene even at any other incident angle, when ordinary reflection is allowed. This is because multiple ordinary reflections are specular in nature and lead to a mode running along the y-axis, rather than a bound state. This is also true even if we have SAR, which leads to a specular Andreev mode running along the y-axis .[159]

However, at a non-zero angle of incidence, if we have specular reflection present (Andreev as well as normal) at each graphene NS interface, we can still have Andreev bound states formed by multiple retro AR in between the two superconducting barriers. However, due to the specular nature of the reflection and the SAR, they are no longer localized. This is shown in Fig. 6.4. The incident electron can transmit through the first superconducting barrier as an electron and then have multiple retro AR. It can also have either ordinary reflection or SAR from the interface. The transmitted electron once again (in fact, for several times, depending on the length of the graphene sheet in the y-direction) can have multiple retro AR before it is finally transmitted (or reflected) as

[iii] Also, note that α needs to be small in order to ensure that the reflection is mainly retro-reflection.

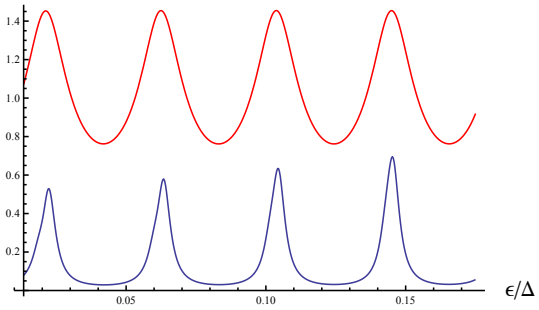

Figure 6.5: The bottom graph shows the behavior of angle resolved conductance, obtained numerically, in units of $4e^2/h$ as a function of energy in the subgapped regime ($\epsilon \ll \Delta$) for $k_y = 0.75$. Here, $\Delta/E_F = 0.05$ and $U_0/E_F = 10.0$. The top graph depicts the denominator of Eq. 6.28 for the same parameter values.

an electron or a hole through the graphene SDB structure. The electron can also cross the first superconductor as a hole by retro CAR and then have multiple retro-reflections from the two interfaces and then this process can continue as well.

The number of reflections (or SAR 's) that can occur in a given sample is controlled by the length of the graphene sheet in the y-direction and the angle of incidence of the electron. Naively, the number should go as $L_y/L\sin\alpha$, where L_y is the length of the sheet in the y-direction and L and α have already been defined earlier. In Fig. 6.4, we have only shown some of the possible quantum mechanical paths to emphasize how the Andreev bound states can form between the two barriers. We have also shown only a single incident electron, but the incident electron can also be at any point along the y-axis. Hence, if we measure the total output current collected throughout the y-length of the graphene sample, we should to able to get the signature of the many Andreev bound states present between the two superconducting barriers.

In fact, the signatures of the Andreev bound states should be present in all the four amplitudes r_c, r_{Ac}, t_c and t_{Ac}, where these four amplitudes denote the quantum mechanical amplitudes for reflection, AR (SAR), transmission and CAR (SCAR) across the SDB structure for an incident electron. They should show either a maximum or a minimum precisely at the Andreev levels obtained in Eq. 6.28. The Andreev levels can be obtained by measuring the transmissions and reflections through a SDB system even for large enough L_y; it does not require an effective 'one-dimensional' system. Furthermore, the signature of the resonances occurs in all the four amplitudes.

To illustrate the above argument, in Fig.6.5, we compare the positions of the resonances as a function of ϵ/Δ obtained by the vanishing of the denominator of Eq. 6.28, the analytically obtained Andreev levels, (which do not include the effects of reflection) with the numerically obtained values of the conductance (by solving the scattering problem in the next section) for the same parameter values. Note that the numerical results do include reflection since we have chosen $k_y = 0.75$. Moreover, the numerical results include transmission throughout all points along the y-axis (width of the graphene sheet). But

as can be seen from the figure, the resonances still fall on top of each other. This clearly shows that the presence of specular reflection (and SAR) has no effect on the position of the resonances which simply occur due to the formation of the Andreev bound states discussed in the earlier section.

6.3.4 Numerical results

In this section we describe the consequences of all the allowed quantum mechanical processes across the SDB geometry in graphene. To the left of the SDB structure, with an incident electron from the left, the wave-function can be written as

$$\psi^{e+} + r_c\psi^{e-} + r_{Ac}\psi^{h-} \tag{6.29}$$

and to the right of the SDB structure, the wave-function can be written as

$$t_c\psi^{e+} + t_{Ac}\psi^{h+} \ . \tag{6.30}$$

The scattering problem can be solved numerically by matching the wavefunctions for the normal and proximity induced superconducting regions (Eq. (G.3)-Eq. (G.6)) at the four NS interfaces in graphene ($x = 0, a, a + L, 2a + L$) forming the SDB structure to obtain the four amplitudes r_c, r_{Ac}, t_c and t_{Ac} for an incident electron with energy ϵ below the gap Δ. Note that we distinguish between electron and hole parameters, and hence the four amplitudes will be different for incident electrons and holes. In

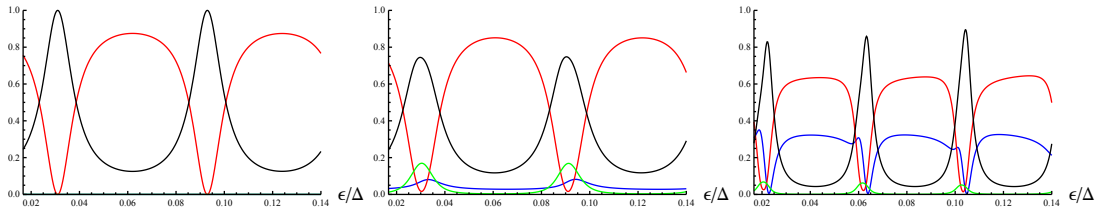

(a) $k_y = 0$ (b) $k_y = 0.2$ (c) $k_y = 0.75$

Figure 6.6: The behavior of all possible quantum mechanical scattering probabilities ($|r_c|^2, |t_c|^2, |r_{Ac}|^2, |t_{Ac}|^2$) through the graphene SDB structure are plotted as a function of energy in the subgapped regime ($\epsilon \ll \Delta$) for three different values of k_y. In (a), (b) and (c) solid red, green, blue and dashed black lines correspond to the $|r_{Ac}|^2, |r_c|^2, |t_{Ac}|^2$ and $|t_c|^2$ respectively. Here, $\Delta/E_F = 0.05$ and $U_0/E_F = 10.0$.

the numerical analysis we do not distinguish between the specular and retro Andreev reflections and also the normal reflection at each NS interface is allowed, besides normal transmission and CAR (specular and retro). The numerical results clearly show that for normal incidence of electron ($\alpha = 0$), the net normal transmission (CT) t_c and the net AR r_{Ac} show resonant behavior in the subgapped ($\epsilon \ll \Delta$) regime. This is shown in the first panel in Fig. (6.6). For normally incident electrons, due to the chirality (which prohibits reflection) and formation of Andreev bound state, we see a tunneling resonance, which is completely forbidden in a normal double barrier (DB) structure in graphene due

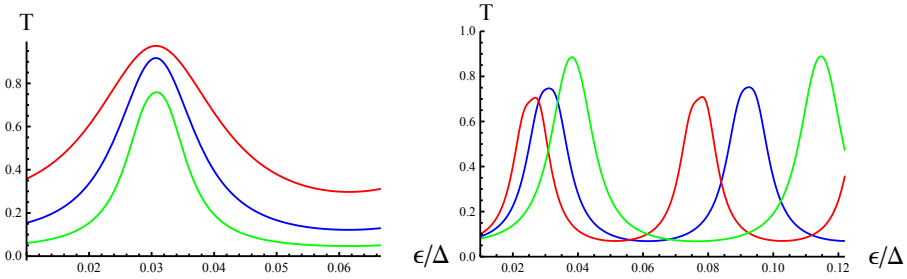

(a) (b)

Figure 6.7: (a) The behavior of the transmission resonances ($T = |t_c|^2$) is plotted as a function of energy in the subgapped regime ($\epsilon \ll \Delta$) for three different values of a/L ratio. The red, blue and green lines correspond to the three different values of a/L which are 0.012, 0.017 and 0.022 respectively. (b) The distance between consecutive resonances for the same three different values of a/L. For both the figures $k_y = 0.125$.

to the Klein tunneling. This is the striking difference between a normal DB and a SDB in graphene.

We also vary the momentum k_y or equivalently the angle of incidence, and study the resonances in Fig. 6.5. As we have already mentioned, at $k_y = 0$ or normal incidence, we have non-zero values only for r_{Ac} and t_c, and strong resonant behavior for the transmission t_c. As soon as the angle of incidence changes, we see the evolution of the t_c, r_c, t_{Ac} and r_{Ac} in the panels in Fig. 6.6. As we increase the angle of incidence, due to finite k_y, normal reflection r_c between the barriers increases, and due to the presence of both r_c and r_{Ac} between the barriers the amplitude of the transmission resonances decreases. However, at very large k_y, the roles of reflection and Andreev reflection switch.[158] Hence, for large k_y, we find large values of r_c, but very small values of r_{Ac} and once again, strong transmission resonances emerge.

These resonances can also be tuned by varying parameters such as the ratio of the width of the superconductor a to the length between the two superconducting barriers L. As a/L increases, we find that the resonances become sharper, and the distance between consecutive resonances increases. The behavior of the resonances as a function of a/L is shown in Figs. 6.7(a) and 6.7(b).

Angle-resolved differential conductance:

The net angle-resolved differential conductance through the SDB system is now given by

$$G = N * G_0 \Big[|t_A|^2 \cos(\alpha') - |t|^2 \cos(\alpha) \Big] \ , \tag{6.31}$$

where N is the number of input channels or transverse modes in a graphene sheet of width L_y, $G_0 = 4e^2/h$ is the unit of conductance and the factor of 4 comes from the pseudo-spin and valley degeneracies present in graphene. In our numerical analysis we have considered the temperature to be zero and also assumed linear bias. We again wish to emphasize the

fact that since multiple Andreev reflections between the two superconducting barriers not only include both specular and retro AR, but also normal reflections, the exit point from the second superconductor can be anywhere along the width (y-axis) of the graphene sheet. Therefore, both normal reflection as well as SAR can change the position of the

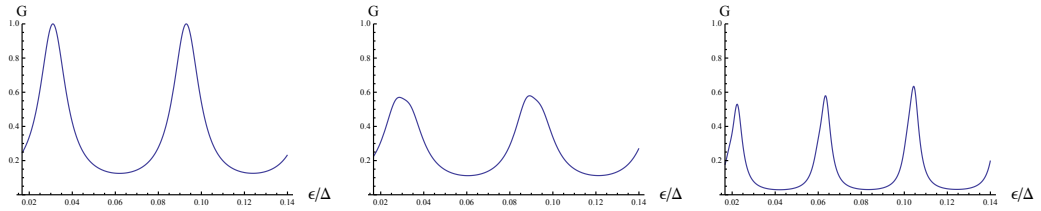

(a) $k_y = 0$ (b) $k_y = 0.2$ (c) $k_y = 0.75$

Figure 6.8: The behaviour of the angle-resolved differential conductance in units of $4e^2/h$ as a function of energy in the subgapped regime ($\epsilon \ll \Delta$) for three different values of k_y. Here, $\Delta/E_F = 0.05$ and $U_0/E_F = 10.0$.

transmitted beam along the y-axis at each reflection. Hence, the total transmission here includes transmission at all points along L_y. In other words, the output lead has also to be as wide as the graphene sheet. In Fig. 6.8, we show the net angle resolved Landauer-Buttiker conductance, given in Eq. 6.31, (for $N = 1$) as a function of the energy of the incident electron $\epsilon \ll \Delta$, where again, the resonant behavior can be seen for different values of k_y or the incident angle. The behavior of the conductance, also shows how the Andreev levels evolve as a function of the incident angle, showing that the height of the resonances is large when the multiple reflection between the barriers is either dominated by retro AR (small angles) or normal reflection (large angles).

6.4 Quantum Charge Pumping

The phenomenon of quantum charge pumping corresponds to a net flow of DC current between different electron reservoirs (at zero bias) connected via a quantum system whose parameters are periodically modulated in time.[169–171] The zero-bias current is obtained in response to the time variation of the parameters of the quantum system, which explicitly break time-reversal symmetry. It is necessary to break time-reversal symmetry in order to get net pumped charge, but it is not a sufficient condition. For obtaining a net pumped charge, parity or spatial symmetry must also be broken. Within a scattering approach, if the time period of modulation of the scattering system parameters is much larger than the time the particle spends inside the scattering region (dwell time), the adiabatic limit is reached. In this limit, the pumped charge in a unit cycle becomes independent of the pumping frequency. This is referred to as "adiabatic charge

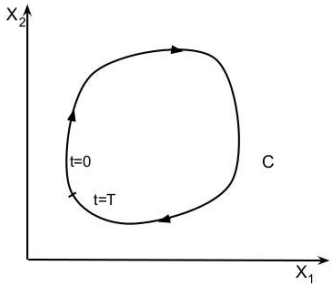

Figure 6.9: A pumping contour in $X_1 - X_2$ parameter space.

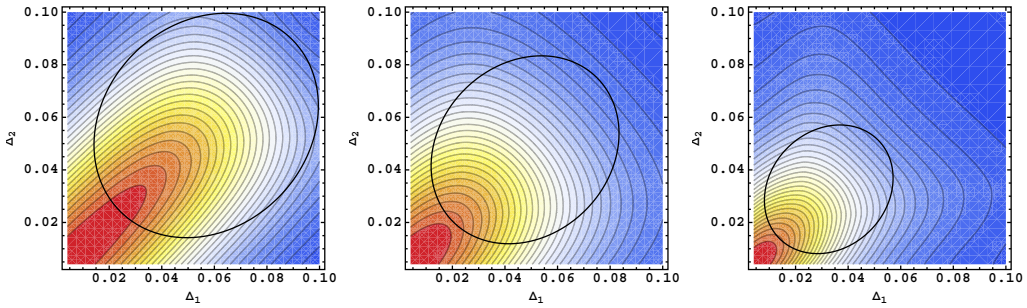

(a) $k_y = 0.0$ (b) $k_y = 0.3$ (c) $k_y = 0.75$

Figure 6.10: Contours of the transmission probability $|t_c|^2$ in the $\Delta_1 - \Delta_2$ plane for three different values of k_y. The steps between the maxima and minima of $|t_c|^2$ range approximately 1.0 to 0.1, 0.6 to 0.05 and 0.3 to 0.01 for the three cases $k_y = 0.0, 0.3$ and 0.75 respectively. In (a), (b) and (c) $a/L = 0.017, \Delta_0 = 40.0, U_0 = 10.0, \phi_1 = \phi_2 = 0.0$ and $\epsilon = 0.00142, 0.00121, 0.00082$ for the three contour plots respectively. The black circle represents the pumping contour for the parameter values $\omega = 1.0, P = 30.0$ and $\eta = 4\pi/9$.

pumping".[171] In recent years, quantum charge and spin pumping through various mesoscopic samples, involving quantum dots and quantum wires, have attracted increasing interest both theoretically[172–184] and experimentally,[185–189] both in the adiabatic regime and otherwise.

For a scattering matrix formulation of the quantum pumping, let us consider the scattering matrix $S(X_1, X_2)$ describes an open system, where X_1 and X_2 are two parameters of the system, which can be potential well, for example. A closed contour in this parameter space can be obtain by varying them with time periodically (Fig. 6.9). Then the net pumped charge in one cycle is given by the Brouwer's formula[171] (for a channel m)

$$Q = \frac{e}{\pi} \oint_C dX_1 dX_2 \sum_{\alpha} \sum_{\beta \in m} \frac{\partial S^*_{\alpha\beta}}{\partial X_1} \frac{\partial S_{\alpha\beta}}{\partial X_2} \ . \tag{6.32}$$

In the recent past, a graphene-based quantum pump has been considered in literature[190,191] where pumped charge is obtained in an adiabatic quantum pump device based on a graphene monolayer modulated by two oscillating gate potentials. However, the pumped charge obtained in these kind of devices is quite small.

6.4.1 Quantum charge pumping in SDB structure

Quantum charge pumps, using a variety of setups involving superconductors, have also been of major interest in recent years.[192–202] Also, very recently, adiabatic charge pumping in graphene with superconductors has also been considered.[203] In this section we consider quantum pumping of electrons (in the adiabatic limit) across an SDB structure in graphene, as depicted in Fig. 6.3.

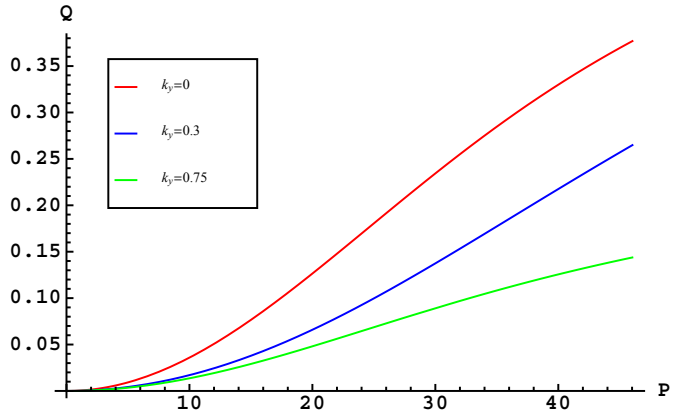

Figure 6.11: The value of the pumped charge $\mathcal{Q}$ in units of electron charge e, for pumping in $\Delta_1 - \Delta_2$ plane, is shown as a function of the pumping strength P for three different values of k_y. Here $a/L = 0.017, \omega = 1.0, \eta = 4\pi/9, \Delta_0 = 40.0$, $U_0 = 10.0$, $\phi_1 = \phi_2 = 0.0$ and $\epsilon = 0.00142, 0.00121, 0.00082$ for the three plots respectively.

In principle, one can explore two scenarios to achieve significant amount of pumped charge

1. by periodic modulation of amplitudes Δ_1 and Δ_2 of the gaps at the two superconducting barriers (SB) or alternatively,

2. by periodic modulation of the order parameter phases ϕ_1 and ϕ_2 associated with the two barriers.

Since it has been seen[202] that the second alternative leads to less pumped charge, we consider the first alternative here. In the SDB geometry, when we consider Δ_1 and Δ_2 as the pumping parameters, we can always choose a pumping contour which completely encloses the transmission resonance discussed in Sec. 6.3.4. If the resonance is sharp enough it is possible for the pumped charge to be large.

So, for a numerical analysis for calculating the pumped charge through the SDB structure, we choose Δ_1, Δ_2 to oscillate with the frequency ω, with a modulation parameter P, and a phase difference 2η between them:

$$\begin{aligned} \Delta_1 &= [\Delta_0 + P\cos(\omega t + \eta)]\epsilon \\ \Delta_2 &= [\Delta_0 + P\cos(\omega t - \eta)]\epsilon \ . \end{aligned} \tag{6.33}$$

$\Delta_0\epsilon$ is the mean value of the amplitude around which the two pumping parameters are modulated with time and P is the pumping strength. Here ϵ is the energy of the incident electron. It is adjusted to be close to an Andreev bound level, so that the SDB is close to a resonance. Hence, effectively by varying P, for fixed ϵ we vary the ratio ϵ/Δ. By fixing ϵ to be close to the resonance, we maximise the pumped charge. The presence of two time-varying potentials with a phase difference between them explicitly violates

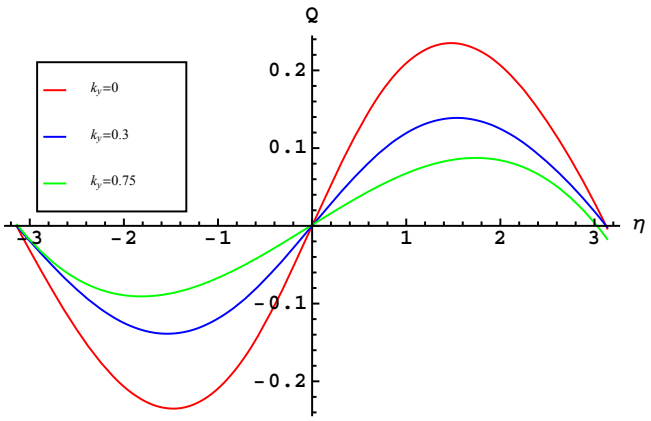

Figure 6.12: The value of the pumped charge $\mathcal{Q}$ in units of electron charge e, for pumping in $\Delta_1 - \Delta_2$ plane, is shown as a function of the phase difference between the two pumping parameters η for three different values of k_y. Here $a/L = 0.017, \omega = 1.0, P = 30.0, \Delta_0 = 40.0$, $U_0 = 10.0$, $\phi_1 = \phi_2 = 0.0$ and $\epsilon = 0.00142, 0.00121, 0.00082$ for the three plots respectively.

parity, which is a necessary condition for obtaining pumped charge. The frequency of the potential modulation is kept small in comparison to the characteristic times for traversal and reflection, so that the pump is in the adiabatic limit.

The transmission probability ($|t_c|^2$) in the $\Delta_1 - \Delta_2$ plane for three different transverse electron momentum k_y is shown in Fig. 6.10. Fig. 6.10 (a) shows the $|t_c|^2 = 1$ resonance for normal incidence of electrons, which gets damped for nonzero values of k_y as normal reflection and CAR (and SCAR) also take part in transport (Fig. 6.10(b) and (c)).

Using the modified version of the Brouwer's formula Eq. (6.32), the pumped charge in one cycle through the graphene SDB structure can written as[171,201,202]

$$\mathcal{Q} = \frac{e}{2\pi}\int_0^\tau dt \left[\left(|r_c|^2\dot{\theta} + |t_c|^2\dot{\chi}\right)\cos\alpha - \left(|r_{Ac}|^2\dot{\beta} + |t_{Ac}|^2\dot{\gamma}\right)\cos\alpha'\right], \quad (6.34)$$

where θ, χ, β and γ correspond to the phases of the reflection, transmission, AR (and SAR) and CAR (and SCAR) amplitudes respectively. Note the negative sign in Eq. (6.34), which results from the fact that r_{Ac} and t_{Ac} correspond to the conversion of an electron into a hole. Thus, the pumped charge through the SDB structure in graphene is directly related to the amplitudes and phases that appear in the $\mathbb{S}$-matrix. Inserting the unitarity relation $|r_c|^2 + |t_c|^2 + |r_{Ac}|^2 + |t_{Ac}|^2 = 1$ in Eq. (6.34), we obtain

$$\mathcal{Q} = \frac{e}{2\pi}\int_0^\tau dt \left[|r_c|^2\left(\dot{\theta}\cos\alpha + \dot{\beta}\cos\alpha'\right) + |t_c|^2\left(\dot{\chi}\cos\alpha + \dot{\beta}\cos\alpha'\right) + |t_{Ac}|^2\left(\dot{\beta} - \dot{\gamma}\right)\cos\alpha' - \dot{\beta}\cos\alpha'\right]. \quad (6.35)$$

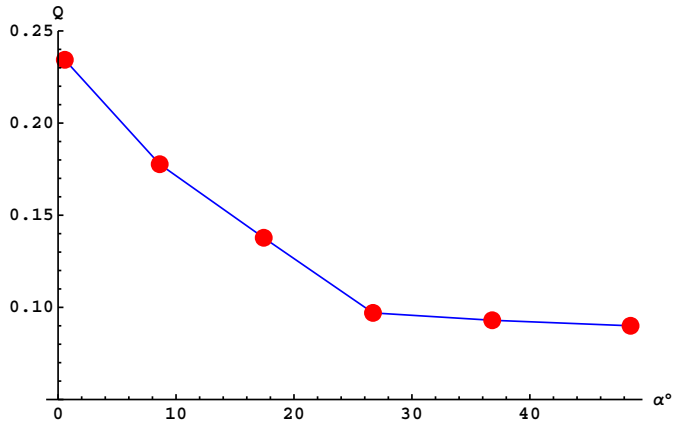

Figure 6.13: The maximum value of the pumped charge $\mathcal{Q}_{max}$ in units of electron charge e through the SDB structure, for pumping in $\Delta_1 - \Delta_2$ plane, is shown as a function of the incident angle α.

Also, note that if we substitute $k_y = 0$, (*i.e.* $\alpha = \alpha' = 0$) in Eq. (6.35), then the formula reduces to

$$\mathcal{Q} = \frac{e}{2\pi}\int_0^\tau dt \left[|t_c|^2\Big(\dot{\chi}+\dot{\beta}\Big) - \dot{\beta}\right] . \tag{6.36}$$

which is precisely the modified Brouwer's formula used in Ref. 202 for a quantum wire. In Eq. (6.36), the first term is called the "*dissipative part*" and the second term is known as the "*topological part*" and depends entirely on the time derivative of the AR phase.

The pumped charge is obtained by using Eq. (6.35) with Δ_1 and Δ_2 as the two pumping parameters. These two parameters are varied by periodically varying the top gate voltage which controls the Fermi energy of the electrons in the superconducting region. Thus essentially, as mentioned earlier, ϵ/Δ is varied for the two barriers periodically. Using Eq. (6.35), we obtain the pumped charge for various parameters of the system. In Fig. 6.11 and Fig. 6.12, we show the behavior of the pumped charge as a function of the pumping strength P and the phase difference between the two pumping parameters η respectively, for three values of k_y. Note that in Fig. 6.11(a), the pumped charge increases with the increase in the pumping strength P as a larger value of P corresponds to a larger pumping contour which encloses more and more of the resonance. Note also that the $|t_c|^2 = 1$ resonance at $k_y = 0$ is not a sharp resonance; it has a finite width because it also has contribution from the "*dissipative part*" as shown in Eq. (6.36). and is not purely topological. The "*dissipative part*" effectively reduces the pumped charge from integer values but we still obtain a fairly large value of pumped charge - where by large we mean that the pumped charge is a sufficiently large fraction of unity (roughly between 0.1 and 0.35). This is in sharp contrast to normal DB in graphene where the pumped charge[190] is very small (in the range of 10^{-4}, because there is no resonance due to Klein tunneling.

However for oblique incidence *i.e.* $k_y \neq 0$ (see Figs. 6.11(b) and (c)), we obtain relatively smaller values of pumped charge as in this case normal reflection, CT, AR (and SAR) and CAR (SCAR) also contribute to Eq. (6.35) and the interplay between all the quantum mechanical amplitudes and their phases result in smaller value of pumped charge.

In Fig. 6.12, we show the oscillatory behavior of pumped charge as a function of the phase difference η between the two time varying parameters. Here also we note that we obtain smaller values of pumped charge through the SDB geometry as we vary k_y from normal incidence to oblique incidence. Note also that in Fig. 6.12, for all three values of k_y, the pumped charge becomes maximum around $\eta \sim \pm\pi/2$.[171]

Finally, we also show the systematic behavior of the maximum value of pumped charge through the SDB geometry as a function of the incident angle α of the incident electron in Fig. 6.13. This behaviour clearly shows that the maximum value of the pumped charge becomes smaller as we vary α from normal incidence ($\alpha = 0$) to oblique incidence ($\alpha \neq 0$).

6.5 Summary & Discussion

To summarize, firstly, we have computed the transmission of an electron through a SDB structure in graphene and shown the resonant suppression of Andreev reflection at certain energies below the superconducting gap Δ where normal transmission $|t_c|^2$ becomes unity. This resonant behaviour is absent in a normal double barrier in graphene due to Klein tunneling. We also show that the resonant suppression is due to the formation of Andreev bound states between the two superconducting barriers. Even at finite incident angles, the position of these Andreev bound levels remains unchanged in presence of reflection and SAR, although the transmission resonances get damped as the incident angle increases due to reflection and SAR. However, at large angles, the roles of AR and ordinary reflection get reversed, and once again, we see strong transmission resonances.

Secondly, we have studied adiabatic quantum pumping through an SDB structure in graphene and have shown that in the $\Delta_1 - \Delta_2$ plane, pumped charge can be large (around 0.2- 0.3) in magnitude for normal incidence. This is in contrast to normal double barriers[190] in graphene, where the pumped charge is small (around 10^{-4}) due to the phenomenon of Klein tunneling. The evolution of the maximum value of pumped charge as a function of the angle of incidence of the incoming electron shows monotonic decrease of pumped charge as we increase the angle of incidence of the incoming electron.

Similar behavior has also been predicted for many other systems where one studies quantum pumping through nanostructures. Integer pumped charge has been shown for pumping through quantum dots[176–178] as well as through Luttinger liquids.[179,182,183,202] In more recent times, similar behaviour of pumped charge has been predicted in graphene NIS junctions[203] and in an InAs Josephson pump.[204]

Possible experimental setups

As far as the practical realization of such a SDB structure in graphene is concerned, it should be possible to fabricate such a geometry by depositing thin strips of a spin singlet superconductor (like Al or Nb) on top of a graphene sheet[153] at two places. The

width of the strips should be of the order of the superconducting phase coherence length ($10 - 15nm$ in case of Nb) for CT and CAR (and SCAR) to take place. For a given a/L ratio, the $|t_c|^2 = 1$ resonance in this SDB geometry can be tuned by varying the energy of the incident electron. In Fig. 6.6(a) and 6.8(a), the equivalent temperature at which the first resonance occurs is approximately 10 mK (critical temperature $T_c \approx 9.2K$ in case of Nb) for $a \sim 10 - 15$ nm and $L \sim 2$ μm. Also different experiments need to be performed with ballistic graphene samples to obtain results at different angles of incidence.

We also expect the features of the resonances to be qualitatively unaffected by long-ranged impurities (slow on the scale of the lattice spacing *i.e.* $k_F l_m \gg 1$ where $k_F \sim 1/d$, d is the lattice spacing and l_m is the mean-free path of electron in graphene), because such impurities in graphene can only cause intra-valley scattering. On the other hand, short range impurities ($k_F l_m \ll 1$) can cause inter-valley scattering which can destroy the resonance. Also, strong disorder can localize electron/hole states between the two barriers which always can destroy the resonance. Another experimental variable which is expected to destroy the resonance is the presence of a magnetic field which bends the electron paths between the two barriers. Hence, it prevents the multiple retracing of the path, which is needed for resonance. Therefore, we do not expect resonances in the presence of strong disorder or even weak magnetic fields.

In the SDB geometry, pumped charge can be obtained by periodically varying the top gate voltage which controls the Fermi energy of the electrons in the superconducting region which amounts to varying ϵ/Δ for the two barriers periodically. The pumped current is expected to be in the range of pico-amperes when the pumping frequency is the order of a few MHz, and should be experimentally measurable.

List of Publications

Below is the list of my journal publications where the results of dissertation are published:

1. “Electron-phonon scattering in topological insulator thin films”
   Sébastien Giraud, Arijit Kundu, Reinhold Egger
   Phys. Rev. B 85, 035441 (2012) , arxiv: 1111.4063 [cond-mat]

2. ”Energy spectrum and broken spin-surface locking in topological insulator quantum dots”
   A. Kundu, A. Zazunov, A. Levy Yeyati, T. Martin, R. Egger
   Phys. Rev. B 83, 125429 (2011) , arxiv: 1102.4437 [cond-mat]

3. ”Quantum charge pumping through a superconducting double barrier structure in graphene”
   Arijit Kundu, Sumathi Rao and Arijit Saha
   Phys. Rev. B 83, 165451 (2011) , arxiv:1102.1447 [cond-mat]

4. ”Magnetic scattering of Dirac fermions in topological insulators and graphene”
   A. Zazunov, A. Kundu, A. Hütten, R. Egger
   Phys. Rev. B 82, 155431 (2010) , arxiv: 1007.5398 [cond-mat]

5. ”Resonant tunneling through superconducting double barrier structures in graphene”
   Arijit Kundu, Sumathi Rao and Arijit Saha
   Phys. Rev. B 82, 155441 (2010) , arxiv: 1007.3716 [cond-mat]

Conclusion

To conclude, in this dissertation I studied certain transport set-ups of Dirac Fermions on the surface of strong topological insulator and graphene. Spin-surface locking, which is an usual feature of Dirac Fermions on TI seems to be broken in a finite geometry, which we found by numerical calculation based on the low energy effective theory for materials like Bi_2Se_3. We also obtain sub-gap states for such geometry, which are located at the two caps of the cylinder. Some of these results are reproducible analytically with a surface Dirac Fermion theory. We perform a numerical calculation based on the tight-binding model for TI , which also confirms these features qualitatively. Some of these features may appear important for transport experiments, although the results are limited for a clean sample and also within the range of validity for the low-energy effective theory.

Thin-film geometries are often used in mesoscopic surface transport because of their large surface to bulk ratio. We computed the electron-phonon coupling induced resistivity of a TI thin-film based on the low energy effective Hamiltonian. The asymptotic behavior of the resistivity (ρ) with temperature (T) is obtained analytically and shows that $\rho \propto T^4$ for low-temperature and it goes linear with temperature for high temperature. The high temperature behavior can be explained physically from the Bosonic nature of the phonons and the low temperature behavior can be experimentally verified for a clean sample. But, my results are also limited to ideal cases, as we do not take into account the real-life effects of defects or disorders. For resistivity of thin-film, it may have considerable effect, specially at low temperature.

The magnetic interaction for TI and graphene has been formulated in a unified way, and we introduced a theory for scattering by static magnetic field. For a magnetic ring, we compute the resulting quasi-bound states and recover the Aharonov-Bohm results in a solenoid limit. The electron phonon coupling and magnetic field together can give rise to interesting physics, which we hope to consider in the future.

I also discussed a particular hybrid structure formed by graphene proximity induced superconductivity. In between two such barriers Andreev levels form which result in transmission resonances, which can be observed by possible experiment. We also obtain significantly large pumped charge in this geometry, although the variation of the pumping parameters we used can be difficult to implement in an experiment.

Both topological insulator and graphene are very active field of research of condensed matter physics. I hope my research contributed positively in the understanding of certain behaviors of electronic transport in these materials.

Appendix A

Berry Phase and TKNN invariant

Berry Phase and Curvature

Let us consider a system described by the Hamiltonian

$$H = H(\boldsymbol{R}) \quad ; \quad \boldsymbol{R} = \boldsymbol{R}(t) \ , \tag{A.1}$$

and lets consider an 'adiabatic evolution' of the system through a path 'C' in the parameter space $(R_1(t), R_2(t), \dots)$ (for eg. as shown one in fig A.1), while going from $t = 0$ to $t = t$. We can diagonalise the Hamiltonian at any point $\boldsymbol{R}$ of the parameter space, giving instanteneous eigenstates

$$H(\boldsymbol{R})|n(\boldsymbol{R}(t))\rangle = E_n(\boldsymbol{R}(t))|n(\boldsymbol{R}(t))\rangle \ , \tag{A.2}$$

$|n(\boldsymbol{R})\rangle$ are instantaneous eigenstates determined up to an arbitrary phase. Now, adiabatic theorem ensures that (as long as there is no level crossing) these states remain eigenstates of the system with the same instantaneous energy $E_n(\boldsymbol{R}(t))$. But the phase can be chosen arbitrarily at each point.

One way to fix this arbitraryness is to choose a smooth and single valued phase along the path C. If, at $t = 0$, we have the eigenstate $|n(\boldsymbol{R}(0))\rangle$, then, we can say that the eigenstate at $t = t$ is:

$$|\psi(t)\rangle = e^{-i\theta(t)}|n(\boldsymbol{R}(t))\rangle \ . \tag{A.3}$$

Here $\theta(t)$ is the smooth phase evolving through tha path C. Plugging in the Schrödinger equation, we have

$$H(\boldsymbol{R}(t))|\psi(t)\rangle = i\hbar\frac{d}{dt}|\psi(t)\rangle \ , \tag{A.4}$$

and using eq (A.2), we can obtain

$$\theta(t) = \frac{1}{\hbar}\int_0^t E_n(\boldsymbol{R}(t'))\ dt' \ - i\int_0^t \langle n(\boldsymbol{R}(t'))|\frac{d}{dt'}|n(\boldsymbol{R}(t'))\rangle\ dt' \ . \tag{A.5}$$

The first part is the dynamical phase, second part is called the **Berry phase**.[10] We can write,

$$|\psi(t)\rangle = e^{-i\frac{1}{\hbar}\int_0^t E_n(\boldsymbol{R}(t'))\ dt'} e^{i\gamma_n}|n(\boldsymbol{R}(t))\rangle \ , \tag{A.6}$$

where γ_n is the Berry phase

$$\begin{aligned}\gamma_n &= i\int_0^t \langle n(\boldsymbol{R}(t'))|\frac{d}{dt'}|n(\boldsymbol{R}(t'))\rangle \\ &= \int_C d\boldsymbol{R}\cdot\mathbf{A}_n(\boldsymbol{R}) \ , \end{aligned} \tag{A.7}$$

where

$$\mathbf{A}_n(\boldsymbol{R}) = i\langle n(\boldsymbol{R})|\nabla_{\boldsymbol{R}}|n(\boldsymbol{R})\rangle \tag{A.8}$$

is called the Berry connection. This is like a vector potential and is guage dependent. If we introduce a gauge:

$$|n(\boldsymbol{R})\rangle \to e^{i\lambda(\boldsymbol{R})}|n(\boldsymbol{R})\rangle \ ,$$

the Berry connection and Berry phase changes as:

$$\begin{aligned}\mathbf{A}_n(\boldsymbol{R}) &\to \mathbf{A}_n(\boldsymbol{R}) - \nabla_{\boldsymbol{R}}\lambda(\boldsymbol{R}) \ , \\ \gamma_n &\to \gamma_n - \int_C \nabla_{\boldsymbol{R}}\lambda(\boldsymbol{R})\cdot d\boldsymbol{R} \ . \end{aligned}$$

But, of course, for a closed orbit (as shown in fig A.1), the last integral vanishes. Also, for garateeing the eigenstates of the Hamiltonian to be singlevalued in the parameter space, we must require that, for a closed path

$$\gamma_n \to i\oint_C \langle n(\boldsymbol{R})|\frac{\partial}{\partial \boldsymbol{R}}|n(\boldsymbol{R})\rangle = 2m\pi \ , \tag{A.9}$$

where $m = 0$ or any integer.

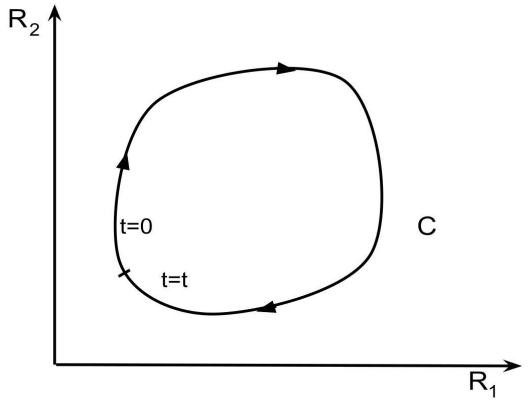

Figure A.1: A closed path in the 2D parameter space

Berry curvature

For a closed path, the Berry phase can be written as:

$$\begin{aligned}\gamma_n &= i\oint_C \mathbf{A}_n(\boldsymbol{R})\cdot d\boldsymbol{R} \ , \\ &= i\iint d\boldsymbol{S}\cdot(\nabla\times\mathbf{A}_n(\boldsymbol{R})) \ , \\ &= \iint d\boldsymbol{S}\cdot\boldsymbol{\Omega}_n(\boldsymbol{R}) \ , \end{aligned} \tag{A.10}$$

where $\boldsymbol{\Omega}_n(\boldsymbol{R}) = i(\nabla\times\mathbf{A}_n(\boldsymbol{R}))$ is called the Berry curvature. It is gauge invariant, and in tensorial notation it's components are written as:

$$\Omega^n_{\mu\nu} = i\left[\left\langle \frac{\partial n(\boldsymbol{R})}{\partial R^\mu}\middle|\frac{\partial n(\boldsymbol{R})}{\partial R^\nu}\right\rangle - \langle\nu\leftrightarrow\mu\rangle\right] \ . \tag{A.11}$$

Chern number

It can be proved in differential geometry, that in general, Berry curvature integrated over a closed manifold is quantised in the unit of 2π. This number is called the Chern number. One example of this comes in the case of Quantum Hall effect, which is discussed below.

Quantum Hall effect

The dynamics of Bloch electrons under the effect of an electric field is one of the oldest problems in solid-state physics. The velocity operator is:

$$\boldsymbol{v} = \dot{\boldsymbol{r}} = (i/\hbar)[H, \boldsymbol{r}] \ . \tag{A.12}$$

In the Bloch representationn (see ref. chap 1), it becomes

$$\begin{aligned} \boldsymbol{v}(\boldsymbol{q}) &= e^{-i\boldsymbol{q}\cdot\boldsymbol{r}}(i/\hbar)[H, \boldsymbol{r}]e^{i\boldsymbol{q}\cdot\boldsymbol{r}} \ , \\ &= (i/\hbar)\left(e^{-i\boldsymbol{q}\cdot\boldsymbol{r}}\boldsymbol{r}He^{i\boldsymbol{q}\cdot\boldsymbol{r}} - e^{-i\boldsymbol{q}\cdot\boldsymbol{r}}H\boldsymbol{r}e^{i\boldsymbol{q}\cdot\boldsymbol{r}}\right) \ , \\ &= \frac{\partial}{\partial(\hbar\boldsymbol{q})}\left(e^{-i\boldsymbol{q}\cdot\boldsymbol{r}}He^{i\boldsymbol{q}\cdot\boldsymbol{r}}\right) \ , \\ &= \frac{\partial H(\boldsymbol{q})}{\hbar\partial\boldsymbol{q}} \ . \end{aligned} \tag{A.13}$$

Now, lets consider a 1D system described by a Bloch Hamiltonian with a time dependent perturbation $H(q,t)$. It can be shown by perturbative analysys (ref), that the average velocity of electron in the nth band has the form:

$$\begin{aligned} \langle v_n(q)\rangle &= \frac{\partial\epsilon_n(q)}{\partial q} - i\left[\left\langle\frac{\partial u_n}{\partial q}\middle|\frac{\partial u_n}{\partial t}\right\rangle - \left\langle\frac{\partial u_n}{\partial q}\middle|\frac{\partial u_n}{\partial t}\right\rangle\right] \ , \\ &= \frac{\partial\epsilon_n(q)}{\partial q} - \Omega^n_{qt} \ , \end{aligned} \tag{A.14}$$

where ϵ_n is the nth band, and u_n is the wavefunction of nth band electron. The second term of the last equation is called the 'Anomalous velocity' and it plays a crucial role in many topological features of a system, for example in the quantum Hall effect,[5] which is discussed in chapter 1.

The quantisation of Hall conductivity was explained by Laughlin[205] based on gauge invariance. But, this can be explained by Berry phase formulation and can be related to a topological invariance of the energy bands. Let us consider a uniform electric field $\boldsymbol{E}$ on a lattice. If we express it in terms of a time varying vector potential $\boldsymbol{A}(t)$, which is uniform in space, then the Bloch description (see sec 1.2.1) is still valid, and we can switch to the Bloch-momenta representation

$$H(\boldsymbol{q}, t) = H\left(\boldsymbol{q} + \frac{e}{\hbar}\boldsymbol{A}(t)\right) \ , \tag{A.15}$$

and we can rewrite the crystal momenta

$$\boldsymbol{k} = \boldsymbol{q} + \frac{e}{\hbar}\boldsymbol{A}(t) \ . \tag{A.16}$$

Also, as $\boldsymbol{A}(t)$ does not break lattice symmetry, $\boldsymbol{q}$ is still a constant of motion $\dot{\boldsymbol{q}} = 0$. Then

$$\dot{\boldsymbol{k}} = -\frac{e}{h}\boldsymbol{E}.$$

After some algebra, from Eq (A.14) (for arbitray dimension), we obtain

$$\boldsymbol{v}_n(\boldsymbol{k}) = \frac{\partial \epsilon_n(\boldsymbol{k})}{\partial \boldsymbol{k}} - \frac{e}{\hbar}\boldsymbol{E} \times \boldsymbol{\Omega}^n(\boldsymbol{k}) \ , \tag{A.17}$$

where $\boldsymbol{\Omega}^n$ is the Berry curvature for nth band. Hall conductivity is the conductivity in the direction perpendicular to the electric field $\boldsymbol{E}$. From the above equation, we obtain the hall conductivity for a 2D system

$$\sigma_{xy} = \frac{e^2}{\hbar}\int_{\mathrm{BZ}} \frac{d^2k}{(2\pi)^2} \sum_{\text{Filled } n} \Omega^n_{k_x k_y} \ , \tag{A.18}$$

where the sum is over the entire Brillouin zone. Here again, we integrate the Berry curvature over a closed manifold, which is the BZ in 2D (a torus). For each band it gives the corresponding Chern number

$$n_i = \frac{1}{2\pi}\int_{\mathrm{BZ}} \frac{d^2k}{(2\pi)^2} \Omega^n_{k_x k_y} \ , \tag{A.19}$$

where summing up all the occupied band contributions defines the TKNN invariant[8] (by the name of Thouless, Kohmoto, Nightingale and den Nijs) $n_C = \sum_{\text{Filled } i} n_i$

$$n_C = \frac{1}{2\pi}\int_{\mathrm{BZ}} \frac{d^2k}{(2\pi)^2} \sum_{\text{Filled } n} \Omega^n_{k_x k_y} \ , \tag{A.20}$$

and consequently the Hall conductivity is quantised in the unit of (e^2/h)

$$\sigma_{xy} = n_C \frac{e^2}{h} \ . \tag{A.21}$$

Appendix B

Microscopic Tight-Binding Approach for TI nanotube

A simple microscopic model for a strong TI was previously proposed by Fu, Kane, and Mele.[71] The model consists of a single-band tight-binding model on a diamond lattice and includes spin-orbit couplings. With lattice fermion operators c_i (spin is kept implicit), this Hamiltonian has the form

$$H_{\rm tb} = \sum_{\langle i,j\rangle} t_{ij} c_i^\dagger c_j + \frac{4i\lambda_{\rm so}}{a^2} \sum_{\langle\langle i,j\rangle\rangle} c_i^\dagger \left(\boldsymbol{\sigma}\cdot\left[\boldsymbol{d}_{ij}^1 \times \boldsymbol{d}_{ij}^2\right]\right) c_j, \tag{B.1}$$

where a is the cubic lattice constant, t_{ij} are hopping parameters connecting nearest neighbors, and the last term describes spin-orbit coupling of strength $\lambda_{\rm so}$ through a second-neighbor hopping between sites i, j, which depends on the two nearest-neighbour vectors $\boldsymbol{d}^{1,2}$ connecting those two sites. In order to generate a full gap in the bulk spectrum, a distortion $t_{ij} \to t + \delta t$ is introduced for $\boldsymbol{d}_{ij}$ along the (111) direction.[71] We use this model to construct the surface states of an infinite nanowire and nanotube TI and compare the results we obtained in Chapter 2 and 3.

TI nanowire:

To define the nanowire, we proceed by selecting the growth direction $\hat{e}_z$ along the (111) axis and keeping all sites within a given radius R. The unit cell of the infinite nanowire thus defined contains six planes of sites corresponding to the three stacking of the two fcc sublattices of the diamond lattice, and has the period $d_{\rm cell} = \sqrt{3}a$. It is worth mentioning that even though a $\boldsymbol{k}\cdot\boldsymbol{p}$ expansion of $H_{\rm tb}$ around the $\frac{\pi}{a}(1,1,1)$ point does not match completely with Eq. (2.4), the main features of the surface states are equivalent in both descriptions and quantitatively similar behavior of the surface gap Δ_s as a function of R has been obtained[66] by setting $a = 2.8$ nm and $-2t + \delta t = M_0$. The band structure of the infinite nanowire is shown in Fig. B.1 (red lines). Note that in the infinite wire case, one obtains $\langle\sigma_r\rangle = 0$ consistent with spin-surface locking.[66]

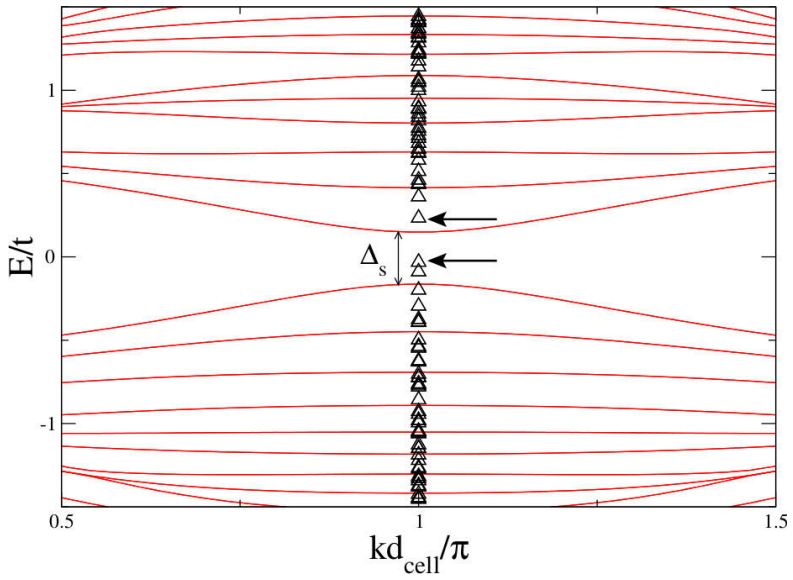

Figure B.1: Band structure of the infinite TI nanowire (red solid curves) and energy levels (denoted by open black triangles) of a finite dot. These results follow from the tight-binding model [Eq. (B.1)] with wire axis along the (111) direction. The dot length is set to $L = 4\sqrt{3}a$, and the radius is $R = 3a$. The arrows indicate the two levels whose spin texture is analyzed in Figs. B.2.

Finite dot

The finite dot geometry is then defined by setting the length of the nanowire along the (111) direction to a given value L. To maintain the aspect ratio of the cylindrical dot studied numerically in Sec. 2.5.1, we set $R = 3a$ and $L = 4\sqrt{3}a$. This corresponds to a cluster of 1592 sites, which is a small enough size to keep a reasonable computational cost of the calculations while still allowing for a meaningful comparison of the spin texture with the results of Sec. 2.5.1 and Sec. 3.

The energy levels in the finite dot geometry are shown in Fig. B.1 (triangles) along with the infinitely long nanowire band-structure for better comparison, where we again focus on states energetically inside the bulk gap. As expected, both the bands of the infinite wire and all dot levels are twofold Kramer's degenerate. For the chosen parameter set, we find two subgap states appearing inside the surface gap Δ_s. (Since there is no full rotational symmetry any more, we cannot classify states by j here.)

To get an idea of the spin texture of the dot states, we now focus on the two states indicated by arrows in Fig. B.1. The lower arrow corresponds to a subgap state, and the second one refers to the lowest-lying state within the conduction band of the infinite wire. The corresponding spin densities are shown in Fig. B.2. As in the effective low-energy

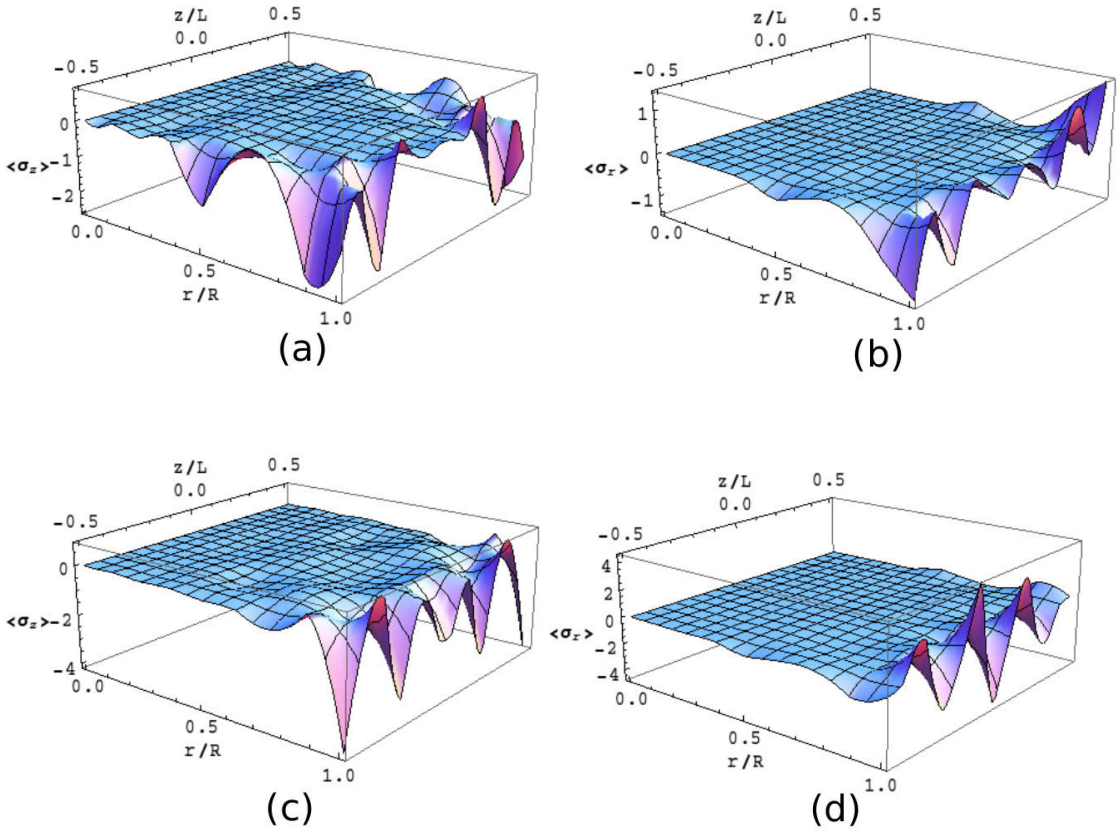

Figure B.2: Spin texture in the rz plane obtained from the tight-binding model Eq. (B.1). (a) and (b) shows the spin densities $\langle\sigma_z\rangle$ and $\langle\sigma_r\rangle$ [(b)] are shown for the subgap state indicated by the lower arrow in Fig. B.1. (c) and (d) shows the same for the state indicated by upper arrow in Fig. B.1.

theory and the surface Dirac fermion description, we again observe $\langle\sigma_\phi\rangle = 0$, and therefore only $\langle\sigma_z\rangle$ and $\langle\sigma_r\rangle$ are shown.

The subgap states have a charge density mostly localized near the caps of the cylindrical dot, again with out-of-plane (in-plane) spin components that are identical (oppositely directed) on both sides, reproducing the results of Secs. 2.5.1 and 3. However, unlike the continuous model, the tight-binding model predicts a spin texture with a superimposed atomic-scale oscillation. This oscillation stems from the finite $k = \pi/d_{\text{cell}}$ value at the Dirac point in this model.

On the other hand, for the lowest-lying state within the conduction band, corresponding to the "zero-momentum" state in Secs. 2.5.1 and 3, Figure B shows that the density is largest along the cylinder trunk. The spin is predominantly oriented along the negative z-direction, but with a finite oscillatory component in the radial direction that breaks

spin-surface locking.

To conclude, even though the results of the tight-binding model are not fully equivalent to the ones in Secs. 2.5.1 and 3, we find that the main properties of the subgap and lowest conduction band states are reproduced.

Appendix C

Surface Hamiltonian for infinite nanowire

Here we analytically derive Eq. (3.10) for an infinite nanowire using the gap-inversion model of Ref. 73 and discussed in Sec 3.2.

First we consider the case $k = 0$. Eq. (3.8) has two solutions ($s = \pm$):

$$\psi_j^{(s)}(r) = \chi_j^{(s)}(r) \otimes \begin{pmatrix} is\cos\gamma \\ -\text{sign}(M)\sin\gamma \end{pmatrix} , \tag{C.1}$$

where

$$\sin\gamma = \sqrt{\frac{1}{2} - \frac{\epsilon}{2M}} , \quad \cos\gamma = \sqrt{\frac{1}{2} + \frac{\epsilon}{2M}} , \tag{C.2}$$

and spinor (in spin space) $\chi_j^{(s)}(r)$ obeys:

$$\left[-i\left(\partial_r + \frac{1}{2r}\right)\sigma_x + \frac{j}{r}\sigma_y\right]\chi_j^{(s)} = is\kappa\chi_j^{(s)} , \quad \kappa = \sqrt{\mathcal{M}^2 - \epsilon^2}/v_2 . \tag{C.3}$$

Explicitly:

$$\chi_j^{(s)}(r < R) = \begin{pmatrix} I_{j-1/2}(\kappa r) \\ -sI_{j+1/2}(\kappa r) \end{pmatrix} , \quad \chi_j^{(s)}(r > R) = \begin{pmatrix} K_{j-1/2}(\kappa r) \\ sK_{j+1/2}(\kappa r) \end{pmatrix} , \tag{C.4}$$

where I_ν and K_ν are the modified Bessel functions with integer $\nu = j \pm 1/2$. [i] The full solution to Eq. (3.8) for $k = 0$ is given by

$$\begin{aligned} \psi_j(r) &= \Theta(R-r)\left[\alpha_1\psi_j^{(+)}(r) + \beta_1\psi_j^{(-)}(r)\right] \\ &\quad + \Theta(r-R)\left[\alpha_2\psi_j^{(+)}(r) + \beta_2\psi_j^{(-)}(r)\right] , \end{aligned} \tag{C.5}$$

[i] For large x, $I_\nu(x)$ and $K_\nu(x)$ are exponentially growing and decaying functions, respectively. For $x \to 0$, $I_\nu(x)$ remains finite, while $K_\nu(x)$ is divergent.

where coefficients $\alpha_{1,2}$ and $\beta_{1,2}$ are obtained by requiring continuity of the wave function at $r = R$. This results in a linear system of equations for the coefficients:

$$\begin{aligned}
&\alpha_1 \begin{pmatrix} I_{j-1/2} \\ -I_{j+1/2} \end{pmatrix} \otimes \begin{pmatrix} i\cos\gamma \\ -\sin\gamma \end{pmatrix} + \beta_1 \begin{pmatrix} I_{j-1/2} \\ I_{j+1/2} \end{pmatrix} \otimes \begin{pmatrix} -i\cos\gamma \\ -\sin\gamma \end{pmatrix} \\
&= \alpha_2 \begin{pmatrix} K_{j-1/2} \\ K_{j+1/2} \end{pmatrix} \otimes \begin{pmatrix} i\sin\gamma \\ \cos\gamma \end{pmatrix} + \beta_2 \begin{pmatrix} K_{j-1/2} \\ -K_{j+1/2} \end{pmatrix} \otimes \begin{pmatrix} -i\sin\gamma \\ \cos\gamma \end{pmatrix} , \qquad \text{(C.6)}
\end{aligned}$$

where (from now on) γ is determined through Eq. (C.2) with $M \to \mathcal{M} > 0$, $I_\nu \equiv I_\nu(\kappa R)$, and similarly for K_ν. Equating to zero the determinant of the system (C.6) leads to a dispersion equation:

$$\begin{aligned}
&\Big(\cos^2\gamma\, I_{j-1/2}K_{j+1/2} - \sin^2\gamma\, I_{j+1/2}K_{j-1/2}\Big) \\
&\qquad \times \Big(\sin^2\gamma\, I_{j-1/2}K_{j+1/2} - \cos^2\gamma\, I_{j+1/2}K_{j-1/2}\Big) = 0 , \qquad \text{(C.7)}
\end{aligned}$$

or equivalently [cf. Ref. 73]:

$$\Big(I_{j-1/2}K_{j+1/2} + I_{j+1/2}K_{j-1/2}\Big)^2 - \frac{4\mathcal{M}^2}{v_2^2\kappa^2}\, I_{j-1/2}I_{j+1/2}K_{j-1/2}K_{j+1/2} = 0 . \qquad \text{(C.8)}$$

Assuming $\kappa R \gg 1$ and using the asymptotic forms for the Bessel functions,

$$\begin{aligned}
I_\nu(x) &\approx \frac{e^x}{\sqrt{2\pi x}} \left[1 - \frac{4\nu^2 - 1}{8x} + ...\right] , \\
K_\nu(x) &\approx \sqrt{\frac{\pi}{2x}}\, e^{-x} \left[1 + \frac{4\nu^2 - 1}{8x} + ...\right] , \qquad \text{(C.9)}
\end{aligned}$$

in particular (for $s = \pm$),

$$I_{j-s/2}(x)K_{j+s/2}(x) \approx \frac{1}{2x}\left(1 + s\,\frac{j}{x}\right) , \qquad \text{(C.10)}$$

one finds from the dispersion equation (C.7):

$$\cos(2\gamma) \approx \pm\frac{j}{\kappa R} \quad \Rightarrow \quad \epsilon \approx \pm j v_2/R , \quad \kappa \approx \mathcal{M}/v_2 . \qquad \text{(C.11)}$$

Thus, for given j and $k = 0$, there are two energy levels: $\epsilon_{s=\pm} = s j v_2/R$. The corresponding wave functions $\psi_{j,s}(r)$, with the coefficients $\alpha_{1,2}$, $\beta_{1,2}$ determined from Eq. (C.6), are given by:

$$\begin{aligned}
\psi_{j,s}(r < R) &= \alpha_1 \Bigg[\begin{pmatrix} I_{j-1/2}(\kappa r) \\ -I_{j+1/2}(\kappa r) \end{pmatrix} \otimes \begin{pmatrix} i\cos\gamma \\ -\sin\gamma \end{pmatrix} \\
&\qquad + s \begin{pmatrix} I_{j-1/2}(\kappa r) \\ I_{j+1/2}(\kappa r) \end{pmatrix} \otimes \begin{pmatrix} -i\cos\gamma \\ -\sin\gamma \end{pmatrix} \Bigg] , \qquad \text{(C.12)}
\end{aligned}$$

	τ_0	τ_x	τ_y	τ_z
σ_0	$\hat{\gamma}_0$	0	$\hat{\gamma}_x$	0
σ_x	$-\hat{\gamma}_x$	0	$-\hat{\gamma}_0$	0
σ_y	0	$\hat{\gamma}_z$	0	$\hat{\gamma}_y$
σ_z	0	$\hat{\gamma}_y$	0	$-\hat{\gamma}_z$

Table C.1: Representation of spin-parity matrices in terms of Pauli matrices $\hat{\gamma}_i$ acting in surface-state subspace.

$$\begin{aligned}\psi_{j,s}(r>R) &= \alpha_2\Bigg[\begin{pmatrix} K_{j-1/2}(\kappa r) \\ K_{j+1/2}(\kappa r)\end{pmatrix}\otimes\begin{pmatrix} i\sin\gamma \\ \cos\gamma\end{pmatrix} \\ &\quad +s\begin{pmatrix} K_{j-1/2}(\kappa r) \\ -K_{j+1/2}(\kappa r)\end{pmatrix}\otimes\begin{pmatrix} -i\sin\gamma \\ \cos\gamma\end{pmatrix}\Bigg] , \end{aligned} \tag{C.13}$$

where α_1 and α_2 are related by $\alpha_1/\alpha_2 \approx -s\pi e^{-2\kappa R}$. For $\psi_{j,s}(r)$ normalized in radial direction,

$$\int_0^{+\infty} dr\, r\,|\psi_{j,s}(r)|^2 = 1 , \tag{C.14}$$

using the asymptotic forms (C.9) in the leading order,

$$\int_0^R dr\, rI_\nu(\kappa r)I_\mu(\kappa r) \approx \frac{e^{2\kappa R}}{4\pi\kappa^2} , \quad \int_R^{+\infty} dr\, rK_\nu(\kappa r)K_\mu(\kappa r) \approx \frac{\pi}{4\kappa^2}\, e^{-2\kappa R} , \tag{C.15}$$

one obtains ($s=\pm$):

$$\alpha_1 = \sqrt{\frac{\pi}{2}}\,\kappa\, e^{-\kappa R} , \quad \alpha_2 = -s\frac{\kappa}{\sqrt{2\pi}}\, e^{\kappa R} . \tag{C.16}$$

For small $k \neq 0$, a surface Hamiltonian is obtained by projecting the bulk Hamiltonian (3.6) onto the subspace of the zero-momentum states (C.12)-(C.13). As a result, one finds for the truncated Hamiltonian:

$$h_j = \frac{jv_2}{R}\,\rho_z + v_1 k\,\rho_y , \tag{C.17}$$

where ρ_i are the Pauli matrices in the zero-momentum subspace. Similarly, in the leading asymptotic approximation (C.15), one can easily calculate all spin-parity matrices, which results in a representation of the Dirac matrices $\sigma_\mu \otimes \tau_\nu$ in the truncated basis. In the limit $R \to \infty$, these combinations and are shown in the above table.

Appendix D

Linearised Boltzmann equation

The linearized Boltzmann equation has been derived for closely related problems before,[81,82,91,100] and we here follow those works and briefly sketch the derivation of Eq. (4.28).

Let $f(\mathbf{r}, \mathbf{k}, t)$ denote the distribution function which gives the occupation probability of the state $|\mathbf{k}\rangle$ by an electron in a volume $d\mathbf{r}$ at position $\mathbf{r}$ and time t. The quasiclassical Boltzmann theory gives:

$$\frac{\partial f}{\partial t} + \mathbf{v}_\mathbf{k} \cdot \frac{\partial f}{\partial \mathbf{r}} + \mathbf{F} \cdot \frac{\partial f}{\partial \mathbf{k}} = I_c[f], \tag{D.1}$$

where $\mathbf{v}_\mathbf{k} = \nabla_\mathbf{k} \epsilon_\mathbf{k}$ is the electron velocity and $\mathbf{F} = -e\mathbf{E}$ the force due to the externally applied electric field. We omit in this subsection the τ and s indexes. The collision integral $I_c[f]$ is given by:

$$I_c[f] = \sum_{\mathbf{k}'} \left[W_{\mathbf{k}' \to \mathbf{k}} f(\mathbf{r}, \mathbf{k}', t)(1 - f(\mathbf{r}, \mathbf{k}, t)) - W_{\mathbf{k} \to \mathbf{k}'} f(\mathbf{r}, \mathbf{k}, t)(1 - f(\mathbf{r}, \mathbf{k}', t)) \right] \tag{D.2}$$

where $W_{\mathbf{k} \to \mathbf{k}'}$ is the transition probability density. For a uniform electric field in a homogeneous system, the Boltzmann equation in the steady state becomes:

$$\mathbf{F} \cdot \frac{\partial f}{\partial \mathbf{k}} = I_c[f] \tag{D.3}$$

In the absence of perturbing field, the distribution function must be the Fermi-Dirac function $f_0 = n_F$. In this case the collision term must vanish and the principle of detailed balance gives for all $\mathbf{k}$ and $\mathbf{k}'$:

$$W_{\mathbf{k}' \to \mathbf{k}} n_F(\epsilon_{\mathbf{k}'})(1 - n_F(\epsilon_\mathbf{k})) = W_{\mathbf{k} \to \mathbf{k}'} n_F(\epsilon_\mathbf{k})(1 - n_F(\epsilon_{\mathbf{k}'})) \tag{D.4}$$

In the presence of an electric field, the distribution function f experiences an axially symmetric perturbation which is biased towards the field direction and f may be expanded in terms of Legendre polynomials. For low electric fields we need only keep the first two

terms of the series so that $f_{\mathbf{k}} = n_F(\epsilon_{\mathbf{k}}) + \cos\alpha f_1(\epsilon_{\mathbf{k}})$, where α is the angle between $\mathbf{k}$ and $\mathbf{F}$. Keeping only the terms linear in $\mathbf{F}$ and using the principle of detailed balance, we get:

$$\mathbf{F}\cdot\mathbf{v}_{\mathbf{k}}\frac{\partial n_F}{\partial\epsilon} = \sum_{\mathbf{k}'} W_{\mathbf{k}\to\mathbf{k}'}\left[\frac{n_F(\epsilon_{\mathbf{k}})}{n_F(\epsilon_{\mathbf{k}'})}\cos\alpha' f_1(\epsilon'_{\mathbf{k}}) - \frac{1-n_F(\epsilon_{\mathbf{k}'})}{1-n_F(\epsilon_{\mathbf{k}})}\cos\alpha f_1(\epsilon_{\mathbf{k}})\right] \tag{D.5}$$

Looking for the solution in the following form:

$$f_1(\epsilon_{\mathbf{k}}) = -\tau(\epsilon_{\mathbf{k}})Fv_{\mathbf{k}}\frac{\partial n_F}{\partial\epsilon} = \tau(\epsilon_{\mathbf{k}})\beta F v_{\mathbf{k}} n_F(\epsilon_{\mathbf{k}})(1-n_F(\epsilon_{\mathbf{k}})), \tag{D.6}$$

with $v_{\mathbf{k}} = \mathbf{v}_{\mathbf{k}}\cdot\mathbf{k}/k$, we arrive at the linearized Boltzmann equation:

$$\frac{1}{\tau(\epsilon_{\mathbf{k}})} = \sum_{\mathbf{k}'} W_{\mathbf{k}\to\mathbf{k}'}\left[1 - \frac{v_{\mathbf{k}'}}{v_{\mathbf{k}}}\frac{\tau(\epsilon_{\mathbf{k}'})}{\tau(\epsilon_{\mathbf{k}})}\frac{\cos\alpha'}{\cos\alpha}\right]\frac{1-n_F(\epsilon_{\mathbf{k}'})}{1-n_F(\epsilon_{\mathbf{k}})} \tag{D.7}$$

Considering the coordinate system where $\mathbf{k} = (0,0,k)$, $\mathbf{F} = (0, F\sin\alpha, F\cos\alpha)$ and denoting by (θ,φ) the spherical angles of $\mathbf{k}'$, we find that $\cos\alpha'/\cos\alpha = \tan\alpha\sin\theta\sin\varphi + \cos\theta$. Integration over φ makes the first term to vanish and we finally get:

$$\frac{1}{\tau(\epsilon_{\mathbf{k}})} = \sum_{\mathbf{k}'} W_{\mathbf{k}\to\mathbf{k}'}\left[1 - \frac{v_{\mathbf{k}'}}{v_{\mathbf{k}}}\frac{\tau(\epsilon_{\mathbf{k}'})}{\tau(\epsilon_{\mathbf{k}})}\cos\theta\right]\frac{1-n_F(\epsilon_{\mathbf{k}'})}{1-n_F(\epsilon_{\mathbf{k}})} \tag{D.8}$$

where θ is the angle between $\mathbf{k}$ and $\mathbf{k}'$. This equation is a linear integral equation for $\tau(\epsilon_{\mathbf{k}})$ which must be solved numerically in the general case. The solution may be interpreted as the electron momentum relaxation time since from Eqs. (D.5) and (D.6), the collision integral can be written in the form:

$$I_c[f] = -\frac{f-n_F}{\tau(\epsilon_{\mathbf{k}})} \tag{D.9}$$

and $\tau(\epsilon_{\mathbf{k}})$ is the characteristic time in which the distribution f returns to its equilibrium form n_F in the absence of the external field $\mathbf{F}$.

In the case of elastic scattering process $\epsilon_{\mathbf{k}} = \epsilon_{\mathbf{k}'}$, we get the simple closed-form expression for $\tau(\epsilon_{\mathbf{k}})$:

$$\frac{1}{\tau(\epsilon_{\mathbf{k}})} = \sum_{\mathbf{k}'} W_{\mathbf{k}\to\mathbf{k}'}(1-\cos\theta) \tag{D.10}$$

Since the scattering of electrons from acoustic phonons may be considered quasielastic $\Omega^{(\lambda)}_{q,n} \ll \mu$, the usual approximation leading to a closed-form expression for the momentum relaxation time and which have been used for instance in graphene,[81] consists in setting $\tau(\epsilon_{\mathbf{k}'}) = \tau(\epsilon_{\mathbf{k}})$ on the right-hand side of the integral equation, so that:

$$\frac{1}{\tau(\epsilon_{\mathbf{k}})} = \sum_{\mathbf{k}'} W_{\mathbf{k}\to\mathbf{k}'}\left[1 - \frac{v_{\mathbf{k}'}}{v_{\mathbf{k}}}\cos\theta\right]\frac{1-n_F(\epsilon_{\mathbf{k}'})}{1-n_F(\epsilon_{\mathbf{k}})}. \tag{D.11}$$

Note that this approximation is equivalent to the test particle approximation used in 91. Notice that in graphene the modulus of the velocity is independent of wave vector

and only intraband transitions have been considered[81] so that the bracket reduces to $[1-\cos\theta]$. It is also the case for TI in the semi-infinite geometry.[87]

The curent density is then given by:

$$\mathbf{j} = -\frac{e}{\mathcal{A}} \sum_{\mathbf{k}} \mathbf{v}_{\mathbf{k}} f(\mathbf{k}) \tag{D.12}$$

Using Eq. (D.6), if the electric field is along the z-axis, we find:

$$j_z = \frac{e^2 E_z \beta}{\mathcal{A}} \sum_{\mathbf{k}} v_{\mathbf{k}}^2 \cos^2\alpha\, \tau(\epsilon_{\mathbf{k}}) n_F(\epsilon_{\mathbf{k}})(1-n_F(\epsilon_{\mathbf{k}})) \tag{D.13}$$

where α is again the angle between $\mathbf{k}$ and $\mathbf{E}$. Using the fact that $v_{\mathbf{k}}$ depends only on the modulus of $\mathbf{k}$ and performing the angular integration, we get the final expression (4.28) for the phonon contribution to the resistivity:

$$\frac{1}{\rho} = \frac{e^2\beta}{2} \int \frac{d\mathbf{k}}{(2\pi)^2}\, v_{\mathbf{k}}^2 \tau(\epsilon_{\mathbf{k}})[-\partial_\epsilon n_F(\epsilon_{\mathbf{k}})], \tag{D.14}$$

where we have used the relation $n_F(\epsilon_{\mathbf{k}})(1-n_F(\epsilon_{\mathbf{k}})) = -\partial_\epsilon n_F(\epsilon_{\mathbf{k}})$.

Appendix E

Eliashberg Function of TI Film

We here mention the analytical result for the full transport Eliashberg function $\mathcal{F}$ defined in Eq. (4.33). Some straightforward yet tedious algebra allows to perform the θ-integration. We find the (lengthy) result

$$\begin{aligned}
\mathcal{F}^{(\nu)}_{k,n,s}(q) &= \frac{2\left|A^{(\nu)}_{k,q,n,s}\right|}{\pi(A_2W)^2}\frac{\Theta\left(Q^{(\nu)}_{k,q,n,s}+k-q\right)\Theta\left(q-\left|Q^{(\nu)}_{k,q,n,s}-k\right|\right)}{\left[\left(q^2-(Q^{(\nu)}_{k,q,n,s}-k)^2\right)\left((Q^{(\nu)}_{k,q,n,s}+k)^2-q^2\right)\right]^{1/2}} \\
&\times \Theta\left(\left|A^{(\nu)}_{k,q,n,s}\right|-\Delta/2\right)\sum_{s'}\Theta\left(s'A^{(\nu)}_{k,q,n,s}\right)\left|M^{s',s}_{\mathbf{k},\mathbf{q},n}\right|^2\Big|_{\theta_0} \\
&\times \left[1-\left(1-\frac{\nu\Omega_{q,n}}{A^{(\nu)}_{k,q,n,s}}\right)\frac{\left(Q^{(\nu)}_{k,q,n,s}\right)^2+k^2-q^2}{2k^2}\right],
\end{aligned}$$

where we use the notations

$$\begin{aligned}
A^{(\nu)}_{k,q,n,s} &= s\sqrt{(\Delta/2)^2+(A_2Wk)^2}+\nu\Omega_{q,n}, \\
Q^{(\nu)}_{k,q,n,s} &= \frac{\sqrt{\left(A^{(\nu)}_{k,q,n,s}\right)^2-(\Delta/2)^2}}{A_2W},
\end{aligned}$$

and the polar angle $\theta=\theta_0\in[0,\pi]$ follows from

$$\sqrt{k^2+q^2+2kq\cos\theta_0}=Q^{(\nu)}_{k,q,n,s},$$

fixing the polar angle between $\mathbf{k}$ and $\mathbf{q}$ in the matrix element M.

Appendix F

Bogoliubov - de Gennes (BdG) Hamiltonian:

The BCS (named after John Bardeen, Leon N. Cooper, John R. Schrieffer) hamiltonian decribing attractively interacting elctron system is

$$H = \sum_{\mathbf{k}} \epsilon_{\mathbf{k}} \hat{n}_{\mathbf{k}\sigma} - \frac{g}{L^d} \sum_{\mathbf{k},\mathbf{k}',\mathbf{q}} c^{\dagger}_{\mathbf{k}+\mathbf{q}\uparrow} c^{\dagger}_{-\mathbf{k}\downarrow} c_{-\mathbf{k}'+\mathbf{q}\downarrow} c_{\mathbf{k}'\uparrow}, \tag{F.1}$$

where g is a positive constant. Here $\mathbf{k}, \mathbf{k}'$ lives very close to the Fermi surfae and $\mathbf{q}$ should be such that, when added to a momentum $\mathbf{k}$, the final state $\mathbf{k}'$ should also live close to the Fermi surface as shown in the figure below. The phenomenon of superconductivity is explained by development of an instability towards pair binding (between electron with opposite spin and opposite momentum, or 'Cooper pair'), or "condensation" in these systems below a critical temperature. Let us assume that the ground state of the system is characterised by the presence of a macroscopic number of Cooper pairs. More specifically, let us assume that the operator $\sum_{\mathbf{k}} c_{-\mathbf{k}\downarrow} c_{\mathbf{k}\uparrow}$ acquires a non-vanishing ground state expectation value,

$$\Delta = \frac{g}{L^d} \langle GS | c_{-\mathbf{k}\downarrow} c_{\mathbf{k}\uparrow} | GS \rangle. \tag{F.2}$$

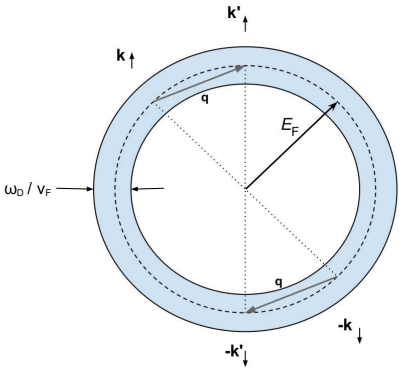

Figure F.1: scattering by q near the Fermi surface of superconductor

Now, we can substite

$$\sum_{\mathbf{k}} c_{-\mathbf{k}+\mathbf{q}\downarrow} c_{\mathbf{k}\uparrow} = \frac{g\Delta}{L^d} + \left(\sum_{\mathbf{k}} c_{-\mathbf{k}+\mathbf{q}\downarrow} c_{\mathbf{k}\uparrow} - \frac{g\Delta}{L^d} \right)$$

in the BCS Hamiltonian and retain only bilinear electron operator terms considering the term inside the braket in the above equation is very small in the ground state. Adding

the chemical potential we get the "mean-field" Hamiltonian:

$$H - \mu N \simeq \sum_{\mathbf{k}} \left[\epsilon_{\mathbf{k}} \hat{n}_{\mathbf{k}\sigma} - \left(\bar{\Delta} c_{-\mathbf{k}\downarrow} c_{\mathbf{k}\uparrow} + \Delta c^{\dagger}_{\mathbf{k}\uparrow} c^{\dagger}_{-\mathbf{k}\downarrow} \right) \right] + \frac{g|\Delta|^2}{L^d}, \tag{F.3}$$

known as the Bogoliubov - de Gennes (BdG) Hamiltonian, (or Bogoliubov - Gor'kov Hamiltonian). In the **Nambu Spinor** representation, with $\Psi_{\mathbf{k}} = (c_{\mathbf{k}\uparrow}, c^{\dagger}_{-\mathbf{k}\downarrow})$, BdG Hamiltonian looks like:

$$H - \mu N = \sum_{\mathbf{k}} \Psi^{\dagger}_{\mathbf{k}} \begin{pmatrix} \epsilon_{\mathbf{k}} & -\Delta \\ \Delta & \epsilon_{\mathbf{k}} \end{pmatrix} \Psi_{\mathbf{k}} + \sum_{\mathbf{k}} \epsilon_{\mathbf{k}} + \frac{g|\Delta|^2}{L^d}. \tag{F.4}$$

This bilinear Hamiltonian can be diagonalised with the unitary transformation

$$\begin{pmatrix} \alpha_{\mathbf{k}\uparrow} \\ \alpha^{\dagger}_{-\mathbf{k}\downarrow} \end{pmatrix} = \begin{pmatrix} \cos(\theta_{\mathbf{k}}) & \sin(\theta_{\mathbf{k}}) \\ \sin(\theta_{\mathbf{k}}) & -\cos(\theta_{\mathbf{k}}) \end{pmatrix} \begin{pmatrix} c_{\mathbf{k}\uparrow} \\ c^{\dagger}_{-\mathbf{k}\downarrow} \end{pmatrix}, \tag{F.5}$$

and with the excitation energy

$$\xi_{\mathbf{k}} = (\Delta^2 + \epsilon^2_{\mathbf{k}})^{1/2} \tag{F.6}$$

to have the diagonalised Hamiltonian:

$$H - \mu N = \sum_{\mathbf{k}\sigma} \xi_{\mathbf{k}} \alpha^{\dagger}_{\mathbf{k}\sigma} \alpha_{\mathbf{k}\sigma} + \sum_{\mathbf{k}} (\epsilon_{\mathbf{k}} - \xi_{\mathbf{k}}) + \frac{g|\Delta|^2}{L^d}. \tag{F.7}$$

Equation F.6 shows that tha elementary excitation in a BCS superconductor (known as the Bogoloubov quasi-particles) have a minimum energy Δ, known as the **energy gap**.

Appendix G

Solution for BdG equation in Graphene:

As discussed in Sec. 6.2, because of the pseudo spin and valley degeneracies present in graphene, it suffices to use a four dimensional version of the Dirac-Boguliobov-de Gennes equation (Eq. (6.15)) for electrons and holes which is given by

$$\begin{pmatrix} \vec{k}.\vec{\sigma} - U & e^{i\phi}\Delta \\ e^{-i\phi}\Delta^* & -(\vec{k}.\vec{\sigma} - U) \end{pmatrix} \begin{pmatrix} u \\ v \end{pmatrix} = \epsilon \begin{pmatrix} u \\ v \end{pmatrix} \tag{G.1}$$

where, $U = U(\mathbf{r}) + E_F$, and the energy ϵ is measured from the Fermi level of the superconductor. We assume that $U(\mathbf{r}) = 0$ in the normal graphene region and $U(\mathbf{r}) = U_0$, a constant, independent of $\mathbf{r}$ in the proximity induced superconducting region. Note that we have defined dimensionless variables

$$\begin{aligned} x \Rightarrow \frac{xE_F}{\hbar v_F}, \quad y \Rightarrow \frac{yE_F}{\hbar v_F}, \quad k_y \Rightarrow \frac{\hbar v_F k_y}{E_F}, \\ \Delta \Rightarrow \frac{\Delta}{E_F}, \quad \epsilon \Rightarrow \frac{\epsilon}{E_F} \quad \text{and} \quad U \Rightarrow \frac{U}{E_F} \end{aligned} \tag{G.2}$$

to replace the original ones. The solution of the DBDG equations,[158] describing electrons and holes with incident energy ϵ inside the normal graphene regions ($\Delta = 0$), can be written as

$$\Psi^{e\pm} = \frac{e^{ik_y y \pm ikx}}{\sqrt{\cos\alpha}} \begin{pmatrix} e^{\mp i\alpha/2} \\ \pm e^{\pm i\alpha/2} \\ 0 \\ 0 \end{pmatrix} \tag{G.3}$$

$$\Psi^{h\pm} = \frac{e^{ik_y y \pm ik'x}}{\sqrt{\cos\alpha'}} \begin{pmatrix} 0 \\ 0 \\ e^{\mp i\alpha'/2} \\ \mp e^{\pm i\alpha'/2} \end{pmatrix} \tag{G.4}$$

where $\alpha = \sin^{-1}[k_y/(\epsilon+1)]$, $\alpha' = \sin^{-1}[k_y/(\epsilon-1)], k = \sqrt{(\epsilon+1)^2 - k_y^2}$ and $k' = \sqrt{(\epsilon-1)^2 - k_y^2}$. α is the angle of incidence of the incoming electron (with wave-vector (k, k_y)) and α' is the angle of reflection of the Andreev reflected hole (with wave-vector $(-k', k_y)$). For retro AR, α' have opposite sign from α whereas for SAR, they have the same signs. The change from retro ($\epsilon < 1$) to SAR ($\epsilon > 1$) occurs at $\epsilon = 1$ (in our dimensionless units).

Similarly for the superconducting barrier regions, the four component spinor solutions (u, v) contain electron wave-functions u of one valley and hole wave-functions v of the other valley. The DBDG equation can now be solved for any arbitrary energy ϵ and the four solutions inside the superconducting barriers are given in the preprint version of Ref. 158,

$$\psi_{1/2} = e^{ik_y y \pm x\sqrt{k_y^2 - (U + \sqrt{(\epsilon^2 - \Delta^2)})^2}} \begin{pmatrix} e^{i\beta} \\ \pm e^{i\beta \pm i\gamma_1} \\ e^{-i\phi} \\ \pm e^{-i\phi \pm i\gamma_1} \end{pmatrix} \tag{G.5}$$

$$\psi_{3/4} = e^{ik_y y \pm x\sqrt{k_y^2 - (U - \sqrt{(\epsilon^2 - \Delta^2)})^2}} \begin{pmatrix} e^{-i\beta} \\ \pm e^{-i\beta \pm i\gamma_2} \\ e^{-i\phi} \\ \pm e^{-i\phi \pm i\gamma_2} \end{pmatrix} \tag{G.6}$$

where the subscripts 1/2 refers to the upper and lower signs on the RHS respectively, and similarly for 3/4 and

$$\begin{aligned} \gamma_1 &= \sin^{-1}\left(\frac{k_y}{U + \sqrt{(\epsilon^2 - \Delta^2)}}\right) \\ \gamma_2 &= \sin^{-1}\left(\frac{k_y}{U - \sqrt{(\epsilon^2 - \Delta^2)}}\right) \end{aligned} \tag{G.7}$$

and

$$\begin{aligned} \beta &= \cos^{-1}\frac{\epsilon}{\Delta} \quad if \quad \epsilon < \Delta \\ &= -i\cosh^{-1}\frac{\epsilon}{\Delta} \quad if \quad \epsilon > \Delta\ . \end{aligned} \tag{G.8}$$

Here, we have not taken the limit $U \gg \Delta, \epsilon$. We have also obtained the solution for both right-moving and left-moving electrons and holes.

Bibliography

[1] M. König, et al., *Journal of the Physical Society of Japan* **77**, 031007 (2008).

[2] J. E. Moore, *Nature* **464**, 194 (2010).

[3] M. Hasan, C. Kane, *Reviews of Modern Physics* **82**, 3045 (2010).

[4] F. Bloch, *Zeitschrift für Physik* **52**, 555 (1929).

[5] K. Klitzing, G. Dorda, M. Pepper, *Physical Review Letters* **45**, 494 (1980).

[6] R. E. Prange, S. M. Girvin, *The Quantum Hall Effect*. Springer, New York (1987).

[7] D. Xiao, M.-C. Chang, Q. Niu, *Reviews of Modern Physics* **82**, 1959 (2010).

[8] D. Thouless, M. Kohmoto, M. Nightingale, M. den Nijs, *Physical Review Letters* **49**, 405 (1982).

[9] M. Nakahara, *Geometry, Topology and Physics*. Hilger, Bristol (1990).

[10] M. V. Berry, *Proceedings of the Royal Society A: Mathematical, Physical and Engineering Sciences* **392**, 45 (1984).

[11] B. Halperin, *Physical Review B* **25**, 2185 (1982).

[12] R. Jackiw, C. Rebbi, *Physical Review D* **13**, 3398 (1976).

[13] C. L. Kane, E. J. Mele, *Physical Review Letters* **95**, 226801 (2005).

[14] B. A. Bernevig, T. L. Hughes, S.-C. Zhang, *Science* **314**, 1757 (2006).

[15] B. A. Bernevig, S.-C. Zhang, *Physical Review Letters* **96**, 106802 (2006).

[16] M. Konig, et al., *Science* **318**, 766 (2007).

[17] A. Roth, et al., *Science (New York, N.Y.)* **325**, 294 (2009).

[18] R. Dornhaus, G. Nimitz, *Narrow Gap Semiconductors*. Springer, Berlin (1983).

[19] M.-C. Chang, Q. Niu, *Journal of Physics: Condensed Matter* **20**, 193202 (2008).

[20] D. Culcer, Y. Yao, Q. Niu, *Physical Review B* **72**, 085110 (2005).

[21] R. Shindou, K. I. Imura, *Nuclear Physics B* **720**, 399 (2005).

[22] C. L. Kane, E. J. Mele, *Physical Review Letters* **95**, 146802 (2005).

[23] L. Fu, C. Kane, *Physical Review B* **74**, 195312 (2006).

[24] T. Fukui, Y. Hatsugai, *Journal of the Physical Society of Japan* **76**, 053702 (2007).

[25] T. Fukui, T. Fujiwara, Y. Hatsugai, *Journal of the Physical Society of Japan* **77**, 123705 (2008).

[26] J. Moore, L. Balents, *Physical Review B* **75**, 121306(R) (2007).

[27] X.-L. Qi, T. L. Hughes, S.-C. Zhang, *Physical Review B* **78**, 195424 (2008).

[28] R. Roy, *Physical Review B* **79**, 195321 (2009).

[29] Z. Wang, X.-L. Qi, S.-C. Zhang, *New Journal of Physics* **12**, 065007 (2010).

[30] D. Sheng, Z. Weng, L. Sheng, F. Haldane, *Physical Review Letters* **97**, 036808 (2006).

[31] M. Kohmoto, B. Halperin, Y.-S. Wu, *Physical Review B* **45**, 13488 (1992).

[32] C. Wu, B. A. Bernevig, S.-C. Zhang, *Physical Review Letters* **96**, 106401 (2006).

[33] K. S. Novoselov, et al., *Nature* **438**, 197 (2005).

[34] K. S. Novoselov, et al., *Science (New York, N.Y.)* **306**, 666 (2004).

[35] Y. Zhang, Y.-W. Tan, H. L. Stormer, P. Kim, *Nature* **438**, 201 (2005).

[36] P. Wallace, *Physical Review* **71**, 622 (1947).

[37] S. Reich, J. Maultzsch, C. Thomsen, P. Ordejón, *Physical Review B* **66** (2002).

[38] G. W. Semenoff, *Phys. Rev. Lett.* **53**, 2449 (1984).

[39] A. H. Castro Neto, N. M. R. Peres, K. S. Novoselov, A. K. Geim, *Reviews of Modern Physics* **81**, 109 (2009).

[40] M. I. Katsnelson, K. S. Novoselov, a. K. Geim, *Nature Physics* **2**, 620 (2006).

[41] M. I. Katsnelson, *Materials Today* **10**, 20 (2007).

[42] T. Ando, T. Nakanishi, R. Saito, *Journal of the Physics Society Japan* **67**, 2857 (1998).

[43] P. McEuen, M. Bockrath, D. Cobden, Y.-G. Yoon, S. Louie, *Physical Review Letters* **83**, 5098 (1999).

[44] A. Calogeracos, N. Dombey, *Contemporary Physics* **40**(5), 313 (1999).

[45] C. Itzykson, J.-B. Zuber, *Quantum Field Theory*. Dover, New York (2006).

[46] V. Cheianov, *Physical Review B* **74**, 041403(R) (2006).

[47] A. De Martino, L. Dell'Anna, R. Egger, *Physical Review Letters* **98**, 066802 (2007).

[48] A. De Martino, R. Egger, *Semiconductor Science and Technology* **25**, 034006 (2010).

[49] L. Fu, C. Kane, *Physical Review B* **76**, 045302 (2007).

[50] D. Hsieh, et al., *Nature* **452**, 970 (2008).

[51] H. Zhang, et al., *Nature Physics* **5**, 438 (2009).

[52] Y. Xia, et al., *Nature Physics* **5**, 398 (2009).

[53] Y. L. Chen, et al., *Science (New York, N.Y.)* **325**, 178 (2009).

[54] D.-X. Qu, Y. S. Hor, J. Xiong, R. J. Cava, N. P. Ong, *Science (New York, N.Y.)* **329**, 821 (2010).

[55] J. Checkelsky, Y. Hor, R. Cava, N. Ong, *Physical Review Letters* **106**, 196801 (2011).

[56] H. Peng, et al., *Nat. Mater.* **9**, 225 (2010).

[57] J. J. Cha, et al., *Nano letters* **10**, 1076 (2010).

[58] Y. M. Zuev, J. S. Lee, C. Galloy, H. Park, P. Kim, *Nano letters* **10**, 3037 (2010).

[59] H. Tang, D. Liang, R. L. J. Qiu, X. P. A. Gao, *ACS nano* **5**, 7510 (2011).

[60] J. P. Perdew, K. Burke, M. Ernzerhof, *Physical Review Letters* **77**, 3865 (1996).

[61] J. Black, E. Conwell, L. Seigle, C. Spencer, *Journal of Physics and Chemistry of Solids* **2**, 240 (1957).

[62] E. Mooser, W. Pearson, *Physical Review* **101**, 492 (1956).

[63] C.-X. Liu, et al., *Physical Review B* **82**, 045122 (2010).

[64] W.-Y. Shan, H.-Z. Lu, S.-Q. Shen, *New Journal of Physics* **12**, 043048 (2010).

[65] Y. Zhang, Y. Ran, A. Vishwanath, *Physical Review B* **79**, 245331 (2009).

[66] R. Egger, A. Zazunov, A. Yeyati, *Physical Review Letters* **105**, 136403 (2010).

[67] J. Bardarson, P. Brouwer, J. Moore, *Physical Review Letters* **105**, 156803 (2010).

[68] Y. Zhang, A. Vishwanath, *Physical Review Letters* **105**, 206601 (2010).

[69] J. Nygå rd, D. H. Cobden, P. E. Lindelof, *Nature* **408**, 342 (2000).

[70] H. W. Postma, T. Teepen, Z. Yao, M. Grifoni, C. Dekker, *Science (New York, N.Y.)* **293**, 76 (2001).

[71] L. Fu, C. Kane, E. Mele, *Physical Review Letters* **98**, 106803 (2007).

[72] D.-H. Lee, *Physical Review Letters* **103**, 196804 (2009).

[73] V. Parente, P. Lucignano, P. Vitale, A. Tagliacozzo, F. Guinea, *Physical Review B* **83**, 075424 (2011).

[74] L. Fu, *Physical Review Letters* **103**, 266801 (2009).

[75] O. Yazyev, J. Moore, S. Louie, *Physical Review Letters* **105**, 266806 (2010).

[76] S.-y. Xu, et al. p. 5 (2011).

[77] S. Souma, et al., *Physical Review Letters* **106**, 216803 (2011).

[78] E. McCann, V. I. Fal ko, *Journal of Physics: Condensed Matter* **16**, 2371 (2004).

[79] a. Akhmerov, C. Beenakker, *Physical Review B* **77**, 085423 (2008).

[80] C.-Y. Moon, J. Han, H. Lee, H. J. Choi, *Physical Review B* **84**, 195425 (2011).

[81] E. Hwang, S. Das Sarma, *Physical Review B* **77**, 115449 (2008).

[82] E. Mariani, F. von Oppen, *Physical Review B* **82**, 195403 (2010).

[83] D. Efetov, P. Kim, *Physical Review Letters* **105**, 256805 (2010).

[84] H. K. Pal, et al., in *AIP Conf. Proc*, pp. 23–25 (2011).

[85] B. Hellsing, A. Eiguren, E. V. Chulkov, *Journal of Physics: Condensed Matter* **14**, 5959 (2002).

[86] P. Echenique, et al., *Surface Science Reports* **52**, 219 (2004).

[87] S. Giraud, *Phys. Rev. B* **83**, 245322 (2011).

[88] G. Zhang, et al., *Applied Physics Letters* **95**, 053114 (2009).

[89] J. O. Jenkins, J. A. Rayne, R. W. Ure, *Phys. Rev. B* **5**, 3171 (1972).

[90] B.-L. Huang, M. Kaviany, *Physical Review B* **77**, 125209 (2008).

[91] N. Bannov, V. Aristov, V. Mitin, M. A. Stroscio, *Phys. Rev. B* **51**, 9930 (1995).

[92] Y. M. Sirenko, K. W. Kim, M. A. Stroscio, *Phys. Rev. B* **56**, 15770 (1997).

[93] P. Thalmeier, *Phys. Rev. B* **83**, 125314 (2011).

[94] G. Shoemake, J. Rayne, R. Ure, *Physical Review* **185**, 1046 (1969).

[95] W. Richter, C. R. Becker, *Physica Status Solidi (B)* **84**, 619 (1977).

[96] J. R. Wiese, L. Muldawer, *Journal of Physics and Chemistry of Solids* **15**, 13 (1960).

[97] L. D. Landau, E. M. Lifshitz, *Elasticity Theory*. Pergamon, New York (1986).

[98] R. C. Hatch, et al., *Phys. Rev. B* **83**, 241303(R) (2011).

[99] N. W. Ashcroft, N. D. Mermin, *Solid State Physics*. Saunders College, Philadelphia (1976).

[100] T. Kawamura, S. Das Sarma, *Physical Review B* **45**, 3612 (1992).

[101] B. Seradjeh, J. E. Moore, M. Franz, *Phys. Rev. Letter* **103**, 066402 (2009).

[102] G. Y. Cho, J. E. Moore, *Phys. Rev. B* **84**, 165101 (2011).

[103] Y. Jiang, et al., *Phys. Rev. Lett.* **108**, 016401 (2012).

[104] D. Novikov, *Physical Review B* **76**, 245435 (2007).

[105] O. Gamayun, E. Gorbar, V. Gusynin, *Physical Review B* **80**, 165429 (2009).

[106] F. Peeters, A. Matulis, *Physical Review B* **48**, 15166 (1993).

[107] A. Matulis, F. Peeters, P. Vasilopoulos, *Physical Review Letters* **72**, 1518 (1994).

[108] I. Ibrahim, F. Peeters, *Physical Review B* **52**, 17321 (1995).

[109] S. Lee, *Physics Reports* **394**, 1 (2004).

[110] A. Nogaret, *Journal of physics. Condensed matter : an Institute of Physics journal* **22**, 253201 (2010).

[111] A. Tarasov, et al., *Physical Review Letters* **104**, 186801 (2010).

[112] S. Mondal, D. Sen, K. Sengupta, R. Shankar, *Physical Review B* **82**, 045120 (2010).

[113] S. Mondal, D. Sen, K. Sengupta, R. Shankar, *Physical Review Letters* **104**, 046403 (2010).

[114] T. Yokoyama, Y. Tanaka, N. Nagaosa, *Physical Review B* **81**, 121401(R) (2010).

[115] Q. Liu, C.-X. Liu, C. Xu, X.-L. Qi, S.-C. Zhang, *Physical Review Letters* **102**, 156603 (2009).

[116] R. Biswas, A. Balatsky, *Physical Review B* **81**, 233405 (2010).

[117] A. Morpurgo, F. Guinea, *Physical Review Letters* **97**, 196804 (2006).

[118] M. Fogler, F. Guinea, M. Katsnelson, *Physical Review Letters* **101**, 226804 (2008).

[119] V. Pereira, A. Castro Neto, *Physical Review Letters* **103**, 046801 (2009).

[120] W. Bao, et al., *Nature nanotechnology* **4**, 562 (2009).

[121] F. Guinea, M. I. Katsnelson, A. K. Geim, *Nature Physics* **6**, 30 (2010).

[122] M. Vozmediano, M. Katsnelson, F. Guinea, *Physics Reports* **496**, 109 (2010).

[123] M. Ramezani Masir, P. Vasilopoulos, A. Matulis, F. Peeters, *Physical Review B* **77**, 235443 (2008).

[124] L. Oroszlány, P. Rakyta, A. Kormányos, C. Lambert, J. Cserti, *Physical Review B* **77**, 081403(R) (2008).

[125] T. Ghosh, A. De Martino, W. Häusler, L. Dell'Anna, R. Egger, *Physical Review B* **77**, 081404(R) (2008).

[126] W. Häusler, A. De Martino, T. Ghosh, R. Egger, *Physical Review B* **78**, 165402 (2008).

[127] M. Tahir, K. Sabeeh, *Physical Review B* **77**, 195421 (2008).

[128] L. Dell'Anna, A. De Martino, *Physical Review B* **79**, 045420 (2009).

[129] M. Ramezani Masir, P. Vasilopoulos, F. M. Peeters, *New Journal of Physics* **11**, 095009 (2009).

[130] L. Z. Tan, C.-H. Park, S. G. Louie, *Physical Review B* **81**, 195426 (2010).

[131] A. Kormányos, P. Rakyta, L. Oroszlány, J. Cserti, *Physical Review B* **78**, 045430 (2008).

[132] M. Ramezani Masir, A. Matulis, F. Peeters, *Physical Review B* **79**, 155451 (2009).

[133] W. Häusler, R. Egger, *Physical Review B* **80**, 161402 (2009).

[134] Y. Aharonov, D. Bohm, *Physical Review* **115**, 485 (1959).

[135] S. Olariu, I. Popescu, *Reviews of Modern Physics* **57**, 339 (1985).

[136] S. Ruijsenaars, *Annals of Physics* **146**, 1 (1983).

[137] C. Hagen, *Physical Review Letters* **64**, 503 (1990).

[138] C. Hagen, *Physical Review D* **41**, 2015 (1990).

[139] C. Hagen, *Physical Review D* **52**, 2466 (1995).

[140] P. Giacconi, F. Maltoni, R. Soldati, *Physical Review D* **53**, 952 (1996).

[141] S. Sakoda, M. Omote, *Journal of Mathematical Physics* **38**, 716 (1997).

[142] R. Jackiw, A. Milstein, S.-Y. Pi, I. Terekhov, *Physical Review B* **80**, 033413 (2009).

[143] M. I. Katsnelson, *EPL (Europhysics Letters)* **89**, 17001 (2010).

[144] P. Recher, et al., *Physical Review B* **76**, 235404 (2007).

[145] S. Russo, et al., *Physical Review B* **77**, 085413 (2008).

[146] T. Fujita, M. B. A. Jalil, S. G. Tan, *Applied Physics Letters* **97**, 043508 (2010).

[147] V. P. Gusynin, S. G. Sharapov, J. P. Carbotte, *International Journal of Modern Physics B* **21**, 4611 (2007).

[148] R. G. Newton, *Scattering Theory of Waves and Particles*. Springer, New York, 2 edn. (1982).

[149] I. S. Gradshteyn, I. M. Ryzhik, *Table of Integrals, Series and Products*. Academic Press, New York (1980).

[150] J. Bolte, S. Keppeler, *Annals of Physics* **274**, 125 (1999).

[151] P. Carmier, D. Ullmo, *Physical Review B* **77**, 245413 (2008).

[152] V. D. Mur, D. Ullmo, *JETP Lett.* **51** (1990).

[153] H. B. Heersche, P. Jarillo-Herrero, J. B. Oostinga, L. M. K. Vandersypen, A. F. Morpurgo, *Nature* **446**, 56 (2007).

[154] G. Deutscher, P. G. de Gennes, *Superconductivity*, vol. 2. Marcel Dekker, New York (1969).

[155] E. L. Wolf, *Principle of Electron Tunneling Spectroscopy*. Oxford University Press (1985).

[156] A. Gilabert, *Annales de Physique* **2**, 203 (1977).

[157] A. F. Andreev, *Sov. Phys. JETP* **19** (1964).

[158] C. Beenakker, *Physical Review Letters* **97**, 067007 (2006).

[159] C. Beenakker, *Reviews of Modern Physics* **80**, 1337 (2008).

[160] A. Morpurgo, F. Beltram, *Physical Review B* **50**, 1325 (1994).

[161] J. Cayssol, *Physical Review Letters* **100**, 147001 (2008).

[162] C. Benjamin, J. Pachos, *Physical Review B* **78**, 235403 (2008).

[163] J. M. Pereira, P. Vasilopoulos, F. M. Peeters, *Applied Physics Letters* **90**, 132122 (2007).

[164] C. Bai, Y. Yang, X. Zhang, *Physica E: Low-dimensional Systems and Nanostructures* **42**, 1431 (2010).

[165] C. Beenakker, A. Akhmerov, P. Recher, J. Tworzydło, *Physical Review B* **77**, 075409 (2008).

[166] A. Kundu, S. Rao, A. Saha, *EPL (Europhysics Letters)* **88**, 57003 (2009).

[167] M. Titov, C. Beenakker, *Physical Review B* **74**, 041401(R) (2006).

[168] M. Maiti, K. Sengupta, *Physical Review B* **76**, 054513 (2007).

[169] D. Thouless, *Physical Review B* **27**, 6083 (1983).

[170] M. Büttiker, H. Thomas, A. Prêtre, *Zeitschrift für Physik B Condensed Matter* **94**, 133 (1994).

[171] P. Brouwer, *Physical Review B* **58**, R10135 (1998).

[172] M. Polianski, P. Brouwer, *Physical Review B* **64**, 075304 (2001).

[173] M. Moskalets, M. Büttiker, *Physical Review B* **66**, 205320 (2002).

[174] M. Moskalets, M. Büttiker, *Physical Review B* **69**, 205316 (2004).

[175] Y. Levinson, O. Entin-Wohlman, P. Wölfle, *Physica A: Statistical Mechanics and its Applications* **302**, 335 (2001).

[176] O. Entin-Wohlman, A. Aharony, *Physical Review B* **66**, 035329 (2002).

[177] S. Banerjee, A. Mukherjee, S. Rao, A. Saha, *Physical Review B* **75**, 153407 (2007).

[178] I. Aleiner, a. Andreev, *Physical Review Letters* **81**, 1286 (1998).

[179] P. Sharma, C. Chamon, *Physical Review B* **68**, 035321 (2003).

[180] R. Citro, N. Andrei, Q. Niu, *Physical Review B* **68**, 165312 (2003).

[181] E. Sela, Y. Oreg, *Physical Review B* **71**, 075322 (2005).

[182] S. Das, S. Rao, *Physical Review B* **71**, 165333 (2005).

[183] A. Agarwal, D. Sen, *Physical Review B* **76**, 035308 (2007).

[184] J. Splettstoesser, M. Governale, J. König, R. Fazio, *Physical Review Letters* **95**, 246803 (2005).

[185] S. Watson, R. Potok, C. Marcus, V. Umansky, *Physical Review Letters* **91**, 258301 (2003).

[186] P. Leek, et al., *Physical Review Letters* **95**, 256802 (2005).

[187] M. Buitelaar, et al., *Physical Review Letters* **101**, 126803 (2008).

[188] S. P. Giblin, et al., *New Journal of Physics* **12**, 073013 (2010).

[189] M. D. Blumenthal, et al., *Nature Physics* **3**, 343 (2007).

[190] R. Zhu, H. Chen, *Applied Physics Letters* **95**, 122111 (2009).

[191] E. Prada, P. San-Jose, H. Schomerus, *Physical Review B* **80**, 245414 (2009).

[192] J. Wang, Y. Wei, B. Wang, H. Guo, *Applied Physics Letters* **79**, 3977 (2001).

[193] F. Zhou, *Int. J. Mod. Phys.* **B15**, 117 (2001).

[194] M. Blaauboer, *Physical Review B* **65**, 235318 (2002).

[195] M. Governale, F. Taddei, R. Fazio, F. Hekking, *Physical Review Letters* **95**, 256801 (2005).

[196] F. Taddei, M. Governale, R. Fazio, *Physical Review B* **70**, 052510 (2004).

[197] J. Splettstoesser, M. Governale, J. König, F. Taddei, R. Fazio, *Physical Review B* **75**, 235302 (2007).

[198] N. Kopnin, A. Mel'nikov, V. Vinokur, *Physical Review Letters* **96**, 146802 (2006).

[199] B. Wang, J. Wang, *Physical Review B* **66**, 201305 (2002).

[200] J. Wang, B. Wang, *Physical Review B* **65**, 153311 (2002).

[201] S. Russo, J. Tobiska, T. Klapwijk, A. Morpurgo, *Physical Review Letters* **99**, 086601 (2007).

[202] A. Saha, S. Das, *Physical Review B* **78**, 075412 (2008).

[203] M. Alos-Palop, M. Blaauboer, *Physical Review B* **84**, 073402 (2011).

[204] F. Giazotto, et al., *Nature Physics* **7**, 857 (2011).

[205] R. Laughlin, *Physical Review B* **23**, 5632 (1981).